

A New Fault-tolerant Control of Battery Energy Storage Grid-connected System Based on Cascaded H-Bridge

Hu huihui, Liu kaixuan, Wang hanqiang, Zhao rende, Wu mingbo, Donglei

College of New Energy, China University of Petroleum (East China), Qingdao, China

Abstract-- Cascaded H-Bridge (CHB) converter has high output power quality, which can be used in energy storage grid connected systems to control charging and discharging of batteries. But this system contains a large number of switching devices and energy storage batteries, increasing the probability of failure. The traditional fault-tolerant control is not suitable when the state-of-charge (SOC) initial values of the battery modules are not the same. Therefore, a new control strategy is proposed in this paper, which only needs to inject zero-sequence voltage once and makes system control simpler and more efficient. Through MATLAB/Simulink and experiments, it has been proven that the proposed fault-tolerant control can not only maintain normal operation in the event of system failure, but also greatly improve the SOC balance speed.

Index Terms-- Cascaded H-bridge, fault-tolerant control, SOC balancing, zero-sequence voltage injection.

I. INTRODUCTION

In order to improving the conversion efficiency of battery modules and reducing the impact of circulating currents, a kind of topology structure for battery module separate governance strategy(BSGS)is widely adopted, as shown in Fig.1. This structure divides a large battery pack into several small battery modules, and each battery module is connected to an H-bridge unit which can achieve independent charge and discharge control. However, in this case, the probability of battery module or power switch devices failure greatly increases, and it is urgent to study corresponding fault-tolerant control to ensure the reliability and stability of the energy storage grid-connected system.

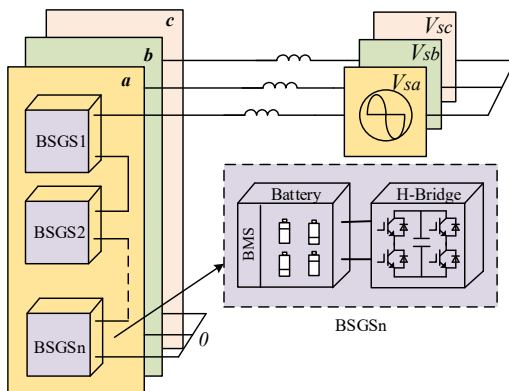


Fig. 1. Topological structure of BSGS.

When a battery module or switch device in the energy storage grid-connected system malfunctions, the faulty unit should be immediately cut off. The output voltage of this unit is 0, which will cause the three-phase voltage output of CHB to be unequal, resulting in an asymmetry in the output current. It will affect the normal operation of the system. In severe cases, it can cause frequency fluctuations in the power grid, which cannot meet the requirements for grid connection. In general, faulty units can only be replaced when the system is allowed to shut down. Therefore, when the system malfunctions, it is very important to take necessary fault-tolerant control, which can timely avoid risks and maintain the normal operation of the energy storage grid-connected system. Fault-tolerance control can be divided into hardware redundancy control and software fault tolerance control. Comparatively speaking, the former is easier to implement, but the system cost will significantly increase. Software fault-tolerant control is technically challenging, but it will not increase additional costs and is more flexible and diverse, which can maximize the energy utilization rate of the remaining healthy modules after a fault [1]-[4].

II. TRADITIONAL FAULT-TOLERANT CONTROL

Due to the star configuration adopted by the cascaded H-bridge converter, the neutral point is in a suspended state. Zero-sequence voltage injection will causes the neutral point potential of the CHB to be different from that of the AC side power supply. This neutral shift can change the output voltage of each phase and making the CHB output a symmetrical three-phase line voltage. Because the actual energy storage grid-connected system is mostly a three wire three-phase system, the zero-sequence component in the output voltage of the cascaded H-bridge converter does not affect the control of grid-connected current. But it can change the output phase voltage. In other words, injecting zero sequence voltage components to generate additional power can adjust the active power of each phase of the cascaded H-bridge converter, without affecting the total power of the system.

In the following, it is assumed that the number of cascaded H-bridge in each phase respectively is N. When the grid-connected system runs normally, the output voltage of each H-bridge is expressed as follows:

$$\begin{cases} u_{an} = mU_{dc} \cos(\omega t) \\ u_{bn} = mU_{dc} \cos(\omega t - \frac{2}{3}\pi) \quad n=1 \dots N \\ u_{cn} = mU_{dc} \cos(\omega t + \frac{2}{3}\pi) \end{cases} \quad (1)$$

where m is the modulation ratio, and U_{dc} is the DC side voltage of each H-bridge.

When a faulty occurs, the faulty unit should be bypassed. Maharan et al. [5] proposes that the modulation ratio of healthy H-bridges in the fault phase can be directly improved to keep the output voltage unchanged. Assuming N_a , N_b and N_c modules are respectively faulty in each phase, the modulation ratio of the remaining healthy modules must be increased to $N/(N-N_a)$, $N/(N-N_b)$ and $N/(N-N_c)$ times to achieve the output of three-phase symmetrical line voltage and maintain the same as before the fault. Due to the different three-phase modulation ratio, the power exchange of the H-bridge unit in normal operation of the three-phase is inevitably different, resulting in the unbalanced SOC of the energy storage battery. SOC is usually defined as the ratio of the remaining battery capacity to the maximum available capacity, used to quantify the current amount of remaining power inside the battery. An important factor affecting the service life of batteries is overcharging and overdischarging caused by the imbalance of SOC between battery modules. Therefore, after bypassing the faulty unit, the fault-tolerant control can maintain the three-phase symmetrical current that meets the grid connection requirements and ensures the SOC balance of the remaining battery modules in CHB to extend the service life of the system. By injecting zero-sequence voltage to achieve neutral shift, the remaining healthy modules are evenly distributed in power, realizing SOC balancing. The essence of this method is to use the principle that zero-sequence voltage can adjust the power between the three phases of CHB. Zero-sequence voltage injection is used to increase the output voltage of the each phase, thereby enabling the cascaded H-bridge converter to output three-phase symmetrical current. In addition, this method can adjust the modulation ratio of the healthy H-bridge unit in the faulty phase to avoid over modulation.

The zero-sequence voltage injection u_{0f} is given by:

$$u_{0f} = U_{0f} \cos(\omega t + \theta_f) \quad (2)$$

In order to maintain the SOC balance of the energy storage battery in the remaining healthy H-bridge unit, the power of each H-bridge unit should be consistent, and the amplitude and phase of the zero-sequence voltage injection can be calculated as follows,

$$U_{0f} = \frac{\sqrt{2[(N_a - N_b)^2 + (N_b - N_c)^2 + (N_c - N_a)^2]}}{3N - N_a - N_b - N_c} \quad (3)$$

$$\theta_f = \begin{cases} \arctan \frac{\sqrt{3}(N_c - N_b)}{N_b + N_c - 2N_a} & N_b + N_c - 2N_a \neq 0 \\ \frac{\pi}{2} & N_b + N_c - 2N_a = 0 \quad N_c - N_b > 0 \\ -\frac{\pi}{2} & N_b + N_c - 2N_a = 0 \quad N_c - N_b < 0 \end{cases} \quad (4)$$

III. NEW FAULT-TOLERANT CONTROL

When the SOC of all energy storage modules is balanced before the fault occurs, traditional fault-tolerant control can be used. However, the SOC of the energy storage battery cannot be guaranteed to be exactly the same in fact. The literatures [6]–[7] propose injecting another zero-sequence voltage to solve this problem and using the unbalance degree of three-phase SOC to calculate it. But this calculation is relatively complex and it will result in the superposition of two zero sequence voltages, which may cause over modulation in the system. From the above analysis, it can be seen that the traditional fault-tolerant control improves the modulation ratio of the faulty phase after removing the faulty unit, causing the SOC imbalance of the energy storage module too. Therefore, the essence of fault-tolerant control is also to achieve SOC balance control. In the literature [8], a fast SOC balancing control is proposed that injecting zero sequence voltage can limit the amplitude of the modulation wave corresponding to the maximum amplitude in the three-phase modulation wave to 1. This enables fast SOC balancing while achieving grid-connected control. On this basis, considering the unequal initial values of SOC, this paper applies fast SOC balancing control to achieve both fault-tolerant control and SOC balancing control simultaneously.

Zero-sequence voltage injection u_0 using fast balancing control is as follows,

$$u_0 = U_0 \cos(\omega t + \theta_0) \quad (5)$$

Assuming the amplitude of phase a is maximum after injecting zero-sequence voltage, the amplitude of the zero-sequence voltage is calculated by (6),

$$\begin{cases} U_0 = \frac{-B + \sqrt{B^2 - 4AC}}{2A} \\ A = 1, B = -2U_{an} \cos \theta_0, \quad C = U_{an}^2 - \frac{1}{(\frac{N}{N - N_a})^2} \end{cases} \quad (6)$$

The phase difference of three-phase modulation waves is $2\pi/3$. The calculation results of phase b and phase c are similar to that of phase a , except for B and C corresponding adjustments required. The specific calculation formula is shown in the appendix.

It is assumed that ΔSOC is unbalance degree, and the calculation results for each phase are as follows,

$$\begin{cases} \Delta SOC_a = SOC_a - SOC \\ \Delta SOC_b = SOC_b - SOC \\ \Delta SOC_c = SOC_c - SOC \end{cases} \quad (7)$$

where $SOC = 1/3(SOC_a + SOC_b + SOC_c)$.

Through PARK transformation, unbalance degree between phases ΔSOC_m and phase angle θ can be obtained by (8) and (9),

$$\Delta SOC_m = \sqrt{\Delta SOC_\alpha^2 + \Delta SOC_\beta^2} \quad (8)$$

$$\theta_0 = \arctan(\Delta SOC_\alpha / \Delta SOC_\beta) \quad (9)$$

This new fault-tolerant control flowchart is shown in Fig. 2.

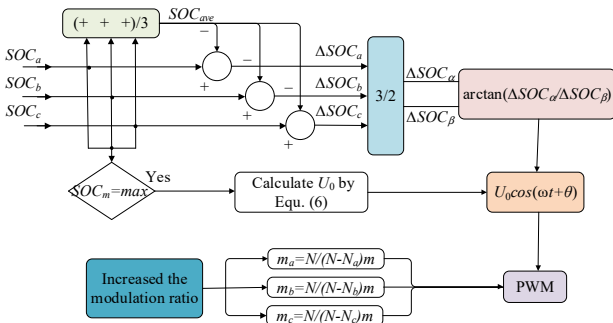


Fig.2. New fault-tolerant control flowchart.

IV. SIMULATION RESULTS AND ANALYSIS

In Simulink, the model of energy storage grid-connected system is built. The rated power of the system is 5,6000W, with 5 H-bridge units cascaded for each phase. The simulation parameters are set as follows: DC bus capacitance $C_1=C_2=470\mu F$, switching frequency is 10 kHz, output voltage frequency of CHB is 50Hz, and filter inductance $L=10mH$. It is assumed that the initial values of three-phase SOC are respectively, 39.4% (phase a), 39.6% (phase b) and 40% (phase c). Assuming that the fifth module of phase a is faulty, the fault unit is removed and the new fault-tolerant control strategy is taking effect.

The grid-connected current and voltage waveform of phase a is shown in Fig.3. The current and voltage are in the same phase, and the cascaded H-bridge energy storage system can realize grid-connected and discharge.

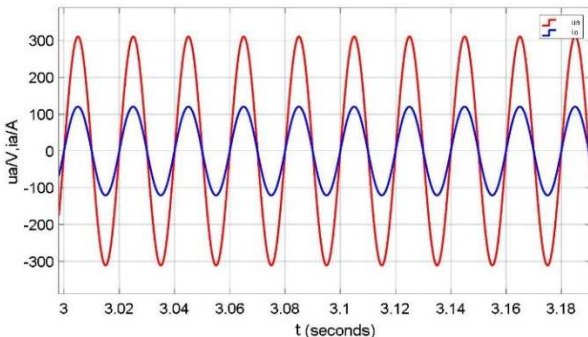


Fig.3. Grid-connected current and voltage waveform of phase a .

The output current waveform of CHB is shown in Fig.4. It can be seen that when the new fault-tolerant control proposed in this paper is adopted, CHB can output three-phase symmetrical current, which also enables the energy storage system to operate stably and meet with grid connection conditions.

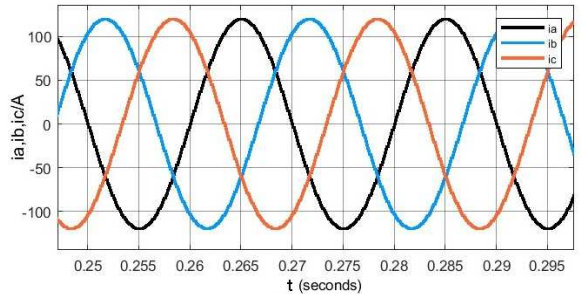


Fig.4. Output current wave of CHB.

The three-phase modulation wave is shown in Fig.5. Because the SOC value of phase c is the largest, to avoid over modulation and maximize utilization, the maximum amplitude of the phase c modulation wave is limited to 1 and maintained until balance between phases is achieved.

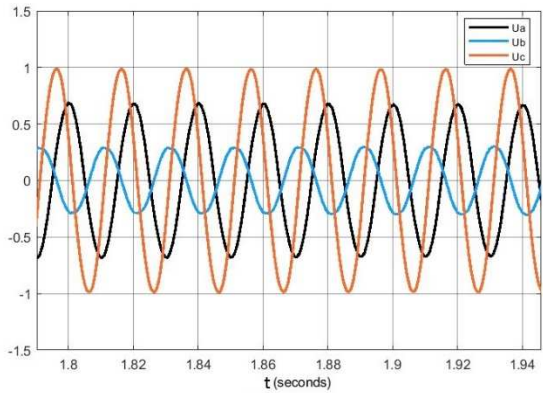


Fig.5. Three-phase modulation wave of CHB.

Fig.6 is output power of CHB. Because the SOC of phase c is the largest, it needs to release the most energy. Under the new fault-tolerant control, P_c is approximated to a constant value for maximum regulation. After a few seconds, the three-phase power is balanced and the system can be transformed into traditional fault-tolerant control. At this time, the remaining 14 modules work properly. In order to maintain the SOC balance, each module has an output power of 4,000W.

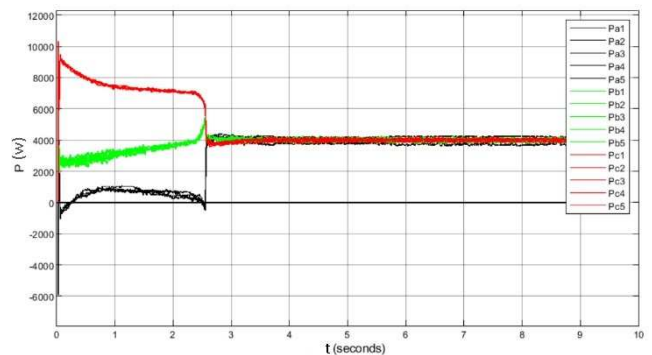


Fig.6. Three-phase output power of CHB

The variation trend of ΔSOC_m is shown in Fig.7. When the amplitude of the zero-sequence voltage injection remains unchanged, ΔSOC_m linearly decreases until SOC equalization is achieved. After that, traditional fault-tolerant control continues to maintain SOC equalization.

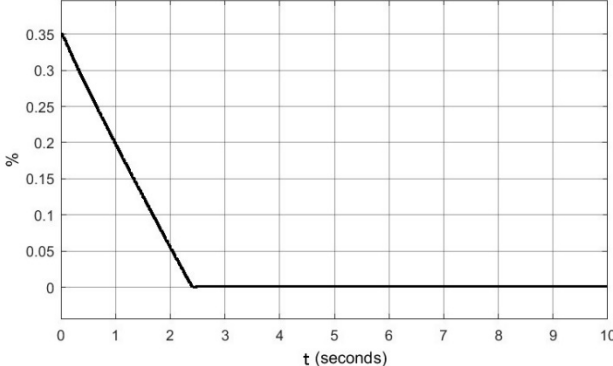


Fig. 7. Unbalance degree between phases (ΔSOC_m)

Fig.8 shows the waveform of three-phase SOC. When the battery discharge, SOC decreases. Because the SOC of phase *c* is the largest, its downward trend is also the most obvious.

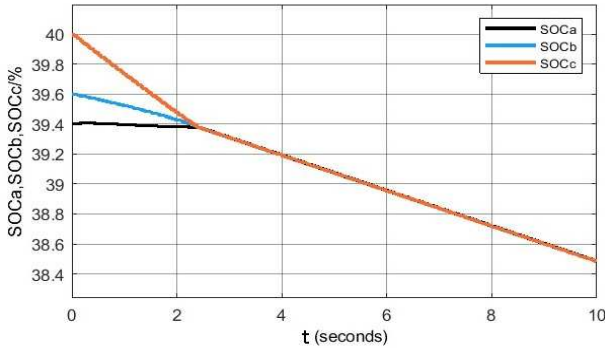


Fig. 7 Waveform of three-phase SOC

V. CONCLUSIONS

The cascaded H-bridge converter has been widely used in energy storage grid connected systems due to its own advantages, but it also makes the system architecture more complex and increases the possibility of faults, requiring corresponding fault-tolerant control to maintain its stable and efficient operation. After cutting off the faulty unit, traditional fault-tolerant control increases the modulation ratio of the remaining healthy units in the faulty phase to output three-phase symmetrical voltage, but it also causes unequal SOC values of battery modules in the energy storage grid connected system, requiring the injection of new zero sequence voltage to maintain balance. When the initial SOC values of the battery modules are not equal, it is necessary to inject another zero sequence voltage for regulation, which not only easily leads to over-modulation but also consumes more time.

This paper proposes a new fault-tolerant control. Even

if the initial SOC values of the battery modules in the energy storage grid connected system are not equal, zero-sequence voltage only needs to be injected once to maintain the maximum amplitude of the three-phase modulation wave at 1. It can ensure system normal operation and achieve SOC balance faster. A calculation formula for new zero-sequence voltage injection has been provided in this paper. Through simulation experiments, it has been verified that the new fault-tolerant control has a significant effect, which can ensure the safe and stable operation of the system even after a fault occurs. It greatly improves the speed of SOC balancing and extends the service life of the energy storage grid connected system.

APPENDIX

Assuming the amplitude of phase b is maximum after injecting zero-sequence voltage. The expression for B and C is given by (10),

$$B = U_{bn} \cos \theta_0 + 1.732 U_{bn} \sin \theta_0, C = U_{bn}^2 - \frac{1}{\frac{N}{N-N_b}} \quad (10)$$

Assuming the amplitude of phase c is maximum after injecting zero-sequence voltage. The expression for B and C is given by (11),

$$B = U_{cn} \cos \theta_0 - 1.732 U_{cn} \sin \theta_0, C = U_{cn}^2 - \frac{1}{\frac{N}{N-N_c}} \quad (11)$$

ACKNOWLEDGMENT

This research was funded by innovation fund project for National Natural Science Foundation of China (Grant Number. 52177203).

REFERENCES

- [1] Xiao Q, Chen L, Jin Y, et al, "An improved fault-tolerant control scheme for cascaded H-bridge STATCOM with higher attainable balanced line-to-line voltages," *IEEE Transactions on Industrial Electronics*, vol. 68, no. 4, pp. 2784-2797, March. 2021.
- [2] Hao Xue, Jinwei He, Yongfeng Ren, "Seamless Fault-Tolerant Control for Cascaded H-bridge Converters Based Battery Energy Storage System," *IEEE Transactions on Industrial Electronics*, vol. 70, no. 4, pp. 3803-3813, June. 2023.
- [3] Paul Gistain Ipoum-Ngome, Rodolfo César Costa Flesch, "Fault-Tolerant Model-Free Predictive Controller for Multilevel Cascaded H-bridge converters With Faulty Cells," *IEEE Transactions on Industrial Electronics*, vol. 69, no. 12, pp. 12225-12236, Nov. 2022.
- [4] Yousef Neyshabouri, Kourosh K. Monfared, "Symmetric Cascaded H-Bridge Multilevel Inverter With Enhanced Multi-Phase Fault Tolerant Capability," *IEEE Transactions on Industrial Electronics*, vol. 69, no.6, pp. 8739-8750, Sep. 2022.
- [5] Maharjan, L, T Yamagishi, "Fault-Tolerant Operation of a Battery-Energy-Storage System Based on a Multilevel Cascade PWM Converter With Star Configuration" *IEEE Transactions on Power Electronics*, vol. 25, no.9, pp. 2386 -2396, Sep. 2010.
- [6] Herzog M, Ebentheuer A W, "State Of Charge Balancing during Fault Tolerant Operation of Battery Storage Systems Based on Cascaded H-Bridge Multilevel Inverter" The 2019 14th International Conference on Ecological Vehicles and Renewable Energies (EVER-Monaco 2019), Monaco, May 2019.
- [7] Xing L, Rui L, "Control of a Battery-Energy-Storage System Based on a Cascaded H-Bridge Converter under Fault Condition" The 2012 7th International Power Electronics and Motion Control Conference (IPEMC-Harbin), Harbin(China),June 2012.
- [8] Hu Huihui;Liu Kaixuan;Wu Mingbo, "Research on SOC Equalization Control Strategy of Cascaded Inverter for Grid-connected Energy Storage System, "The 2022 5th

Characterisation of Grid Short-Circuit Faults with Energy Storage Plant

Chengdong Jiang
*School of Electrical and Electronic Engineering
 North China Electric Power University
 Beijing, China
 1227905031@qq.com*

Wei Dai
*School of Electrical and Electronic Engineering
 North China Electric Power University
 Beijing, China
 2545482372@qq.com*

Chuce Guo
*School of Electrical and Electronic Engineering
 North China Electric Power University
 Beijing, China
 guochuce@163.com*

Pengbo Han
*School of Electrical and Electronic Engineering
 North China Electric Power University
 Beijing, China
 120232201097@ncepu.edu.cn*

Jin Liu
*School of Electrical and Electronic Engineering
 North China Electric Power University
 Beijing, China
 liujin@ncepu.edu.cn*

Abstract—With a large number of new energy power stations connected to the grid, the power quality of the grid will be affected, in this regard, through the grid-connected energy storage power station to suppress the intermittent new energy generation characteristics such as wind power, and large-scale energy storage power station access to the grid will also have an impact on the grid short-circuit current, this paper through the study of different ways of grid-connected storage power station to obtain the short-circuit current of the output of the storage station in different ways to get with the grid type and structural grid type short-circuit current differences in the output of the storage power station. This paper investigates the different ways of grid-connected energy storage plants, obtains the output short-circuit current of energy storage plants under different control methods, gets the difference between the output short-circuit current of grid-following-type and grid-forming-type energy storage plants, and then obtains the short-circuit fault characteristics of the grid containing energy storage plants, and builds a simulation model and a short-circuit current calculation program under MATLAB/Simulink with a certain localized power grid of Shanxi Province, to verify the theoretical accuracy.

Keywords—Energy storage plant, grid-following type, grid-configuration type, short-circuit current

I. INTRODUCTION

China has clearly proposed to reach carbon peak by 2030 and strive for carbon neutrality by 2060, putting forward clear requirements for the development of renewable energy, while the ‘Fourteenth Five-Year Plan’ and the Outline of the Vision for 2035 have also put forward clear tasks for the development of renewable energy, with the aim of constructing a clean, low-carbon, safe and efficient energy system, controlling the total amount of fossil energy and focusing on improving the efficiency of its use, and implementing actions to replace renewable energy. The aim is to build a clean, low-carbon, safe and efficient energy system, control the total amount of fossil energy, focus on improving the efficiency of

the use of renewable energy substitution, deepen the reform of the electric power system, and build a new type of power system with new energy as the main body. Energy storage power station has two functions of storing and releasing electric energy, which means that the energy storage power station can be used as both power supply and load power. The access of large-scale energy storage power station, on the one hand, makes the power grid from the original simple single-side power supply network into a complex dual power supply or even multiple power supply network, the size of the short-circuit current has become complex to judge, on the other hand, due to the introduction of the energy storage converter, making the transient characteristics of the system short-circuit current changes, the traditional short-circuit current discrimination is no longer applicable to the new power system.

Literature [1] analyzed the fault characteristics of IIDGs in microgrids, but the analysis results are not applicable to IIDGs directly connected to the grid. Literature [2] investigated the fault characteristics of IIDGs with constant power control and constant voltage-frequency control but the theoretical analysis is insufficient. Literature [3] studied the fault current characteristics of IIDGs operating in isolated islands. The control strategy of the grid-connected IIDG is different from that of the islanded IIDG. The control strategy of grid-connected IIDGs is different from that of islanded IIDGs, which leads to a big difference in fault current characteristics; literature [4] studied the fault current characteristics of grid-connected IIDGs, but did not fully consider the reactive power support requirements of IIDGs on the grid during the LVRT process.

In the field of power system relay protection, the measurement of short-circuit current is an important way to judge the occurrence of short-circuit faults in the circuit. Therefore, it is particularly important to reasonably analyse and calculate the impact of energy storage power plants on the system short-circuit current [5].

II. MODELLING METHODS FOR ENERGY STORAGE PLANTS

A typical BESS consists of an energy storage battery, converter, transformer, battery management system and monitoring system. It is shown in Figure 1.

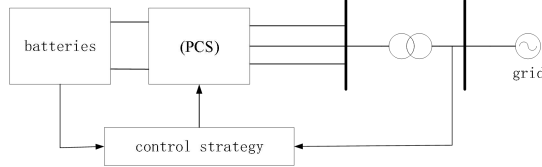


Fig. 1. Structure of grid-connected energy storage

The main components of the energy storage converter are the inverter and the filter, and there are two typical topologies of the energy storage system, the single-stage topology and the two-stage topology, and the two-stage topology is adopted in this paper. The bi-directional AC/DC converter consists of six IGBTs connected in parallel with diodes in a three-phase bridge structure, in which the LC-type filter has gradually replaced the traditional L-type filter in practical applications due to its excellent attenuation effect of high harmonics and its performance advantage at low switching frequency, Fig. 2 shows the two-stage topology of the three-phase grid-connected inverter[6].

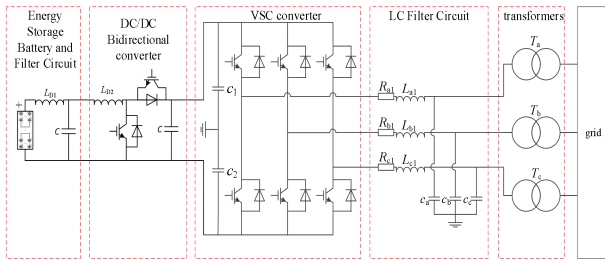


Fig. 2. Three-phase grid-connected inverter two-stage topology diagram

Using a two-stage topology DC side does not require a complex LC filter, small battery measurement ripple, higher control accuracy, and short charging and discharging conversion time. Large-capacity stand-alone design, the DC side can be implemented using multiple DC/DC, each DC/DC unit can be connected to an independent battery pack, without the need for multiple battery packs connected in series and parallel, reducing the difficulty of battery pack configuration; a single group of batteries due to failure replacement, will not degrade the performance indicators of the whole system. AC side or DC side failure, due to the existence of DC/DC circuit link, can effectively protect the battery, to avoid the battery to withstand the impact current, to extend the service life of the battery.

The energy storage system enables a bi-directional flow of energy between the three-phase grid-connected inverter and the grid.

III. GRID-CONNECTED CONTROL STRATEGIES FOR ENERGY STORAGE PLANTS

A. Charge/Discharge Control

The energy storage plant has three operating states, namely, discharge, charge and standby. Batteries are used as energy

storage units, and the DC output during discharge operation is converted to AC by a pulse width modulation (PWM) inverter and connected to the grid. The grid-connected energy storage system adopts different control methods according to different topologies. The single-stage topology converter system consists of a bi-directional converter to realise the active and reactive power control of the system, and a double closed-loop to realise the grid-connected control of the energy storage system, with the inner loop controlling the input and output currents of the storage system, and the outer loop selecting either the constant power (P/Q) control or the constant voltage control according to the control objective. The two-stage topology grid-connected system can have the following two combinations of control modes: one is to take the output power of the AC side as the main control object, to achieve the constant power output of the AC side, the bidirectional converter adopts the P/Q control to control the input and output power of the energy storage system, and the DC/DC converter adopts the constant voltage control to control the DC bus voltage, in order to maintain the stability of the DC bus voltage; the second one is to take the voltage of the DC side as the main control object To achieve the stability of the DC side voltage, the bidirectional converter adopts constant voltage control to maintain the DC bus voltage constant, and the DC/DC converter adopts constant current control to control the charging and discharging power of the energy storage device on the DC side, so as to realise constant current charging and discharging. The charge/discharge control strategy is shown in Fig. 3.

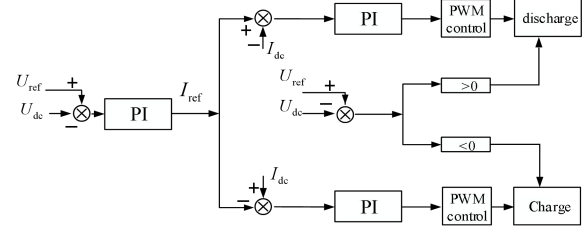


Fig. 3. Charge/discharge control block diagram

The DC/DC converter adopts constant voltage control, as shown in Fig. 3, and the difference between the DC bus reference value U_{ref} and the actual value U_{dc} is used by the PI regulator to provide the energy storage side with the current reference value I_{ref} . The energy storage system is discharged when $U_{\text{ref}} > U_{\text{dc}}$, and charged when $U_{\text{ref}} < U_{\text{dc}}$.

B. PQ Control in Concert with Low Voltage Ride-through Control

The P/Q control is based on the active and reactive power of the energy storage system as the reference command. The block diagram of the P/Q control is shown in Fig. 4. P_{ref} and Q_{ref} are the reference values of the given power, and P and Q are the measured and calculated values, respectively; i_{dref} and i_{qref} are the reference values of the dq-axis components on the AC side, respectively; i_d and i_q are the measured and calculated values of the dq-axis components on the AC side,

respectively; u_d and u_q are the measured and calculated values of the dq-axis components of the inverter output voltage, respectively; u_{dl} and u_{ql} are the reference values of the dq-axis components of the inverter output voltage obtained by decoupling calculation, respectively; L is the inductance of the AC side; and θ is the phase angle of the voltage of the grid-connected system[7].

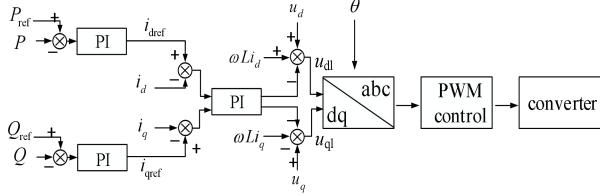
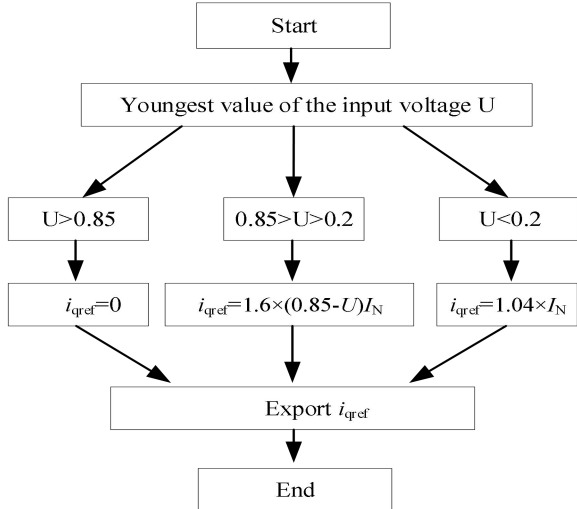


Fig. 4. PQ Control Block Diagram

In the grid-connected operation of the energy storage system, the energy storage converter is required to have a low-voltage ride-through capability, so that the energy storage system can operate continuously without disconnecting from the grid within a certain range of voltage dips and time intervals, and provide a certain amount of reactive power to the grid to support the grid voltage [8].

According to the Technical Specification for Energy Storage Converters for Electrochemical Energy Storage Systems, the dynamic reactive current i_{qref} injected into the grid by the energy storage converter of the electrochemical energy storage system shall meet the following requirements when a voltage dip is caused by a fault in the system:



Where: U for the parallel network point voltage Missing Value, I_N for the rated output current of the energy storage system. The active current reference value i_{dref} of the current

inner loop control takes the smaller value of i_{dref0} and $\sqrt{I_{max}^2 - (i_{qref})^2}$. i_{dref0} is the active current reference value of the energy storage inverter before the failure of the energy storage system. I_{max} is the maximum output current of the energy storage system, I_N is the rated output current of the energy storage system, and the block diagram of the LVRT control strategy is shown in Fig. 5.

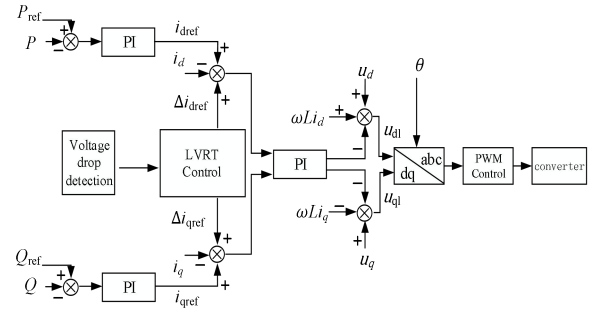


Fig. 5. LVRT control block diagram

C. Droop Control

The studies in this chapter are carried out in the case where the line impedance is inductive, and there exists $X \gg R$, the line resistance R is negligible, i.e., $R=0$. At this point, the difference in the phase angle of the voltages between the AC side of the inverter and the common point is very small, so the approximation has $\sin \varphi \approx \varphi$, $\cos \varphi \approx 1$. Therefore.

$$P_i = \frac{U_{PCC} U_i}{X_i} \varphi_i \quad (1)$$

$$Q_i = \frac{U_{PCC} (U_i - U_{PCC})}{X_i} \quad (2)$$

In general, it is necessary to ensure that the common point voltage U_{PCC} is stable, so its value can be approximated as constant. The size of the active power output from the inverter is mainly related to φ , and the reactive power is related to the voltage magnitude U_i , and the relationship between them is linear. Therefore, by changing the phase angle and amplitude of the inverter output voltage, the active and reactive power can be changed. However, in field operation, the phase angle φ is not easy to measure, and there is an integral relationship $f = d\varphi / (2\pi \cdot dt)$ between f and φ . Therefore, the control of phase angle can be achieved by controlling the frequency [9].

Based on the output characteristics of the inverter the droop characteristic equation can be obtained as

$$\begin{cases} f = f_0 - m(P - P_0) \\ U = U_0 - n(Q - Q_0) \end{cases} \quad (3)$$

Where f and U denote the frequency and amplitude of the output voltage of the inverter; P and Q denote the active and reactive power output from the inverter; f_0 and U_0 denote the reference values of frequency and amplitude; P_0 and Q_0 denote the reference values of active and reactive power; and m and n denote the droop coefficients of the active and reactive power, respectively.

$$\begin{cases} m = \frac{f_0 - f_{\min}}{P_{\max} - P_0} \\ n = \frac{U_0 - U_{\min}}{Q_{\max} - Q_0} \end{cases} \quad (4)$$

The droop control module firstly calculates P and Q according to the power measurement part, and then generates the voltage frequency ω and amplitude U with the help of the droop characteristic curve, and then according to the relationship between the frequency and the phase angle, it can get the input reference voltage of the voltage-current double closed-loop control module. The schematic diagram of the droop control module is shown in Fig. 6.

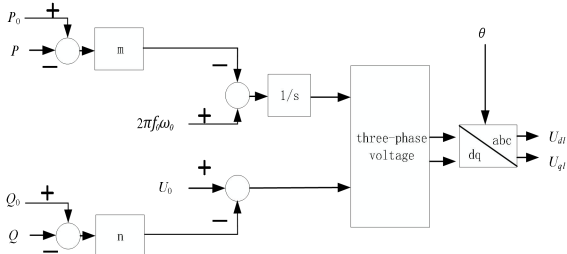


Fig. 6. Droop control block diagram

D. VF Control

The voltage-current double closed-loop control takes the output voltage as the outer-loop control and the filter inductor current as the inner-loop control, as shown in Fig. 7. In the figure, u_{ref} is the reference value of the given voltage; u_{dref} and u_{qref} are the dq component of the voltage reference value; i_{dref} and i_{qref} are the reference value of the dq axis component of the AC side current; i_d and i_q are the actual value of the dq axis current of the AC side current; v_d and v_q are the actual value of the dq axis component of the output voltage of the inverter; v_{sd} and v_{sq} are the reference value of L_s is the coupled inductance of the AC side; f is the the given frequency command; ω is the initial electrical angle of the voltage; θ is the phase angle of the voltage [10].

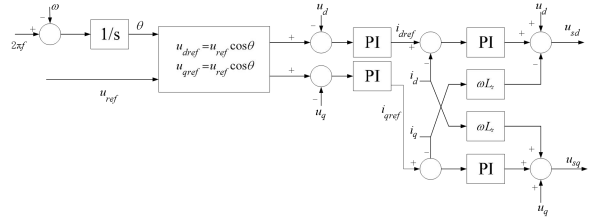


Fig. 7. VF control block diagram

This control strategy, on the basis of the voltage closed-loop, adds the current inner-loop, which realises the control of both the output voltage RMS and the waveform of the output current. The voltage outer-loop control provides voltage support for the AC side, and the inductor current inner-loop control can quickly track load changes and improve dynamic response speed. The simulation analysis of V/f control characteristics is shown in Fig. Under off-grid condition, the voltage and frequency of the parallel network point under V/f control, etc. When the load input changes, the voltage remains unchanged, and the current changes with the change of load power, the main role of V/f control is to keep the voltage and frequency of the parallel network point unchanged [11].

IV. SHORT-CIRCUIT CURRENT CHARACTERISTICS OF ENERGY STORAGE PLANT

When the energy storage power station is connected to the grid, when a three-phase short-circuit occurs at a certain point in the grid, the voltage at the point of the grid drops by 50%, switching between different control modes, the short-circuit current output from the energy storage power station is as follows

A. PQ Control in Concert with Low Voltage Ride-through Control

The figure 8,9 and 10 shows the power, voltage and current output of the energy storage plant when a three-phase short-circuit occurs somewhere in the grid under the grid-connected condition of the PQ-controlled energy storage plant.

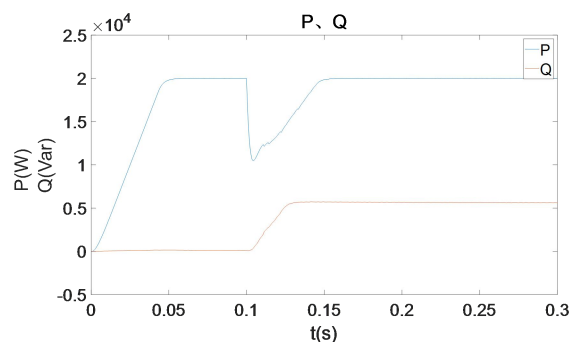


Fig. 8. Active and reactive power under faults

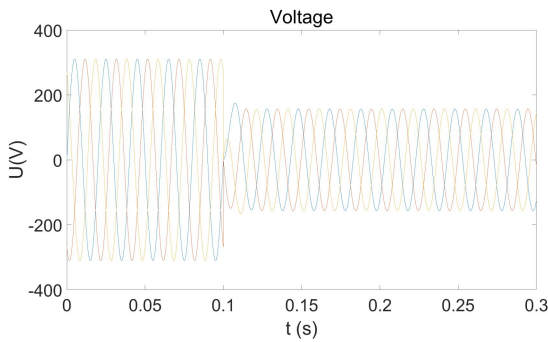


Fig. 9. Short-circuit voltage

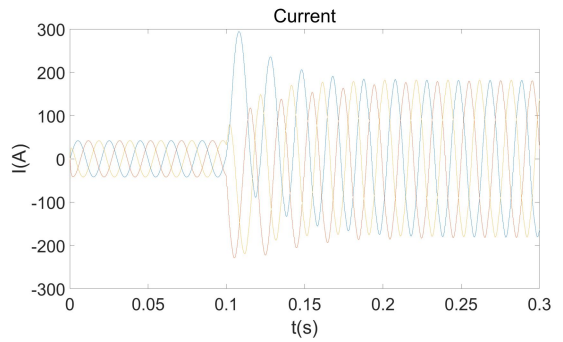


Fig. 13. Short-circuit current

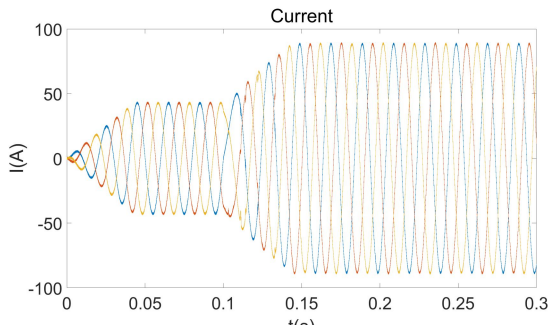


Fig. 10. Short-circuit current

B. Droop Control

The figure 11,12 and 13 shows the power, voltage and current output of the energy storage plant when a three-phase short-circuit occurs somewhere in the grid under the grid-connected condition of the droop control energy storage plant.

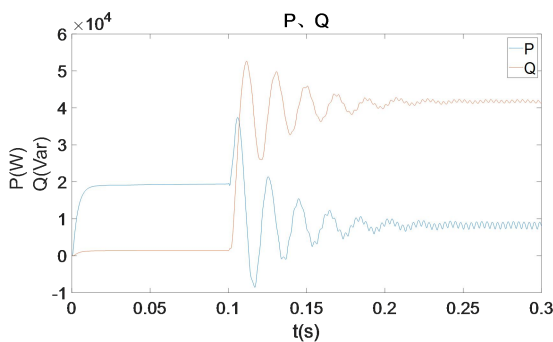


Fig. 11. Active and reactive power under faults

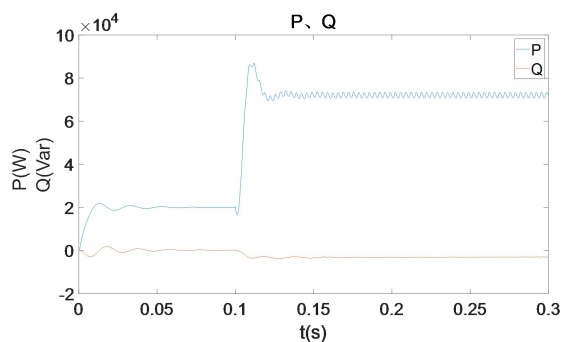


Fig. 14. Active and reactive power under faults

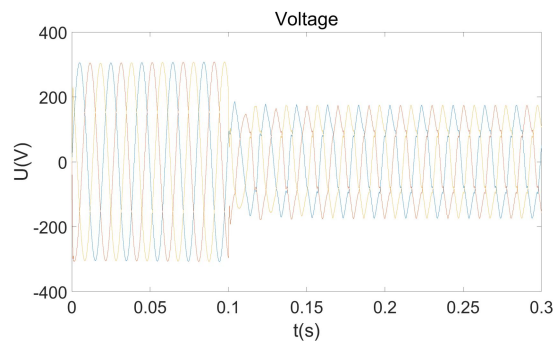


Fig. 12. Short-circuit voltage

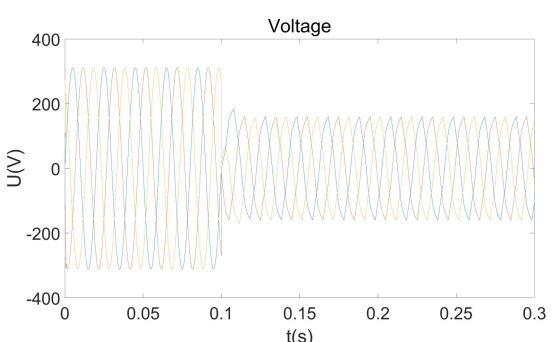


Fig. 15. Short-circuit voltage

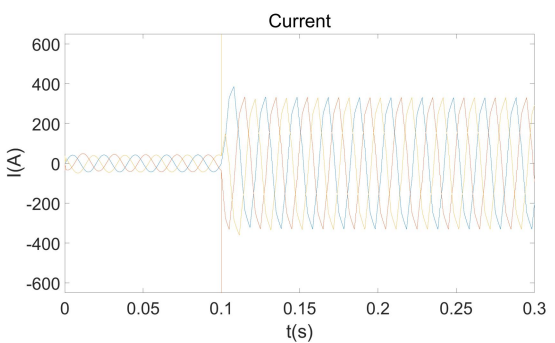


Fig. 16. Short-circuit current

C. VF Control

The figure 14,15 and 16 shows the power, voltage and current output of the energy storage plant when a three-phase short-circuit occurs somewhere in the grid under the grid-connected condition of the VF control energy storage plant.

V. DIFFERENCES BETWEEN GRID-FOLLOWING AND GRID-FORMING CONVERTERS

The output short-circuit current of the energy storage plant varies greatly under the three control modes, in which the PQ control belongs to the grid-following type converter, and the droop control belongs to the grid-conforming type converter, which can be equated to a controlled current source connected in parallel with an impedance, and usually adopts a phase-locked loop to trace the phase angle of the grid to ensure that the converter is synchronised with the grid and the measured phase angle is used as the current control. A grid-type storage converter is equivalent to a controlled voltage source connected in series with an impedance, which is self-synchronised with the grid by the principle of power synchronisation of a conventional generator and does not require a phase-locked loop to measure the grid phase angle. The GFM has a faster power response to improve the frequency stability of the system compared to a conventional generator that improves the grid frequency stability by releasing the kinetic energy stored in the rotating rotor.

1. GFM

The main characteristic of a grid-construction converter is its ability to autonomously form a grid and independently regulate voltage and frequency. Its control strategy is usually similar to that of a synchronous generator, so that it is able to provide higher short-circuit currents in the face of short-circuit faults. The main impacts include: higher short-circuit current contribution: the grid-type converter is able to mimic the behaviour of a synchronous generator by actively regulating the output voltage and current to provide a certain amount of short-circuit current support in the event of a fault. This allows the system to have relatively high current levels during a short-circuit, especially in microgrid or islanding operation scenarios, where the GFM converter can respond to a short-circuit event like a conventional generator. Strong voltage support: Because it can actively regulate the system voltage, it can still support the voltage near the point of fault even during a short-circuit, helping to quickly restore system stability.

2. GFL

A grid-following converter, on the other hand, relies on external grid signals (usually voltage and frequency) to synchronise and adjust its own output. It therefore has a more passive behaviour in the face of short-circuit faults and its contribution to short-circuit current is relatively low. Specific effects include:

Lower short-circuit current contribution: The current output of a grid-following converter is usually limited by its internal control strategy, especially when the voltage of the external grid drops significantly. As a result, the GFL converter's contribution to the short-circuit current in the event of a short-circuit fault is relatively low and will not provide as large a short-circuit current as a synchronous generator.

Dependence on external grid voltage support: The GFL converter relies on the voltage and frequency signals provided by the grid for its operation, and is therefore weakly supported by the voltage during a short circuit. If the grid voltage

collapses, the GFL converter may not be able to provide effective power support.

The GFM converter is able to provide higher short-circuit currents during short-circuits, and has strong support for grid voltage and frequency, which makes it particularly suitable for islanded operation or microgrid scenarios.

The GFL converter has a lower current contribution during short-circuit and relies on grid signals for its operation, and therefore exhibits weaker voltage support during grid faults.

As shown in Fig. 17 is the comparison of RMS values of short-circuit currents under the three control modes. the VF control output short-circuit current is the largest, followed by the droop control, and the PQ control short-circuit current is the smallest.

Since PQ control is constant power control, when the grid voltage dips, its output current increases compared to normal, but the power remains constant; with sag control, the converter reactive power command increases due to the voltage drop of 50% at the PCC point, which sends out reactive power to support the voltage, thus increasing its total apparent power, which in turn makes the output current increase more. The grid-type converter mostly uses sag control, and its effect on short-circuit current will be even greater. In some field test conditions, the converter is required to have an overcurrent capacity of 3 times under such conditions, the short-circuit current provided by the converter at this overcurrent multiplier will rise sharply to 1.3-3 times the rated current, and its impact on the grid short-circuit current will be further increased.

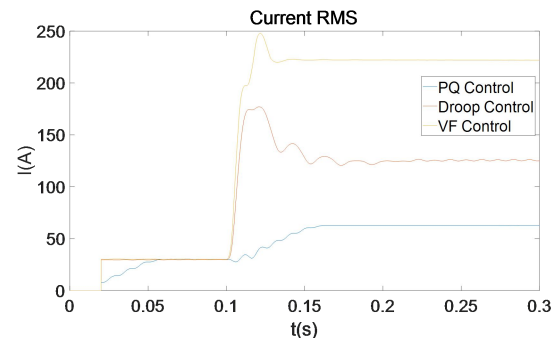


Fig. 17. RMS short-circuit current

Comparison of short-circuit currents at the output of an energy storage plant under three control methods.

TABLE I. SHORT-CIRCUIT CURRENT

Short-circuit current supplied by energy storage plant	
control method	Three-phase short circuit/A
PQ Control	62.6
Droop Control	125.1
VF Control	221.2

VI. CALCULUS ANALYSIS

Selecting a local power grid in Shanxi Province and building a simulation model in MATLAB/Simulink

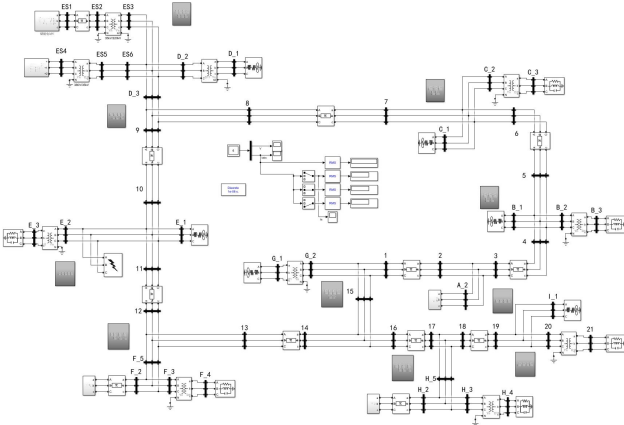


Fig. 18. Grid Simulation Models

In the event of a three-phase short-circuit fault at different locations on the grid, the circuit currents output from the energy storage plant are shown in Table 2

TABLE II. SHORT-CIRCUIT CURRENT

Short-circuit current supplied by energy storage plant (220kV side)	
Parallel Point Voltage	Three-phase short circuit/kA
0.7U _N	0.351
0.5U _N	0.513
0.3U _N	0.826

VII. CONCLUSION

When a short-circuit occurs in the grid containing an energy storage plant, its short-circuit current characteristics mainly depend on its converter control method, when PQ control is used, its short-circuit current is limited to the

maximum output power, so the output current is smaller, when droop control is used, it mimics the behaviour of synchronous machines, with strong voltage support capability, more output power and greater output short-circuit current.

REFERENCES

- [1] Han Yi,Zhang Dongxia.Fault analysis of microgrid composed by inverter-based distributed generations[J].Power System Technology,2011,35(10):147-152.
- [2] Baran M E,El-Markaby I.Fault analysis on distribution feeders with distributed generators[J].IEEE Transactions on Power Systems,2005,20(4):1757-1764.
- [3] Plet C A,Brucoli M,McDonald J D F,et al.Fault models of inverter-interfaced distributed generators:experimental verification and application to fault analysis[C]//2011 IEEE Power and Energy Society General Meeting.San Diego:IEEE,2011:1-8.
- [4] Plet C A,Graovac M,Green T C,et al.Fault response of grid-connected inverter dominated networks[C]//2010 Power and Energy Society General Meeting.Minneapolis:IEEE,2010:1-8
- [5] Li Hui, Liu Dong, Yao Danyang. Analysis and Reflection on the Development of Power System Towards the Goal of Carbon Emission Peak and Carbon Neutrality [J]. Proceedings of the CSEE, 2021, 41 (18) : 6245-6259.
- [6] Baran M E, El-Markaby I. Fault analysis on distribution feeders with distributed generators[J]. IEEE Transactions on Power Systems , 2005, 20 (4) : 1757-1764.
- [7] Plet C A, Brucoli M, McDonald J D F, et al. Fault models of inverter-interfaced distributed generators : experimental verification and application to fault analysis[C]//2011 IEEE Power and Energy Society General Meeting. San Diego : IEEE, 2011 : 1-8.
- [8] Boutsika T N, Papathanassiou S A, Short-circuit calculations in networks with distributed generation[J]. Electric Power Systems Research, 2008, 78 (7) : 1181-1191.
- [9] Jiang Xingyue. Integrating Load Flow and Short-Circuit Current Calculation for Distribution Systems Containing Distributed Generations[D]. Tianjin University, 2007
- [10] Plet A C, Green C T. Fault response of inverter interfaced distributed generators in grid-connected applications[J]. Electric Power Systems Research, 2014, 106.
- [11] Zhang Die, Yuan Xufeng, Zhang Lahua et al. Research on Low Voltage Ride-through Control Strategy of Soft Open Point[J]. Electric Power Science and Engineering, 2021, 37 (09) : 1-9.

Characterization of Short-circuit Faults Within Battery Modules for Energy Storage Systems

Zhicheng Li

State Grid Fujian Electric Power Co.,
Ltd.
Electric Power Science Research
Institute
Fuzhou, China
565339368@qq.com

Shuling Zhang

State Grid Fujian Electric Power Co.,
Ltd.
Electric Power Science Research
Institute
Fuzhou, China

Yeqiang Deng

Wuhan University
School of Electrical Engineering and
Automation
Wuhan, China

Weijun Zhang*

State Grid Fujian Electric Power Co.,
Ltd.
Electric Power Science Research
Institute
Fuzhou, China
14158755@qq.com

Yuge Chen

State Grid Fujian Electric Power Co.,
Ltd.
Electric Power Science Research
Institute
Fuzhou, China

Xiaolong Gu

Wuhan University
School of Electrical Engineering and
Automation
Wuhan, China

Biao Li

State Grid Fujian Electric Power Co.,
Ltd.
Electric Power Science Research
Institute
Fuzhou, China

Chaoping Deng

State Grid Fujian Electric Power Co.,
Ltd.
Electric Power Science Research
Institute
Fuzhou, China

Yu Wang

Wuhan University
School of Electrical Engineering and
Automation
Wuhan, China

Abstract—With the rapid increase in the proportion of new energy installed capacity, in order to solve the problem of new energy output volatility, battery energy storage by virtue of its electrical characteristics and economic advantages of the rapid development, and gradually tend to modularization and large capacity, but also accompanied by battery short circuit, thermal runaway and other safety issues. This paper takes a domestic battery energy storage station as a reference, combines the current decoupling control, builds a complete cascade H-bridge battery energy storage system simulation model, calculates the electrical parameter change rule when short-circuit fault occurs inside the battery module under different operating power, and summarizes the fault characteristics under different fault conditions. The study shows that the battery terminal voltage will fall to different degrees, and under the control of the power module, the system operating power will recover after a short fluctuation. A large short-circuit current will be generated internally, but the short-circuit current remains unchanged with the change of operating power. The battery cluster current has exceeded the maximum allowable current, and failure to remove the fault in time can seriously damage the battery.

Keywords—Cascade type; Battery storage; Internal short circuit; Fault characterization

I. INTRODUCTION

With¹ the rapid development of wind and renewable energy, the demand for energy storage gradually tends to scale and large capacity, gigawatt-hour battery energy storage power plant has become a national strategic development of emerging industries^[1-3]. For the high-voltage

battery integrated system, the number of batteries is large, the integrated structure is complex, the probability of short-circuit accidents is higher, and the failure triggered accidents is more serious. The current lithium battery energy storage system can not fully realize the early warning function, only when the failure occurs through the smoke, temperature and other information for fault alarm, lack of effectiveness, is still unavoidable to cause economic losses^[4-6].

Literature^[7] constructs an active safety system for energy storage power stations is constructed, which establishes the safety defense of the energy storage system from the three perspectives of risk source identification, fault identification and accident identification. Among them, the active risk source identification mainly relies on the battery management system to evaluate the battery state, and the accuracy of the evaluation depends on the mastery of the fault characteristics of the battery pack. In this regard, the literature^[8-9] quantitative analysis of battery pack short circuit fault current change law, but it only considered the battery pack static working condition short circuit characteristics, did not consider the energy exchange with the PCS and AC system. However, the research object is the traditional non-cascaded energy storage power station, and it is not necessarily applicable to the research of large-scale energy storage fault characteristics at the GWh level^[10-11].

In the aforementioned research status quo, this paper builds a simulation model of gigawatt-hour cascade H-bridge battery energy storage system, conducts a systematic research on the operating characteristics of battery system under different short-circuit fault types and different operating conditions, and analyzes the

¹ This paper is supported by the science and technology project of State Grid Fujian Electric Power Co., Ltd., the project name is "gigawatt time-class lithium-ion battery energy storage system technology (battery system high voltage integration and fault protection)", and the project code is (52130423000H).

safety risk of energy storage system under typical faults, so as to provide reference for the safety protection of battery energy storage system..

II. SIMULATION MODELING OF CASCADED H-BRIDGE BATTERY ENERGY STORAGE SYSTEM

A. Structural parameters of cascaded H-bridge battery storage system

The cascaded H-bridge based battery energy storage system (CHB-BESS) connects the battery cells into clusters in series and then connects them to the DC side of the H-bridge power electronic modules, and the series connection of the H-bridge power modules replaces the series connection of the battery cells to increase the voltage, which improves the voltage level and capacity of the storage system and ensures that each power module has a reasonable voltage withstand range. [12-13].

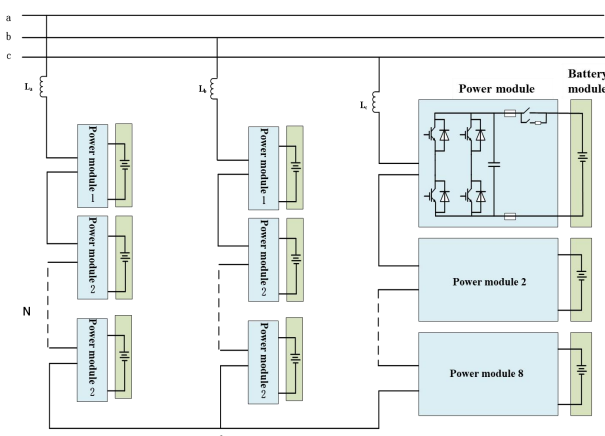


Fig. 1. Structure of cascade H-type energy storage system

The structure and parameters of the large-capacity high-voltage battery energy storage system studied in this paper are based on a pilot demonstration project of a large-scale domestic energy storage power station as a reference. When designing a cascaded battery energy storage system, the number of cascades of each phase power module needs to meet the requirements of grid-connected voltage, system redundancy and equalization function^[14]. In this paper, the number of power modules in each phase needs to meet the requirements of grid voltage, system redundancy and equalization. In this paper, we mainly consider from the perspective of grid-connected voltage, to ensure that the battery module voltage can meet the impact of grid voltage fluctuation and voltage unbalance on grid-connected while uninterrupted charging and discharging changes. From this, equation (2.1) can be used to calculate the number of links N for each item.

$$\frac{N \times U_{dcmin}}{\sqrt{2}} \geq \frac{U_s}{\sqrt{3}} \times K_v \times K_b \times K_L \quad (1)$$

Where U_{dcmin} is the minimum working voltage of the battery module, U_s is the rated voltage of the grid, K_v is the correction factor for the maximum fluctuation of the grid voltage, K_b is the correction factor for the most serious imbalance of the grid voltage, and K_L is the correction factor for the maximum voltage drop of grid-connected reactor. K_v is taken as 1.07, which is mainly referenced to the "Permissible Deviation of Power Supply Voltage for Electricity Quality", which points out

that voltage deviation of the power grid of 20kV and below is controlled within 7%. It is stated that the voltage deviation of the grid with 20kV and below is controlled within 7%, so the correction factor of grid voltage in extreme condition is taken to be 1.07. K_b is taken to be 1.02, which can be referred to the requirement of "Allowable imbalance degree of three-phase voltage of power quality", and the imbalance degree of the grid-connected voltage should not be more than 2% under the extreme condition. The battery side voltage of the energy storage station referred to in this paper is 728 to 936 V, so U_{dcmin} is 728 V. The rated voltage of the energy storage system connected to the grid in this project is 10 kV, i.e., U_s is 10,000 V. The voltage drop of the resistor is generally not large, so K_L is 1.1, and then the number of links N needs to satisfy equation (2.2).

$$N \geq \frac{\sqrt{2} \times 10 \times 10^3 \times 1.07 \times 1.02 \times 1.15}{\sqrt{3} \times 728} = 13.46 \quad (2)$$

N needs to be rounded upwards, so in this paper $N = 14$, i.e., the number of links per phase of the cascade-type battery energy storage system is 14, and the number of battery modules of the whole energy storage system is 42.

The energy storage system consists of 42 subsystems (battery modules), each of which consists of 1 control cabinet and 25 electrical cabinets. A single battery cabinet consists of 5 battery boxes connected in series, and each battery box consists of 52 lithium iron phosphate batteries in series, with a battery monitoring unit inside the battery box. Considering the topology alone, each battery cabinet can be made up of 5 battery boxes connected in series to form a battery cluster, so the internal topology of a single battery module can be used as shown in Figure 2.3. N needs to be rounded upwards, so in this paper $N = 14$, i.e., the number of links per phase of the cascade-type battery energy storage system is 14.

The energy storage system consists of 42 subsystems (battery modules), each of which consists of 1 control cabinet and 25 electrical cabinets. A single battery cabinet consists of 5 battery boxes connected in series, and each battery box consists of 52 lithium iron phosphate batteries in series, with a battery monitoring unit inside the battery box. Considering the topology alone, each battery cabinet can be made up of 5 battery boxes connected in series to form a battery cluster, so the internal topology of a single battery module can be used as shown in Figure 2.3.

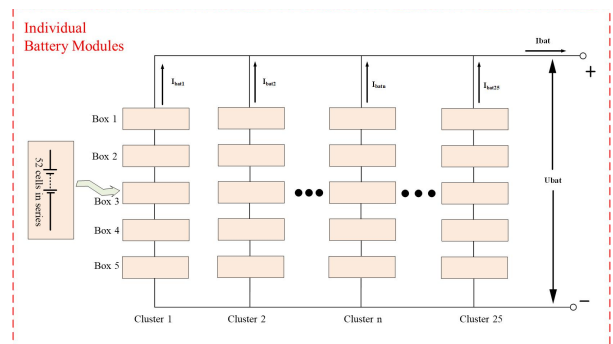


Fig. 2. Internal structure of a single battery module

B. Cascade H-bridge power control

Fig.3 shows the overall flow of grid-connected

power control of cascaded battery storage system. Firstly, the three-phase voltages U_a , U_b , U_c and currents I_a , I_b , I_c of the grid-connected point need to be collected, and the phase of the grid-connected point voltage is obtained through the phase-locked-loop PLL link, and the Pike transform is applied to it, so that the three-phase voltages and currents of the grid-connected point are transformed to the dq rotating coordinate system, and the intermediate control quantities U_d , U_q , and I_d , I_q are obtained.

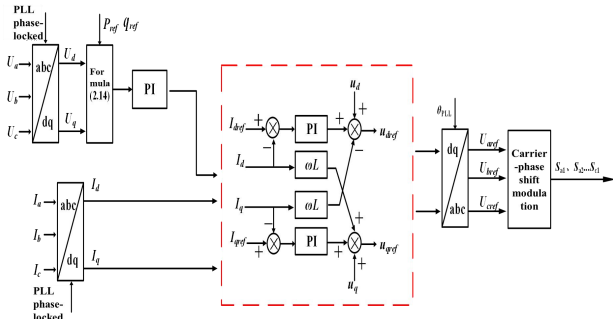


Fig. 3. Power control structure of cascade battery energy storage system

This is followed by the power outer loop control, which calculates the grid-connected current component references I_{dref} and I_{qref} in d-axis and q-axis according to the instantaneous power calculation formula, through the dc voltage and the set reference values of active and reactive power, and then by using the PI control and negative feedback link.

Secondly, the reference component of the current is introduced into the current inner-loop control, which is involved in the calculation of the active current I_d and the reactive current I_q , respectively, to obtain the reference values of the d-axis component and the q-axis component of the voltage at the parallel network point U_{dref} and U_{qref} through the feed-forward decoupling control as described before.

Finally, the Pike inverse transform is performed on the reference value of the grid-connected point voltage to obtain the reference values of the three-phase AC voltage, U_{aref} , U_{bref} , U_{cref} , and the carrier-phase shifting method is used to modulate the reference value of the AC voltage, and the control signals generated from these signals, S_{a1} , S_{a2} ... S_{c1} , are used as the control signals of the cascaded power devices, which ultimately realizes the power control for the grid-connected battery energy storage system. The control signals S , S ... S are used as the control signals of the cascaded power devices to realize the power control of the battery storage system on the grid^[15-16].

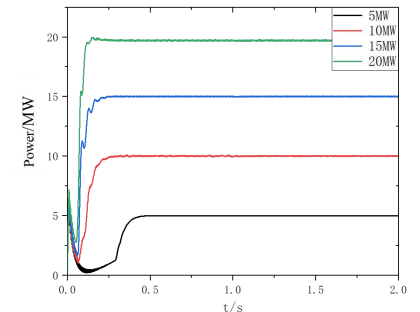
III. SIMULATION STUDY OF FAULT CHARACTERISTICS OF LITHIUM-ION BATTERY PACKS

A. Short-circuit faults within the battery cluster

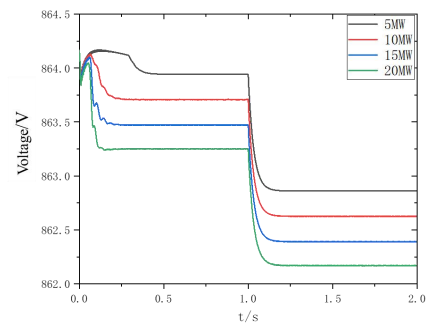
Set the simulation time as 2s and the fault moment as 1s, i.e., the battery system operates normally during 0~1s, and the battery is in the short-circuit fault state during 1~2s. Taking the case of SOC=60% as an example, we analyze the discharge multiplier of the battery system in the battery cluster at 0.125C, 0.25C, 0.375C, 0.5C, i.e., the operating power of 5MW, 10MW, 15MW, and 20MW. No. 1 monomer and No. 16 monomer short-circuit failure

occurs.

From Fig. 4, it can be seen that the transition time from startup to stabilization of the system becomes shorter while the battery discharge power increases. From Fig. (a), it can be seen that the system tends to stabilize from startup to the time when the power reaches the reference power during the period from 0 to 1s. The higher the power, the shorter the transition time of startup, but the amplitude of transient fluctuations increases slightly. the failure occurs at the moment of 1s, and the battery operating power hardly fluctuates, which shows that the system can be stabilized under the control of the power module. From Fig. (b), it can be seen that when the fault occurs, the overall terminal voltage of the battery module will fall to different degrees, and the final steady-state value of the voltage will become lower with the increase of the power, and the final steady-state value of the voltage is 862.86V, 862.62V, 862.39V, 862.17V in order under the 5-20MW. from Fig. (c), it can be seen that the short-circuit current at the moment of 0-1s is almost 0, and the short-circuit current is about 18kA when the fault occurs. moment reaches about 18kA, and the steady-state value of the short-circuit current is almost unchanged with the increase of the operating power, which is due to the fact that the operating power does not affect the short-circuit circuit.



(a) Battery module power change



(b) Battery module terminal voltage change

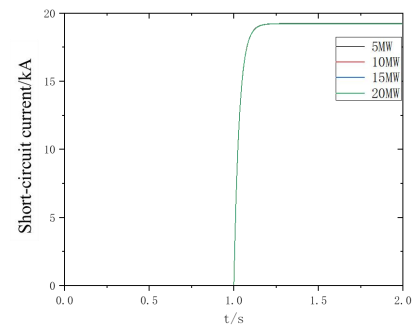


Fig. 4. Variation of the main parameters of the battery module

Figure 5 shows the change rule of each battery cluster current under 20MW. I_{bat1} and I_{batn} indicate the current of faulty battery cluster and normal battery cluster. Before the fault occurs, the current of each battery cluster is in the normal state, about 0.9kA. When the fault occurs, the polarity of the two is reversed, in which I_{bat1} rises rapidly and finally stabilized at about 24kA, much larger than the normal operating conditions, I_{batn} is also a little higher than the normal, stabilized at about 1.7kA, the discharge current is less than 1C, which is still in the safer state.

From the above analysis, it can be seen that when the short-circuit fault occurs inside the battery box, although the battery pack external output power, voltage and current and other parameters do not change significantly, but the short-circuit circuit has generated a very high short-circuit current, generating a large amount of heat, which for a long time will lead to thermal runaway of the battery or even fire and explosion, and the battery clusters will inevitably form a loop current between the battery clusters, and the entire battery pack of batteries are in an abnormal state, and the operation of the system is seriously affected. The operation of the system is seriously affected.

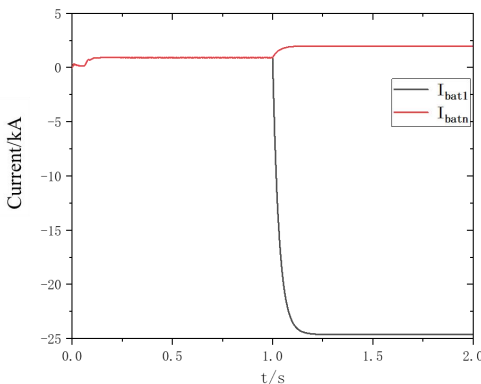


Fig. 5. Current variation of each battery cluster

B. Short-circuit failures between cell clusters

According to Fig. 6, it can be seen that the transition time of the system from startup to stabilization becomes shorter with the increase of battery discharge power. From Fig. (a), it can be seen that the fault occurs at the moment of 1s, and the power curve shows obvious fluctuation, after which it returns to stability, which is different from the short-circuit fault inside the battery box, indicating that the fault between the battery clusters causes larger fluctuations in the system, but the system quickly returns to stability under power control. From Fig. (b), it can be seen that the overall terminal voltage of the voltage module will drop to different degrees when the fault occurs, and the final steady-state value of the voltage will become lower with the increase of the power, and the final steady-state value of the voltage is 848.89 V, 848.66 V, 848.42 V, and 848.19 V in order under 5-20 MW. From Fig. (d), it can be seen that the short-circuit current doesn't change with the change of the operating power, and the At this time, the steady-state value of short-circuit current has reached about 63kA, which seriously affects the safe operation of the battery pack.

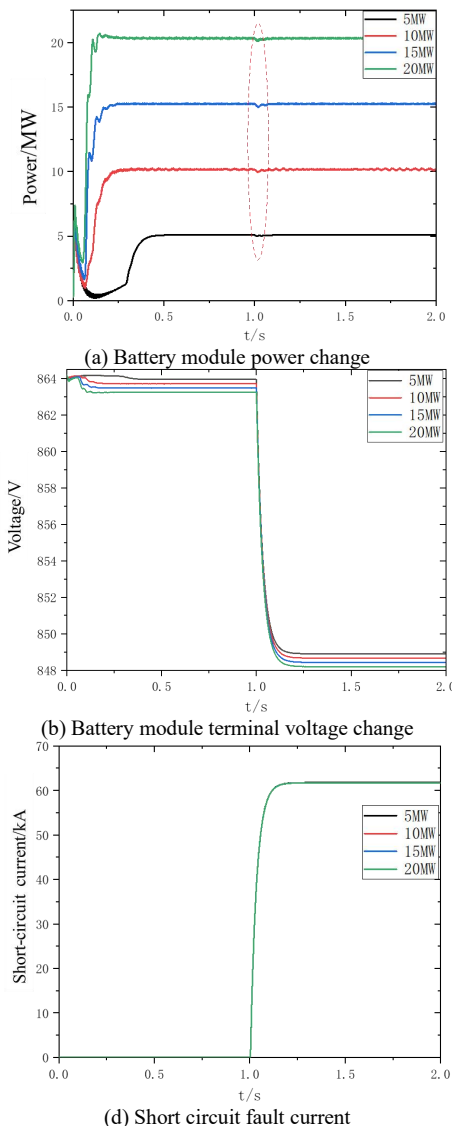


Fig. 6. Changes in the main parameters of the battery module

Inter-cluster short-circuit fault will make two clusters in an abnormal state, at this time the inter-cluster loop current is more serious, so it is necessary to study the characteristics of each cluster current change. Let each battery cluster current be I_{bat1} , I_{bat2} I_{batn} , where I_{batn} denotes the current of the non-faulty battery cluster.

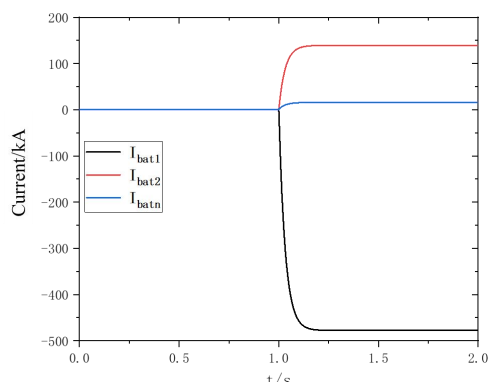


Fig. 7. Current change rule of each cell cluster during inter-cluster failure

As shown in Fig. 7, the current change of each

battery cluster when the output power of the system is the rated discharge multiplier (20 MW), in which due to the short circuit between battery clusters 1 and 2, the currents of the two, I_{bat1} , I_{bat2} , change significantly, with opposite polarity and very large amplitude. Since the batteries of battery cluster 1 at both ends of the short-circuit circuit are at a high potential and the batteries of battery cluster 2 are at a low potential, the current of battery cluster 1 is negative, and the whole is in a clearly discharged state, which supplies power to all the other clusters. Battery cluster 2, on the other hand, is in a charging state, and the cluster current is significantly higher than other normal clusters, indicating that the energy from battery cluster 1 is mainly flowing to battery cluster 2. I_{batn} The current is also positive, with an amplitude of about 16 kA, indicating that the other normal clusters are less affected, but that the current values of the entire battery module have significantly exceeded the normal operating values.

CONCLUSION

In this paper, according to the internal integration structure of the actual battery module, short-circuit faults are categorized into intra-cluster short-circuit and inter-cluster short-circuit faults, and then based on the battery energy storage simulation model constructed in the previous section, the operation characteristics of the system under the two kinds of faults are systematically investigated. The main conclusions are as follows:

(1) Under the control of the power module, the short-circuit fault within the battery cluster does not significantly affect the operating power and steady-state current of the battery module, while the battery terminal voltage drops to different degrees and the internal short-circuit current reaches 18 kA. In the case of a short-circuit fault between the battery clusters, the fault moment will cause a large fluctuation in the power and current, and the power will be restored to the reference power value, and the steady state value of the current at this time will be slightly larger than that during normal operation. during normal operation.

(2) different faults under different rules of change of battery cluster current, non-fault battery cluster current and fault battery cluster current polarity opposite, and the latter far more than the normal operating state, the formation of loop current between the battery cluster. Battery box failure non-fault battery cluster current of 1.7kA, is still in a relatively safe range, between the battery box and the short circuit between the cluster failure, the battery cluster current has exceeded the maximum allowable current, do not timely excise the fault will seriously damage the battery.

ACKNOWLEDGMENT

This paper is supported by the science and technology project of State Grid Fujian Electric Power Co., Ltd., the

project name is " gigawatt time-class lithium-ion battery energy storage system technology (battery system high voltage integration and fault protection)", and the project code is (52130423000H).

REFERENCES

- [1] BAI Jianhua, XIN Songxu, LIU Jun, et al. Study on the development path of realizing high proportion of renewable energy in China[J]. China Journal of Electrical Engineering, 2015,35(14):3699-3705.
- [2] Chu S, Majumdar A. Opportunities and challenges for a sustainable energy future[J]. Nature, 2012, 488(7411): 294-303.
- [3] Xie Xiaorong, Ma Ningjia, Liu Wei et al. Review and outlook of energy storage applications in new power systems[J]. Chinese Journal of Electrical Engineering, 2023, 43(01): 158-169.
- [4] WANG Mingmin, SUN Lei, GUO Pengyu et al. Thermal runaway characteristics of lithium iron phosphate energy storage battery module overcharge based on online gas monitoring[J]. High Voltage Technology, 2021, 47(01): 279-286.
- [5] ZHU Xiaoqing, WANG Zhenpo, WANG Hsin et al. A review on thermal runaway and safety management of lithium-ion power batteries[J]. Journal of Mechanical Engineering, 2020, 56(14): 91-118.
- [6] TANG Wenjie, JIANG Xin, LIU Hao Yan et al. Early warning of lithium-ion battery fire based on gas-liquid fugitive image recognition[J]. High Voltage Technology, 2022, 48(08): 3295-3304.
- [7] Yang Ram, Huang Xiaoqing, Yu Shengqian et al. Research on active safety of electrochemical energy storage power plants[J]. Power Automation Equipment, 2023, 43(08): 78-87.
- [8] XU Guangfu, JIANG Miao, WANG Wanchun et al. Analysis of short-circuit faults and protection strategies for large-scale energy storage batteries[J]. Energy Storage Science and Technology, 2022, 11(07): 2222-2232.
- [9] Wan Jun. Research on protection key technology of large battery energy storage power station [D]. Shanghai Jiao Tong University, 2013.
- [10] LI Jianlin, WU Yiwen, WANG Nan et al. Research review and outlook of gigawatt-scale electrochemical energy storage plants[J]. Power System Automation, 2021, 45(19): 2-14.
- [11] de la Torre S, González-González J M, Aguado J A, et al. Optimal battery sizing considering degradation for renewable energy integration[J]. IET Renewable Power Generation, 2019, 13(4): 572-577.
- [12] LIU Chang, CAI Xu, LI Rui et al. Capacity boundary and optimization design of ultra-large capacity chain battery energy storage system[J]. High Voltage Technology, 2020, 46(06): 2230-2241.
- [13] LIU Chang, WU Xiqi, JIANG Xinyu et al. Battery stack segmentation method for high-voltage direct-mounted large-capacity energy storage systems[J]. Chinese Journal of Electrical Engineering, 2023, 43(19): 7483-7497.
- [14] Cao Yang. Design and realization of 2MW/10kV high-voltage cascade H-bridge battery energy storage system [D]. Shanghai Jiao Tong University, 2015.
- [15] MAO Su-Min, CAI Xu. Control strategy of large-capacity chain battery storage power conditioning system[J]. Grid Technology, 2012, 36(09): 226-231.
- [16] SUN Yichao, ZHAO Jianfeng, JI Zhendong. DC voltage balance and power equalization control strategy for grid-connected cascaded H-bridge converter[J]. Power Automation Equipment, 2014, 34(01): 55-60.

DC Fault Characteristics of Battery Energy Storage System Based on Different Grid-Connected Structures

Qingyao Sun¹, Weijie Wen^{1*}, Huiwen He², Lei Wang², Jiangang Xu³, Yang Xu⁴, Bin Li¹

¹*Key Laboratory of Smart Grid of Ministry of Education, Tianjin University, Tianjin, China.*

²*China Electric Power Research Institute, Wuhan, China*

³*State Grid Jiangsu Electric Power Co., Ltd., Nanjing, China*

⁴*State Grid Jiangsu Electric Power Co., Ltd. Research Institute, Nanjing, China*

*weijie.wen@tju.edu.cn

Keywords: BATTERY ENERGY STORAGE SYSTEM, FAULT ANALYSIS, DC/DC CONVERTERS

Abstract

To optimize the protection scheme of battery energy storage systems (BESSs) in the future, characteristics of DC fault current of BESSs with different grid-connected structures are studied in this paper. During the research, three grid-connected structures for BESS are analyzed, including battery clusters connected directly (structure_1), battery clusters connected through non-isolated DC/DC converter (structure_2), battery clusters connected through isolated DC/DC converter (structure_3). The equivalent circuit and the numerical calculation method of fault current are provided. The theoretical analysis is verified by simulation in PSCAD/EMTDC. The research results proved that the fault current has high peak value and rapid rise speed when non-isolated DC/DC is used, which poses great technical challenges to protective devices, such as fuse and DC breaker. Finally, comparison of three grid-connected structures is conducted. Only if DC breaker technology for BESS is broken through, battery clusters connected through non-isolated DC/DC converter is both cost-effective and high-efficient, making it more suitable for integration into large-scale BESS systems.

1 Introduction

Battery Energy Storage System (BESS) is a type of energy storage system that stores electrical energy in batteries in the form of chemical energy, which can store and release energy flexibly during the charging and discharging processes of the battery. With advantages of high energy density, large capacity, good dynamic response capability, and strong flexibility, BESS can satisfy the requirements of large-capacity energy storage facilities in the future [1].

During periods of low electricity demand in the grid, BESS can be controlled to be an active load for the main distribution grid, and during periods of high electricity demand in the grid, BESS can be controlled to be a source for the main distribution. In this way, BESS can be used to relieve the significant peak-to-valley pressure faced by the current power supply, reducing energy wastage and installed capacity requirements, minimizing line losses, and saving investment costs.

The typical structure of BESS is shown in Fig.1(a), which mainly consists of battery system, power conversion system (PCS), and battery management system (BMS) [2]. Battery system is the primary component of the BESS and can operate in two modes: charging mode and discharging mode. As shown in Fig.1(b), battery system can be divided into three levels: battery cells, battery modules, and battery clusters. Multiple battery cells are connected in series or parallel to form a battery module, and multiple battery modules are connected in series or parallel to form a battery cluster. PCS is used to facilitate the energy exchange between

battery system and the grid [3]. Battery cluster serves as the basic output unit for grid connection, with DC voltage transformed through PCS and connected to the main AC grid. The configuration of PCS represents the grid-connected structure of the battery system. BMS collects information from various devices within BESS to ensure the safe operation of batteries [4].

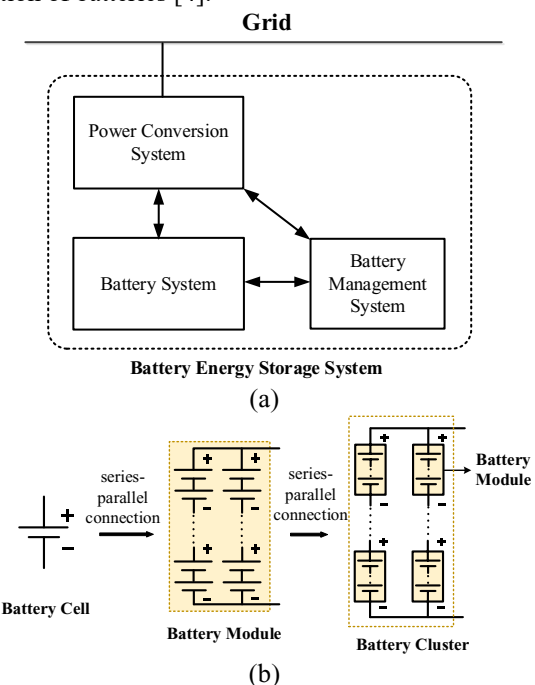


Fig. 1 Structure of battery energy storage system.
(a)overall composition, (b) structure of battery system.

The grid-connected structures of battery clusters impact the DC fault characteristics of DC line faults in BESS significantly. Existing research mainly focuses on the study of short-circuit faults between individual battery cells within the battery system [5-6], lacking analysis of the characteristics of DC line faults in BESS under different grid-connected structures.

To fulfill the research gap, the DC line fault characteristics and requirements for current interruption of BESS are demonstrated in this paper based on different grid-connected structures. In Section 2, three basic grid-connected structures of BESS are primarily introduced. In Section 3, for each grid-connected structure, equivalent circuit and the numerical calculation method for pole-to-pole faults are proposed, theoretical analysis results are validated through PSCAD simulation. In Section 4, a comparison of the three grid-connected structures is presented.

2 Brief of grid-connected structures for BESS

In order to accurately clarify the characteristics of DC faults under various grid-connected structures of BESS and further refine the protection schemes for BESS, it is necessary to conduct detailed analysis based on different grid-connected structures. Three basic grid-connected structures are introduced as follow.

2.1 Battery clusters connected directly (structure_1)

The topology of structure_1 is shown in Fig.2(a), where each battery cluster is directly connected to DC/AC converter in parallel, and increasing the number of parallel battery clusters can enhance the capacity of BESS. This grid-connected structure utilizes only DC/AC converter for energy conversion, requiring fewer power semiconductors and resulting in higher energy conversion efficiency. Under structure_1, in order to match the DC side voltage with the AC side voltage, a large number of battery cells need to be connected in series within each battery cluster to output a higher voltage level. However, due to differences in individual cell parameters and operating temperatures, actual output power imbalances and circulating currents may occur between different clusters. This circulating current leads to a gradual amplification of cluster-to-cluster differences over time and affects the internal state of each cluster within the entire battery system, increasing the difficulty of power balance control. Hence, resolving these issues is essential in practical applications to enhance the operational efficiency of BESS.

2.2 Battery clusters connected through non-isolated DC/DC converter (structure_2)

The topology of structure_2 is shown in Fig.2(b). The battery clusters are boosted by non-isolated DC/DC converters, and then the power exchange with the AC grid is carried out through DC/AC converters. A DC/DC converter is installed at the front end of each battery cluster to regulate the output voltage and achieve balanced power distribution among the clusters, thereby eliminating imbalance caused by individual

differences and effectively suppressing circulating currents. Non-isolated bidirectional DC/DC converters are typically implemented using the Buck-Boost circuit. The Buck-Boost converter features a simple structure, low control complexity, good economy, and high conversion efficiency. However, it lacks electrical isolation function and may lead to interference issues between devices, which is detrimental to the safe and reliable operation of the system.

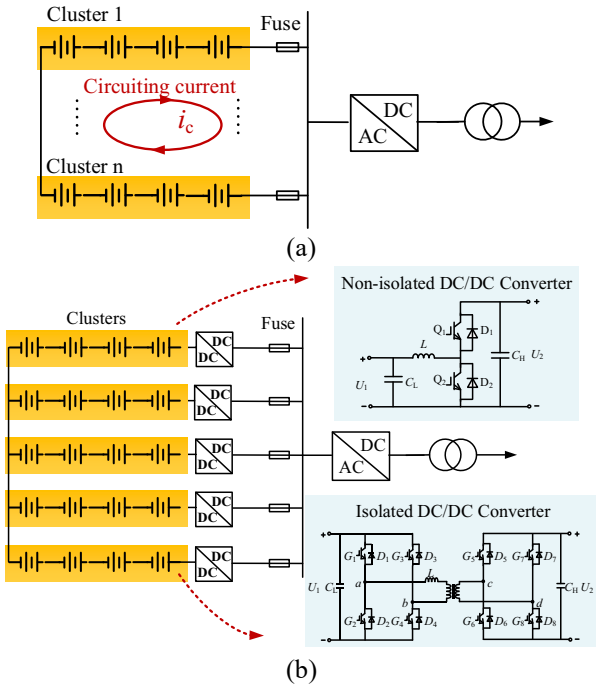


Fig. 2 Three grid-connected structures for BESS. (a) structure_1, (b) structure_2 and structure_3.

2.3 Battery clusters connected through isolated DC/DC converter (structure_3)

The topology of structure_3 is shown in Fig.2(b). The difference between structure_2 and structure_3 lies in the DC/DC converter structures: Structure_3 uses isolated DC/DC converters for energy conversion, while structure_2 employs non-isolated DC/DC converters. DAB is a typical isolated DC/DC converter, which utilizes a high-frequency transformer to achieve electrical isolation, ensuring the safe and reliable operation between the grid and the battery system. By isolating the battery cluster from the DC bus, it prevents the flow of current from the battery cluster to the opposite side of DAB, effectively eliminating potential circulating current issues among clusters. However, this approach has some drawbacks, mainly including a complex structure, higher costs, and the need for multiple sets of isolation drive circuits. Additionally, due to the bidirectional energy transfer requiring the use of high-frequency transformers, this results in reduced efficiency and increased costs.

Both structure_2 and structure_3 achieve inter-cluster balance control by installing DC/DC converters at the front end of the battery clusters, resolving circulating current issues among different clusters that are present in structure_1. Furthermore, by adjusting the DC/DC converter, the output

voltage of battery clusters can be matched with the DC side voltage of the DC/AC converter, reducing the voltage level of the battery clusters and thus reducing the difficulty for balancing and monitoring in BMS.

3 Fault analysis for different grid-connected structures

3.1 Numerical calculation method of fault current

To simplify the analysis, a battery cluster is equivalent to an electrochemical model of a single battery in this paper. As shown in Fig.2, the improved Shepherd battery model consists of a controllable voltage source and a constant resistor (r) connected in series. The internal electromotive force (E) and the output voltage of the battery model (v_{batt}) can be represented as (1) and (2) respectively. Here, E_0 is the constant voltage of the battery, K is the polarization voltage, Q is the battery capacity, SOC is the state of charge, and A and B are the exponential term coefficients. i_{batt} is the output current of the battery.

$$\left\{ \begin{array}{l} E = E_0 - K \cdot \frac{1}{SOC} + A \cdot e^{-B \cdot Q \cdot (1-SOC)} \\ SOC = \frac{Q - \int i_{batt} dt}{Q} \end{array} \right. \quad (1)$$

$$v_{batt} = E - i_{batt}r \quad (2)$$

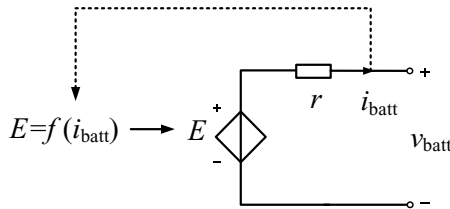


Fig. 3 Schematic diagram of the battery model.

In the event of a fault in DC line of a BESS, pole-to-pole faults are the most serious, which have a significant impact on the overall stability of the system. Therefore, the following analysis is primarily focused on pole-to-pole faults and assumes that the battery cluster is in discharging mode.

3.1.1 Fault analysis of BESS with structure_1

In structure_1, multiple battery clusters are connected in parallel first and then collectively integrated into the DC bus. When a pole-to-pole fault occurs on the DC line connected at both ends of the battery cluster, the fault equivalent circuit is shown in Fig.3. Assuming the equivalent resistance and inductance of the line between the battery cluster and the fault point are R_l and L_l , and the short-circuit resistance is R_f .

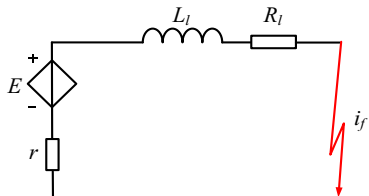


Fig. 4 Fault equivalent circuit in structure_1.

The discharge loop is directly formed between the battery and the fault point. Based on Fig.3, the fault loop equation with fault current (i_f) as a state variable can be expressed as (3). (3) is a first-order dynamic circuit, where $R = R_l + R_f$.

$$L_l \frac{di_f}{dt} + (R + r)i_f = E \quad (3)$$

Assuming the initial time of the fault, the current on the DC line is I_0 . By solving (3), the expression for i_f can be obtained as (4). From (4), it is known that the fault current rises very quickly.

$$i_f = I_0 e^{\frac{-R+r}{L_l} t} + \frac{E}{R + r} \quad (4)$$

After the transient component decays, the circuit reaches a steady state, and i_f is only determined by the internal characteristics of the battery and the fault distance.

3.1.2 Fault analysis of BESS with structure_2

In structure_2, a battery cluster is connected to the DC bus through a Buck-Boost converter. When the battery cluster is in discharging mode, Q_1 is in off-state, and Q_2 is in on-state, and the direction of inductor current (i_L) is shown in Fig.5. After a pole-to-pole fault on the DC line on the high-voltage side of the Buck-Boost converter, the fault equivalent circuit is shown in Fig.5. At the moment of fault occurrence, Q_2 immediately turns off to self-protection. Based on the fault characteristics after the fault occurs, the development of fault mainly goes through two stages [7-8].

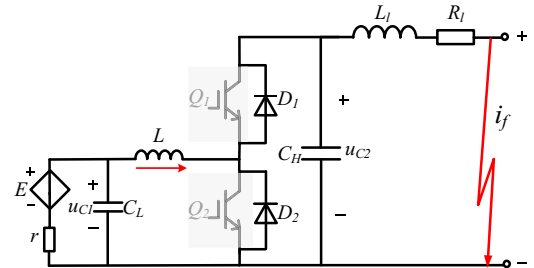


Fig. 5 Schematic diagram of equivalent circuit in structure_2.

Stage 1: the C_H discharge stage. The fault circuit is shown in Fig.5, where D_1 conducts, and D_2 withstands reverse voltage at both ends to remain off-state.

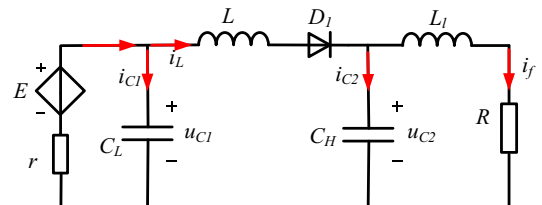


Fig. 6 Fault equivalent circuit of stage 1 in structure_2.

According to the fault circuit, the expression for the fault circuit in this stage can be obtained as (5), with low-voltage side voltage of Buck-Boost converter (u_{C1}), high-voltage side voltage (u_{C2}), i_L and i_f as state variables. Assuming the initial values of the state variables as $i_f(0) = 0$, $i_L(0) = I_{L0}$, $u_{C1}(0) = U_{C10}$, $u_{C2}(0) = U_{dc}$.

$$\begin{bmatrix} \frac{du_{C1}}{dt} \\ \frac{du_{C2}}{dt} \\ \frac{di_L}{dt} \\ \frac{di_f}{dt} \end{bmatrix} = \begin{bmatrix} -\frac{1}{rC_L} & 0 & -\frac{1}{C_L} & 0 \\ 0 & 0 & \frac{1}{C_H} & -\frac{1}{C_H} \\ \frac{1}{L} & -\frac{1}{L} & 0 & 0 \\ 0 & \frac{1}{L_l} & 0 & -\frac{R}{L_l} \end{bmatrix} \begin{bmatrix} u_{C1} \\ u_{C2} \\ i_L \\ i_f \end{bmatrix} + \begin{bmatrix} \frac{1}{rC_L} \\ 0 \\ 0 \\ 0 \end{bmatrix} E \quad (5)$$

According to (5), the fault current in this stage is solely provided by C_H . The discharge circuit of C_H forms a first order zero-input circuit, causing i_f to rise rapidly. Due to the presence of L , i_L cannot undergo a sudden change. The battery cluster and C_L charge towards C_H , but at a much slower rate compared to the discharge rate of C_H , resulting in a rapid decrease in u_{C2} .

Stage 2: the stage of all diodes conduction. At $t = t_1$, C_H is fully discharged, entering the phase of full conduction of the diodes. Both D_1 and D_2 conduct simultaneously, clamping u_{C2} to 0. Assuming the initial values for the state variables in this stage are $i_f(t_1) = I_1$, $i_L(t_1) = I_{L1}$, $u_{C1}(t_1) = U_{C1}$, $u_{C2}(t_1) = 0$. Because $u_{C2}(0) = 0$, the circuit can be decomposed into two parts as shown in Fig.7 for separate analysis. It is worth noting that the direction of i_L is opposite to the forward conduction direction of D_2 in Fig.7(a), for the sake of analysis. The total current flowing through D_2 (i_{D2}) is given by (6), and still complies with its unidirectional conduction characteristic.

$$i_{D2}(t) = i_f(t) - i_L(t) \quad (6)$$

According to the fault circuit diagram in Fig.7(b), the freewheeling diode circuit forms a first-order zero-input circuit, and the expression for the fault current is given by (7). Based on the fault circuit diagram in Fig.7(a), the discharge circuit of the low-voltage side forms a second-order circuit, and the fault circuit equation with i_L as state variable is shown in (8).

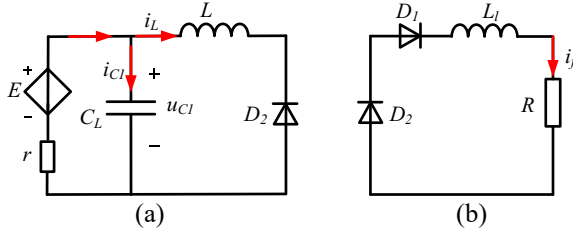


Fig. 7 Fault equivalent circuit of stage 2 in structure_2. (a) the discharge circuit of the low-voltage side, (b) the freewheeling diode circuit.

$$i_f(t) = I_1 e^{-\frac{R}{L_l}(t-t_1)} \quad (7)$$

$$rLC_L \frac{d^2 i_L}{dt^2} + L \frac{di_L}{dt} + ri_L = E \quad (8)$$

The state equation for this stage can be derived from (7) and (8) as:

$$\begin{bmatrix} \frac{du_{C1}}{dt} \\ \frac{du_{C2}}{dt} \\ \frac{di_L}{dt} \\ \frac{di_f}{dt} \end{bmatrix} = \begin{bmatrix} -\frac{1}{rC_L} & 0 & -\frac{1}{C_L} & 0 \\ 0 & 0 & 0 & 0 \\ \frac{1}{L} & 0 & 0 & 0 \\ 0 & 0 & 0 & -\frac{R}{L_l} \end{bmatrix} \begin{bmatrix} u_{C1} \\ u_{C2} \\ i_L \\ i_f \end{bmatrix} + \begin{bmatrix} \frac{1}{rC_L} \\ 0 \\ 0 \\ 0 \end{bmatrix} E \quad (9)$$

After i_{D2} decreases to zero, D_2 is turned off again, and C_H undergoes charging and discharging, bringing the fault back to stage 1. After a certain period, the system progresses to stage 2, continuing in this cycle. When the system reaches a steady state, C_H stops charging and discharging, and only the battery cluster continues to supply current to the fault point. The steady-state fault current depends on the battery discharge status. As the discharge time increases, the state of charge (SOC) gradually decreases, and the fault current also decreases. This process typically lasts for several hours.

3.1.3 Fault analysis of BESS with structure_3

In structure_3, the battery cluster is connected to the DC bus through the DAB converter. Under normal conditions, the direction of energy flow on the DAB converter is shown in Fig.8(a). When a pole-to-pole fault occurs on the output side DC line of the DAB converter, the equivalent circuit is shown in Fig.8(b).

After the fault occurs, IGBTs in the two H-bridges immediately shut down. The DAB has electrical isolation, battery cluster cannot supply current to the fault point. Therefore, the fault development process can be divided into two stages as shown in Fig.8(b): the capacitor discharge stage and the diode conduction stage.

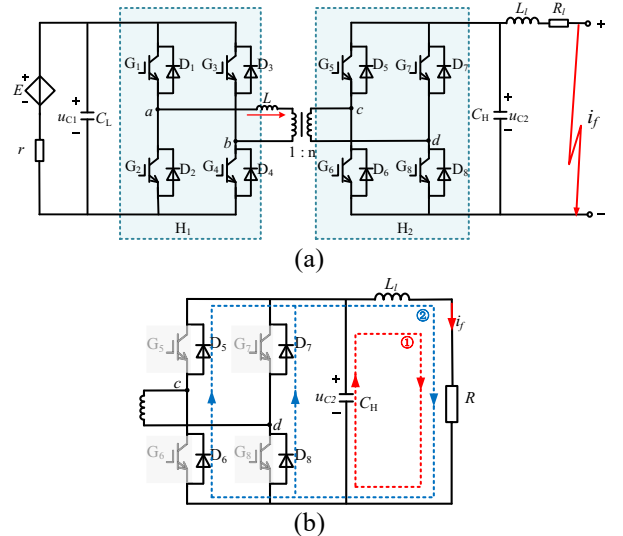


Fig. 8 (a) Schematic diagram of equivalent circuit in structure_3, (b) Fault equivalent circuit of structure_3.

Stage 1: the capacitor discharge stage. C_H discharges towards the fault point through L_l and R_l , causing u_{C2} to gradually decrease. The fault loop is shown in Fig.8(b). The corresponding second-order fault loop equation can be derived based on the circuit structure:

$$L_t C_H \frac{d^2 u_{C2}}{dt^2} + R C_H \frac{du_{C2}}{dt} + u_{C2} = 0 \quad (10)$$

The characteristic roots (λ_1 and λ_2) of the solved equation are (11). In the case where the fault has the greatest impact on the grid, the circuit is in underdamped state, and λ_1 and λ_2 are a pair of complex conjugate roots.

$$\lambda_{1,2} = -\alpha \pm j\beta = -\frac{R}{2L_t} \pm j\sqrt{\frac{1}{L_t C_H} - \frac{R^2}{4L_t^2}} \quad (11)$$

Assuming the fault happen at $t = 0$, $u_{C2}(0) = U_{C2}$, $i_f(0) = 0$, u_{C2} and i_f can be expressed as (12) and (13).

$$u_{C2}(t) = U_{C2} \cdot \frac{\sqrt{\alpha^2 + \beta^2}}{\beta} e^{-\alpha t} \cos(\beta t - \theta) \quad (12)$$

$$i_f = C_H \frac{du_2}{dt} = \frac{U_{C2}}{\beta L_t} e^{-\alpha t} \sin(\beta t) \quad (13)$$

Where $\theta = \arctan(\alpha / \beta)$.

Stage 2: the diode conduction stage. At $t_2 = (\theta + \pi/2) / \beta$, u_{C2} drops to 0. L_t continues to discharge the fault point through the freewheeling diodes $D_5 \sim D_8$, causing i_f to gradually decrease. The fault loop is shown in Fig.8(b). At this stage, the initial value of i_f is given by (14), and the expression for the fault current can be derived as (15).

$$I_{f2} = i_f(t_2) = \frac{U_{C2}}{L_t \sqrt{\alpha^2 + \beta^2}} e^{-\alpha t_2} \quad (14)$$

$$i_f(t) = I_{f2} e^{-\frac{R}{L_t}(t-t_2)} \quad (15)$$

Once the energy in L_t is fully discharged, the system reaches a steady state, and the fault current in the circuit drops to zero, achieving self-clearing of the fault.

3.2 Simulation verification and result discussion

The above theoretical analysis is verified through simulation using PSCAD/EMTDC. The simulation model of BESS as shown in Fig.9 is constructed, with the DC/DC converter structured as both Buck-Boost and DAB. The parameters used in the simulation are provided in Table 1.

The fault characteristics of the three grid-connected structures in BESS are compared. At $t = 0$ ms, a pole-to-pole fault (fault1) occurs on the DC line connecting to the battery clusters, the fault current is shown in Fig.10. At $t = 3$ ms, the fault current in structure_1 rises to 78.32kA, reaching a near steady-state value of 103.20kA by $t = 13$ ms. In structure_2, the battery clusters also feed into the fault point. At $t = 3$ ms, the fault current rises to 23.34kA, reaching 65.29kA by $t = 13$ ms. The rise rate of fault current within 3ms for structure_1 is approximately 3.36 times that of structure_2, and the time to reach steady-state fault current is approximately 1/4 of the latter. Compared to structure_1, the fault propagation speed is reduced in structure_2 as Buck-Boost converters are installed at the front end of the battery clusters. In structure_3, at $t = 0.31$ ms, the fault current reaches its peak, with the peak

value of 9.67kA. At $t = 3$ ms, the fault has entered the diode conduction stage, and the fault current has decayed to 2.47kA, reaching nearly 0 by $t = 13$ ms.

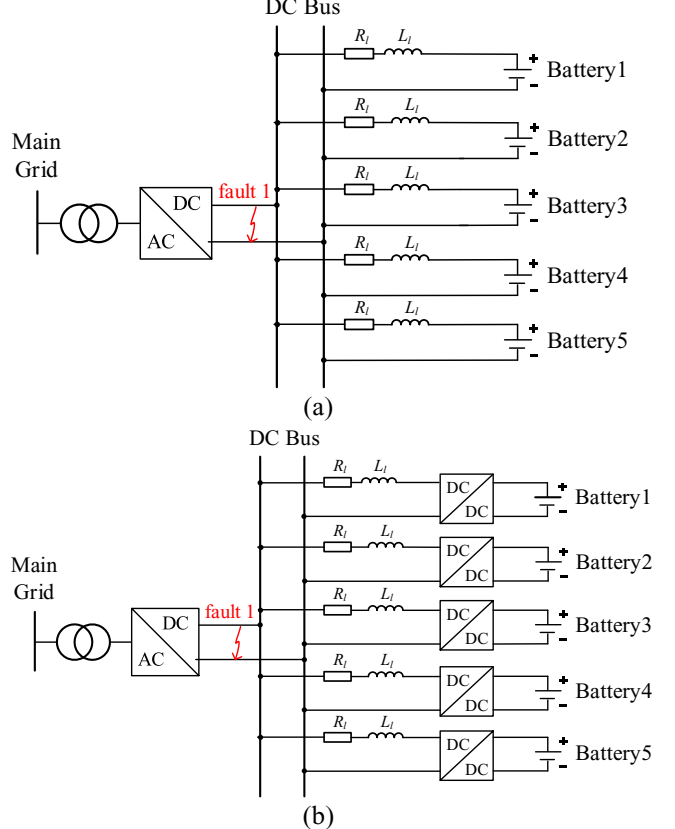


Fig. 9 Schematic Diagram of pole-to-pole fault on DC line. (a) structure_1, (b) structure_2 and structure_3.

Table 1 Simulation Parameters

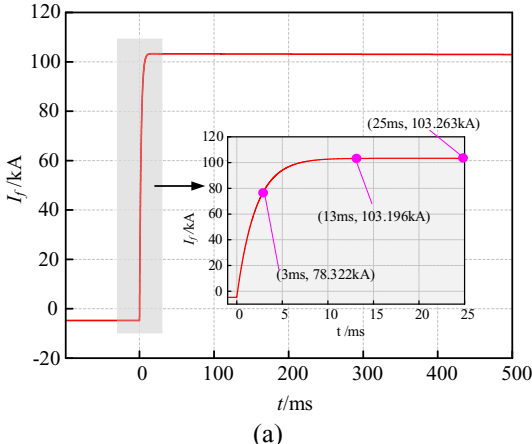
Parameters	Value	
Rated voltage of battery cluster (V)	600	
Battery cluster capacity (Ah)	720	
The number of battery cluster	5	
initial SOC of battery cluster	1	
DC bus voltage (V)	750	
L_t (μ H)	68.275	
R_t (m Ω)	28.0	
DC/DC output power (kW)	100	
C_L (μ F)	350	
Buck-Boost	C_H (μ F)	100
	L_t (μ H)	600
	C_L (μ F)	25
DAB	C_H (μ F)	600
	L (μ H)	25

Based on the simulation verification results, the DC fault interruption requirements for the three grid-connected structures are as follows:

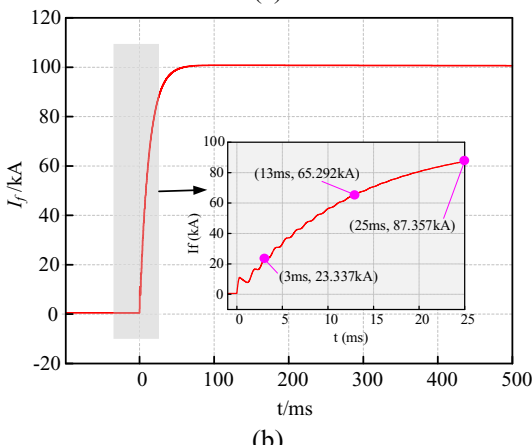
(1) Under structure_1, the fault develops rapidly, and protective devices cannot respond and act in a timely manner. The fault current will cause significant impact and damage to power electronic devices in the grid. The steady-state short-circuit current is too high, exceeding the breaking capacity of existing DC protection devices. Moreover, imbalance between battery clusters can lead to cluster-to-cluster circulation. Therefore, this grid-connected structure should be avoided in BESSs.

(2) Under structure_2, the Buck-Boost converter is a non-isolated DC/DC converter that provides a discharge path for the battery clusters to the fault point. The fault current is the sum of the discharge currents of all battery clusters, and the steady-state fault current exceeds 100kA. From Fig.10(b), it is evident that the faster the operation speed of the protective device, the smaller the current value that needs to be interrupted, indicating a high requirement for the speed and reliability of the protective device.

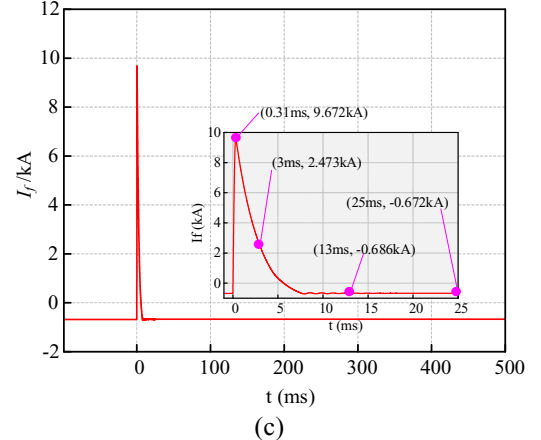
(3) Under structure_3, the isolated DAB converter achieves electrical isolation, and the fault current is provided solely by the discharge of the DAB high-voltage side capacitors. After the capacitor discharge, the fault current gradually decays to zero, achieving self-clearing of the fault. The difficulty of interrupting the short-circuit fault is significantly reduced, and the requirements for current interruption capability and speediness of protective devices are lowered, which widens the selection range for protective devices.



(a)



(b)



(c)

Fig.10 The fault currents for (a) structure_1, (b) structure_2, (c) structure_3.

4 Comparison

In order to compare the three grid-connected structures, Table 2 provides a comparison of the economic viability, transmission efficiency, and output characteristics of battery clusters for the three grid-connected structures of the simulation model in Section 3.

First, from the economic perspective, the main power electronic devices for the three grid-connected structures are IGBTs and diodes. The three grid-connected structures have the same AC-side structure, so only the structural differences on the DC-side are discussed. Structure_1 has no power electronic devices on the DC-side, while the number of IGBTs in structure_3 is four times that of structure_2. In terms of cost, the cost of structure_2 consists of 10 IGBTs and 5 series inductors of Buck-Boost converters, while the cost of structure_3 consists of 40 IGBTs, 5 inductors and transformers in DABs. Taking the cost of structure_2 as the baseline value of 1p.u., the cost of structure_3 is approximately 3.9p.u..

From the perspective of energy transfer efficiency, only losses in the DC/DC stage are analyzed. The losses of the Buck-Boost converter mainly include device losses and inductor losses, while the losses of the DAB converter mainly include device losses and transformer losses. Compared to device losses, the values of inductor losses and transformer losses are very small and can be neglected. So this paper just focus on device losses. Thermal simulation models for the Buck-Boost and DAB converters are established in PLECS, with a rated power of 100kW for both converters using FF600R17ME4P IGBT modules. The device losses for the Buck-Boost and DAB converters are shown in Table 2, and the device losses of structure_3 are 2.5 times that of structure_2.

From the perspective of addressing inter-cluster circulating current issues, differences in internal parameters of individual batteries and environmental parameters in structure_1 lead to cluster-to-cluster circulating current. However, in structure_2 and structure_3, DC/DC converters are deployed at the output of each battery cluster to regulate

the output voltage of the battery cluster, ensuring its consistency and effectively suppressing cluster-to-cluster circulating current.

Table 2 Comparison of different grid-connected structures

	Structure_1	Structure_2	Structure_3
The number of IGBT	0	10	40
Cost (p.u.)	-	1	3.9
DC/DC power device loss (delivered power set at 100kW)	-	1862.68	6834.70
Whether the inter-cluster circulation current exists	Yes	No	No

In summary, based on the comprehensive comparison, structure_2, while optimizing the output characteristics of the battery clusters, combines economic and efficient features, making it the most suitable grid-connected structure for existing BESSs. According to the analysis of fault interruption requirements, the BESS with structure_2 is suitable for implementing line protection by DC circuit breaker with current-limiting function.

5 Conclusion

Starting from the perspective of grid-connected structures in BESSs, the characteristics of DC line faults and the requirements for fault interruption in BESSs are demonstrated in this paper. Theoretical analysis and verification through PSCAD simulations are conducted for each grid-connected structure under pole-to-pole faults. The comparison shows that as long as DC breaker for BESS could be broken through, structure_2, with advantages of cost-effective and high-efficient, is more suited for existing BESSs.

6 Acknowledgements

This work was supported by Science and Technology Project of the State Grid Cooperation of China (5108-202218280A-2-440-XG).

7 References

- [1] M. Liu et al., 'A Review of Power Conversion Systems and Design Schemes of High-Capacity Battery Energy Storage Systems,' in IEEE Access, 2022, 10, pp. 52030-52042.
- [2] G. Wang et al., 'A Review of Power Electronics for Grid Connection of Utility-Scale Battery Energy Storage Systems,' in IEEE Transactions on Sustainable Energy, vol. 7, no. 4, pp. 1778-1790, Oct. 2016.
- [3] M. Liu et al., 'A Review of Power Conversion Systems and Design Schemes of High-Capacity Battery Energy Storage Systems,' in IEEE Access, 2022, 10, pp. 52030-52042.
- [4] M. T. Lawder et al., 'Battery Energy Storage System (BESS) and Battery Management System (BMS) for Grid-Scale Applications,' in Proceedings of the IEEE, vol. 102, no. 6, pp. 1014-1030, June 2014.
- [5] K. Zhang, X. Hu, Y. Liu, X. Lin and W. Liu, 'Multi-fault Detection and Isolation for Lithium-Ion Battery Systems,' in IEEE Transactions on Power Electronics, vol. 37, no. 1, pp. 971-989, Jan. 2022.
- [6] M. Seo, M. Park, Y. Song and S. W. Kim, 'Online Detection of Soft Internal Short Circuit in Lithium-Ion Batteries at Various Standard Charging Ranges,' in IEEE Access, 2020, 8, pp. 70947-70959.
- [7] J. Yang, J. E. Fletcher and J. O'Reilly, 'Short-Circuit and Ground Fault Analyses and Location in VSC-Based DC Network Cables,' in IEEE Transactions on Industrial Electronics, vol. 59, no. 10, pp. 3827-3837, Oct. 2012.
- [8] Z. Zhang, Q. Chen, R. Xie and K. Sun, 'The Fault Analysis of PV Cable Fault in DC Microgrids,' in IEEE Transactions on Energy Conversion, vol. 34, no. 1, pp. 486-496, March 2019.

Factors Affecting Battery Unit Contributions to Fault Currents in Grid-connected Battery Storage Systems

S. A. Saleh

ECE Department, UNB
Fredericton, NB, Canada
asaleh@unb.ca

E. Ozkop

Electrical & Electronics Eng.
KTU, Trabzon, Turkey
eozkop@ktu.edu.tr

M. Valdes

ABB Industrial Solutions
Cary, North Carolina, USA
Marcelo.valdes@us.abb.com

A. Yuksel

TUBITAK MAM Energy Inst.
Ankara, Turkey
ahmet.yuksel@tubitak.gov.tr

M. Haj-Ahmed

Department of Electrical Eng.
Uni. of Jordan, Amman, Jordan
M.Hajahmed@ju.edu.jo

S. G. Sanchez

Centro de Estudios de Energia
Universidad de Cienfuegos, Cienfuegos, Cuba
zgarcia@ucf.edu.cu

C. Mardegan

EngePower
Osasco 06114-022, Brazil
claudio.mardegan@engepower.com

Abstract—This paper investigates factors affecting the contributions of battery units to fault currents in grid-connected battery storage systems (BSSs). The work in this paper is intended to examine effects of the state-of-charge (SOC) on battery currents that are drawn due to faults. This paper also examines impacts of charger controller actions on the currents drawn from battery units to faults in grid-connected BSSs. The impacts of the SOC and charger controller on battery currents due to faults, are examined for the Lead-Acid, Lithium-Ion, and Nickle-Cadmium battery units. Examination results show that the battery currents due to faults are directly dependent on the SOC. Moreover, these results show that actions of charger controller can support the battery terminal voltage, thus preventing the fast reduction of the SOC. The support of the battery terminal voltage helps in limiting the currents drawn from battery units during faults. The effects of the SOC and charger controller are verified using a 1 MW, 3 ϕ grid-connected BSS, which has Lead-Acid battery units. Several faults have been created during charging and discharging operations, and at different values of SOC. Test results confirm the direct dependence of battery currents (due to faults) on the SOC. In addition, obtained results demonstrate the ability of charger controller to limit the currents drawn from battery units due to faults in different parts of a grid-connected BSS.

Index Terms—Grid-connected battery storage systems, grid-connected power electronic converters, IEEE Standard 946, IEEE Standard 1375, and power system faults.

I. INTRODUCTION

A. General

High power rated battery storage systems (BSSs) have gained popularity in power systems due to their fast response, high power density, and dynamic charge/discharge characteristics. Applications of BSSs in power systems include supporting voltage/frequency stability, improving the power quality, and mitigating variations of the power generated by renewable energy systems [1]–[8]. Despite their capabilities to enhance power systems functions, the interconnection of BSSs can create challenges for protection systems and devices. Such challenges are created by [1]–[7]:

- bi-directional power flows to charge/discharge the BSS;
- actions of the BSS controller to regulate the power flow;
- features of interfacing power electronic converters (PECs);
- contributions of the BSS to fault currents.

References [9], [10], [11], and [12] provide various aspects for designing accurate and reliable protection systems for interconnected BSSs. Test results of these protection systems have demonstrated their abilities to accommodate bi-directional

power flows, actions of BSS controllers, and features of interfacing PECs [12]. However, the accurate determination of BSS contributions to fault currents has not been fully addressed, when considering the actions BSS controller and features of the interfacing PEC.

B. Overview of IEEE Standard 946 and IEEE Standard 1375

Battery storage systems (BSSs) have become essential components in many industrial systems, including data centers, communications systems, renewable energy systems, uninterrupted power supplies, power systems, and others. In these applications, a BSS is considered to have a dc stage and an ac stage that are fed from the utility grid via an interconnection transformer as shown in Fig. 1. The dc stage is composed of the battery units, and protection devices. The ac stage is composed of the interfacing PEC, grid-tie filter, interconnection transformer, grid-synchronizing, and protective devices [2]–[5]. Several industrial sectors have developed standards and best practices for the design, operation, and protection for grid-connected BSSs [1]–[8].

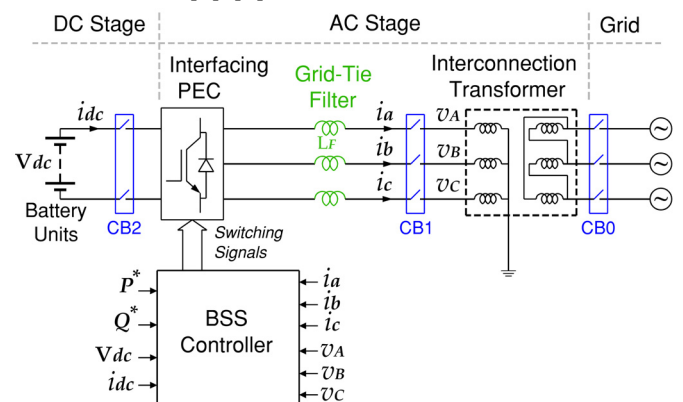


Fig. 1. A circuit diagram for a 3 ϕ grid-connected BSS.

Similar to other components of a power system, grid-connected BSSs can experience various types of faults, which can occur in the dc stage, ac stage, and grid. However, due to the charging and discharging operation of battery units, the behavior of a grid-connected BSS during faults can be influenced by several factors. For example, a fault in the dc stage during the charging operation may trigger a different current from that during the discharging operation. An other example can be a fault in the ac stage may trigger a discharge current

that is dependent on the state-of-charge of the battery units [1]–[6], [12], [13]. In order to avoid equipment damages and/or service interruptions, grid-connected BSSs have to be featured with adequate protective devices (relays, circuit breakers, and fuses) with proper sizing and settings [1]–[4]. The selection of such protective devices requires determining currents that are triggered by faults at different stages of a grid-connected BSS.

IEEE Standard 1375

This standard [4] details recommended practices for the protection of stationary battery units. These battery units are typically connected to a dc bus that may feed some dc loads, and be connected to several PECs (chargers and inverters). The IEEE Standard 1375 addresses the short-circuit in battery units, grounding of battery units, and protection devices for battery units. For faults in the dc stage, the IEEE Standard 1375 sets the battery contribution to the fault current based on:

- the battery time-constant;
- the equivalent impedance as seen from the fault location;
- the battery rated terminal voltage;

IEEE Standard 946

This standard [2] provides recommendations for designing stationary BSSs with a dc bus, dc loads, and multiple PECs (chargers and inverters). The IEEE Standard 946 provides guidance for designing protection systems for stationary BSSs, where protective devices are selected for ac and dc stages based on the maximum possible current triggered by faults in the ac and dc stages. This standard states that the maximum possible fault current is the sum of contributions by the battery units, active dc loads (connected to the dc bus), and filters on both sides of the charging PECs. The IEEE Standard 946 sets the contributions of battery units to faults in the ac or dc stages based on their rated voltages and equivalent impedance as seen from the fault location [2], [9]–[13].

Other reported research works [14], [15] have investigated the protection of BSSs with different structures. In these works, the selection of the protective devices has been based on the IEEE standards 1375 and 946. Moreover, the fault detection has been adapted from methods used in PEC protection as discussed [12], [16], [17]. Nonetheless, these works have not addressed the battery units contributions to fault currents.

C. Paper Objectives and Contributions

Currents triggered by faults in grid-connected BSS have components contributed by the battery units and charger PEC. The existing methods to estimate these contributions do not consider the effects of the SOC and actions of the charger PEC. This paper aims to investigate the factors affecting the currents drawn from battery units due to faults in grid-connected BSSs. The objectives of this paper can be summarized as:

- to examine effects of the controller actions on the currents drawn from battery units due to faults;
- to examine the effects of the SOC on the battery currents during faults in a grid-connected BSS;

Achieving these objectives ensures the following contributions:

- i) the factors affecting the currents drawn from battery units due to faults in grid-connected BSSs;
- ii) the verification of these factors using a 1 MW grid connected BSS.

II. FAULT CURRENTS IN BATTERY STORAGE SYSTEMS

There exist several approaches to determine fault currents in battery storage systems. Among these approaches are the IEEE Standard 1375 and IEEE Standard 946, which are intended for stationary battery storage systems. Fig. 2 depicts the single line diagram for a stationary battery storage system.

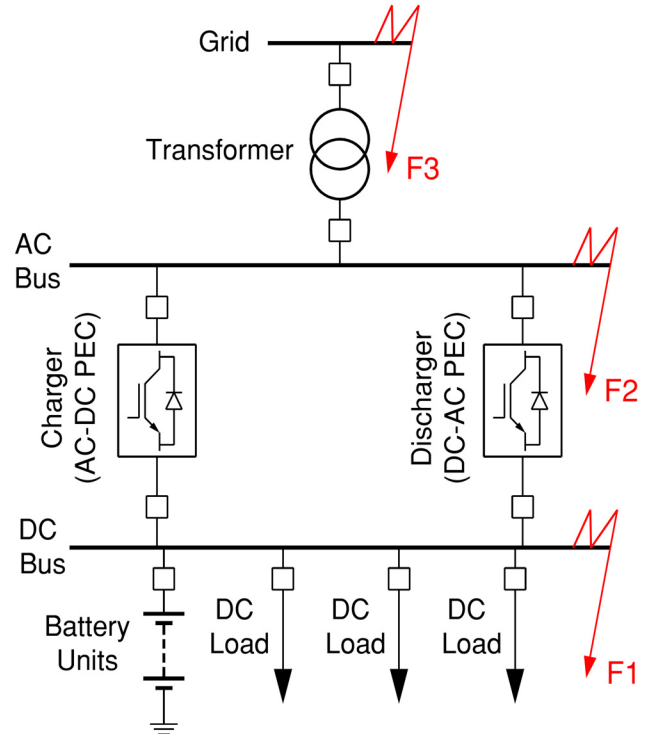


Fig. 2. A single line diagram of a stationary battery storage systems [2], [4]. The IEEE standards 1375 and 946 determine a fault current, in a stationary battery storage systems, as a combination of contributions by the battery units and interfacing PECs (chargers and/or inverters) [2]–[5].

A. Calculating Fault Currents Using IEEE Standard 1375

The IEEE Standard 1375 sets the maximum current triggered by a fault in the dc bus (fault F1 in Fig. 2) as [4]:

$$(i_{F1})_{\max} = \frac{V}{R} \left(1 - e^{-\frac{t}{\tau_{bs}}} \right) + 10 (I_{PEC})_{\text{Rated}} \quad (1)$$

where $(i_{F1})_{\max}$ is the maximum fault current triggered by F1, V is the pre-fault voltage on the terminals of the battery units, R is the equivalent resistance of the battery units, τ_{bs} is battery short-circuit time constant (see Table 2 in reference [4]), and $(I_{PEC})_{\text{Rated}}$ is the rated current of the charger. The IEEE Standard 1375 provides guidance for determining the value of R using the discharge characteristic curve of the battery units.

Remarks Regarding Equation (1)

- (a) The value of $(i_{F1})_{\max}$ is intended only for determining the size and interruption capacity of protective devices to be installed in the dc bus.
- (b) The current contributed by the battery units to F1 is assumed to increase during the interval of $5 \times \tau_{bs}$ after the start F1. Nonetheless, this interval can be long enough for a significant reduction V , thus limiting the current contributed by the battery units.

- (c) The current contributed by the charger can not exceed the rated pulsing current of individual switching elements comprising the charger. Such a current is less than $10(I_{PEC})_{\text{Rated}}$.

B. Calculating Fault Currents Using IEEE Standard 946

This standard determines the maximum current triggered by a fault in the dc bus (F1) as:

$$(i_{F1})_{\text{max}} = \frac{V_{Br}}{R_{eq}} + 10(I_{PEC})_{\text{Rated}} \quad (2)$$

where V_{Br} is the rated terminal voltage of the battery units, and R_{eq} is the equivalent resistance seen the location of F1. For a fault in the ac bus (Fault F2 in Fig. 2), the IEEE Standard 946 sets the maximum fault current as [2]:

$$(i_{F2})_{\text{max}} = 10(I_{PEC})_{\text{Rated}} + (i_{acI})_{\text{max}}(1 + e^{-\gamma}) \quad (3)$$

where $(i_{acI})_{\text{max}}$ is the maximum ac current provided by the inverters (see by Table 2 and Table 3 in reference [18]), and γ is give as:

$$\gamma = \frac{2\pi}{X/R} \left(0.49 - 0.1e^{-\frac{X/R}{3}} \right) \quad (4)$$

with X being the equivalent inductive impedance seen from the location of F2, and R being the equivalent resistance seen from the location of F2.

For a fault on the grid-side (fault F3 in Fig. 2), the contributions of the battery units and inverter, $(i_4)_{F3}$, are set by the IEEE Standard 946 as:

$$(i_4)_{F3} = 10(I_{PEC})_{\text{Rated}} \quad (5)$$

The grid contribution to faults on the grid-side are determined using the IEEE Standard 3002.3 as [18]:

$$(i_0)_{F3} = (i_{acG})_{\text{max}}(1 + e^{-\gamma}) \quad (6)$$

where $(i_{acG})_{\text{max}}$ is the peak ac component of the grid current (see Table 2 and Table 3 in reference [16]), and γ is determined by equation (4) for F3. The maximum current that can be triggered by F3, $(i_{F3})_{\text{max}}$, is stated as:

$$(i_{F3})_{\text{max}} = 10(I_{PEC})_{\text{Rated}} + (i_{acG})_{\text{max}}(1 + e^{-\gamma}) \quad (7)$$

Remarks Regarding Equations (3) and (7)

- The values of $(i_{F2})_{\text{max}}$ and $(i_{F3})_{\text{max}}$, determined using the IEEE Standard 946, are used only for selecting the size and interruption capacity of protective devices in the dc and ac buses.
- The contributions of battery units and inverter to faults in ac bus or grid, are limited by the rated current of the inverter.
- The contribution of the grid to fault currents in the ac stage, can be determined using the IEEE Standard 3002.3.

III. FACTORS AFFECTING FAULT CURRENTS IN GRID-CONNECTED BSSs

In general, a battery unit can deliver an extremely high current during a short-circuit on its terminals. The short-circuit current delivered by a battery unit can reach more than 40 times its rated discharge current [2]–[4], [13]–[15]. However, short-circuit currents delivered by a battery unit can be affected by the battery type, state-of-charge (SOC), protection devices, temperature, and equivalent resistance as seen from the terminals of the battery unit [17].

A. Effects of the SOC on the Short-Circuit Current

The state-of-charge (SOC) for a battery unit is critical parameter that reflects its performance and facilitates its operation. The monitoring of the SOC of a battery unit helps preventing its over-discharge and improving its functions. The impacts of the SOC on the short-circuit of a battery unit can be illustrated by the relationship between the discharge current (I_{DS}) and SOC, that is [19]:

$$I_{DS}(t) = \frac{C}{\Delta t} (\text{SOC}(t) - \text{SOC}(t - \Delta t)) \quad (8)$$

where C is nominal capacity of the battery unit in (Ah), Δt is a time interval, and t_n is set as $t_n = t - \Delta t$.

For purposes of demonstrating the effects of the SOC on the short-circuit current delivered by a battery unit, models for Lithium-Ion, Nickel-Cadmium, and Lead-Acid battery units have been created using e-TAP and MATLAB/SIMULINK software packages [20], [21]. These models have been used to test the short-circuit I_{SC} of these battery units at different values of the SOC. Each model is rated for 24 V, 20 A.h, and a rated discharge current of 8 A. Fig. 3 shows the maximum short-circuit current at different values of the SOC for each battery unit.

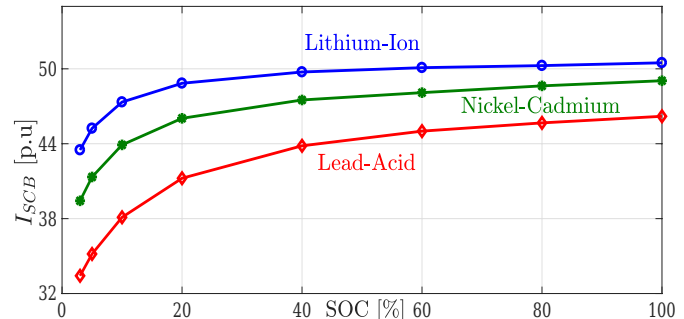


Fig. 3. The maximum short-circuit current at different values of the SOC for Lithium-Ion, Nickel-Cadmium, and Lead-Acid battery units. The base value of I_{SCB} is 8 A, and the value of Δt is $\Delta t = 10$ ms.

Fig. 3 shows that the SOC value prior to a short-circuit has a significant influence on the maximum short circuit contributed by a battery unit. In addition, Fig. 3 demonstrates that the type of a battery unit has a direct influence on the maximum short-circuit current contributed by that battery unit.

The influences of the SOC on $(I_{SC})_{\text{max}}$ are further demonstrated by a comparison with $(I_{SC})_{\text{max}}$ determined by the IEEE standards 946 and 1375 for three battery units. The internal resistances and short-circuit time constant for the Lithium-Ion, Nickel-Cadmium, and Lead-Acid battery units, are obtained from the data in references [2] and [4] as:

- Lithium-Ion battery unit: $R_B = 0.05 \Omega$;
- Nickel-Cadmium battery unit: $R_B = 0.073 \Omega$;
- Lead-Acid battery unit: $R_B = 0.104 \Omega$;
- Short-circuit time constant $\tau_{SC} = 3.3$ ms (Table 2 in [4]).

The values of $(I_{SCB})_{\text{max}}$ are determined by the IEEE standards 946 and 1375 as:

- IEEE Standard 946:

$$(I_{SCB})_{\text{max}} = \frac{V_{Br}}{R_B} \quad (9)$$

with V_{Br} being the rated terminal voltage.

- IEEE Standard 1375:

$$(I_{SCB})_{\max} = \frac{V}{R_B} \left(1 - e^{-\frac{t}{\tau_{bs}}}\right) \quad (10)$$

with V being the terminal voltage before the short circuit.

Fig. 4 shows $(I_{SCB})_{\max}$ for the three battery units determined based on the SOC, as well as the IEEE standards 946 and 1375.

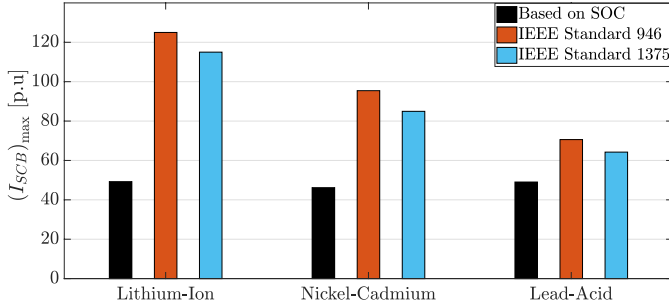


Fig. 4. The maximum short-circuit current for the tested Lithium-Ion, Nickel-Cadmium, and Lead-Acid battery units determined based on SOC= 100%, and IEEE Standards 946 and 1375. The base value of I_{SCB} is 8 A.

It can be seen from Fig. 4 that the IEEE standards 946 and 1375 yield $(I_{SCB})_{\max}$ with higher values than that determined based on SOC. These differences in $(I_{SCB})_{\max}$ are observed for the Lithium-Ion, Nickel-Cadmium, and Lead-Acid battery units.

B. Effects of Controller Actions on the Short-Circuit Current

Battery chargers are usually operated by constant voltage and/or constant current controllers. Constant voltage controllers are designed to operate the charger (ac-dc PEC) to maintain the battery terminal voltage at a constant value by adjusting the charging current. Constant current controllers are designed to operate the charger to maintain a constant charging current until the battery terminal voltage meets a desired value [22], [23]. References [22] and [23], have several designs for charger controllers.

A constant voltage controlled 3ϕ charger (thyristor or switched ac-dc PEC) produces an average dc voltage, V_{dc} , (over the n^{th} switching interval) on its dc side as [23]:

$$V_{dc}(n) = \frac{3}{2} V_{Ps} \cdot (k(n))_{CV} \quad (11)$$

where $(k(n))_{CV}$ ($0 \leq (k(n))_{CV} \leq 1$) is related to the actions of the constant voltage controller during n , and V_{Ps} is the rms value of the line voltage on the ac side of the 3ϕ charger. The value of $(k(n))_{CV}$ depends on the type of charger as:

- For a thyristor-based charger, $(k(n))_{CV}$ is:

$$(k(n))_{CV} = \cos(\alpha(n))$$

with $\alpha(n)$ being the firing angle during n .

- For a transistor-based charger, $(k(n))_{CV}$ is:

$$(k(n))_{CV} = m_a(n)$$

with $m_a(n)$ being the modulation index during n .

The output dc current during n , I_{dc} , can be stated as [22], [23]:

$$I_{dc}(n) = \frac{2(k(n))_{CV}}{\pi} \left(|i_a(n)| + |i_b(n)| + |i_c(n)| \right) \quad (12)$$

where $i_a(n), i_b(n), i_c(n)$ are the 3ϕ currents on the ac side of the charger during n . The value of $(k(n))_{CV}$ during n is set by the constant voltage controller to achieve:

$$V_{dc}(n) \xrightarrow{(k(n))_{CV}} V_{dc}^*(n) \quad (13)$$

where $V_{dc}^*(n)$ is the desired output dc voltage.

A constant current controlled charger will maintain I_{dc} fixed as long as $V_{dc} = V_{dc}^*$. For a 3ϕ charger operated by a constant current controller, the output dc voltage during n is stated as [23]:

$$V_{dc}(n) = \frac{3}{2} V_s \cdot (1 - k_{1CC} \Delta V_{dc}(n)) \quad (14)$$

where k_{1CC} is a parameter of the constant current controller, and $\Delta V_{dc}(n)$ is given as:

$$\Delta V_{dc}(n) = V_{dc}^* - V_{dc}(n)$$

The dc current, during n , produced by a 3ϕ constant current controlled charger can be expressed as [23]:

$$I_{dc}(n) = (\beta_0 + \beta_1 \Delta V_{dc}(n)) \left(|i_a(n)| + |i_b(n)| + |i_c(n)| \right) \quad (15)$$

with β_0, β_1 being parameters for the constant current controller.

A short circuit on the dc bus results in a sudden reduction of V_{dc} , thus $\Delta V_{dc}(n) \neq 0$. The sudden reduction in V_{dc} triggers a response from the charger controller to restore V_{dc} to its desired value V_{dc}^* . A constant voltage controller will increase $(k(n))_{CV}$ to restore V_{dc} , causing I_{dc} to increase (equation (12)). A similar action will be initiated by a constant current controller, which tends to achieve $\Delta V_{dc} \rightarrow 0$. This action causes I_{dc} to increase as in equation (15). Since the response of a battery unit is slower than the response of the charger controller, fast increases in I_{dc} can affect I_{SCB} (the short circuit current contributed by a battery unit).

The actions of charger controller (constant voltage or constant current) to restore V_{dc} will slow the decay of SOC, as a high current is drawn from the battery unit (due to a short circuit at the dc bus). This can be illustrated by [24]:

$$V_{dc}(n) = V_{B0} - \frac{C \cdot h_p (1 - SOC(n))}{SOC(n)} - \left(\frac{h_p}{SOC(n)} + R_B \right) (I_{DS})_{\text{Rated}} \quad (16)$$

where V_{B0} is the battery internal potential, and h_p is the polarization coefficient. The effects of V_{dc} on the SOC for Lithium-Ion (LI-I), Nickel-Cadmium (N-C), and Lead-Acid (L-A) battery units are demonstrated in Fig. 5. The curves in Fig. 5 are obtained using the following data [20], [21]:

- Li-I: $V_{B0} = 25.59$ V, $h_p = 0.1484$, $(I_{DS})_{\text{Rated}} = 8$ A, $R_B = 0.050$ Ω .
- N-C: $V_{B0} = 25.70$ V, $h_p = 0.1406$, $(I_{DS})_{\text{Rated}} = 8$ A, $R_B = 0.073$ Ω .
- L-A: $V_{B0} = 25.93$ V, $h_p = 0.1373$, $(I_{DS})_{\text{Rated}} = 8$ A, $R_B = 0.104$ Ω .

It can be observed from Fig. 5 that regulating the terminal voltage of a battery unit will prevent the fast decay of the SOC. This observation is applicable to the three tested battery units.

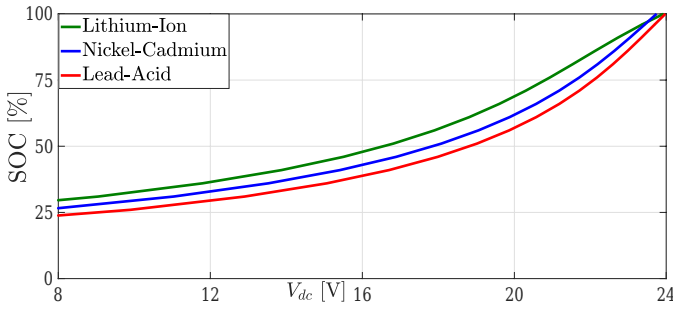


Fig. 5. Effects of changing V_{dc} (produced by the charger) on the SOC for the tested Lithium-Ion, Nickel-Cadmium, and Lead-Acid battery units.

The adjustment of the SOC will change the maximum short-circuit current that can be drawn from a battery unit. It should be noted that Fig. 5 does not provide any relationship between the SOC and battery open-circuit terminal voltage (VOC).

In order to demonstrate the effects of charger controller actions, two models for chargers were constructed. One model was for a 3ϕ , 0.25 kW, 60 Hz, thyristor-based charger, which had an ac side line voltage of 20 V. Another model was for a 3ϕ , 0.25 kW, 60 Hz, insulated-gate bipolar transistor (IGBT)-based charger, which had an ac side line voltage of 20 V [20], [21]. Each of the tested Lithium-Ion, Nickel-Cadmium, and Lead-Acid battery units was separately fed by the two chargers. Constant voltage and constant current controllers were designed, and employed to operate the thyristor and IGBT chargers. For each charger feeding each battery unit, a short-circuit was created at the terminals of the battery unit. For each short-circuit, $(I_{SCB})_{max}$ was measured, and plotted as shown in Fig. 6.

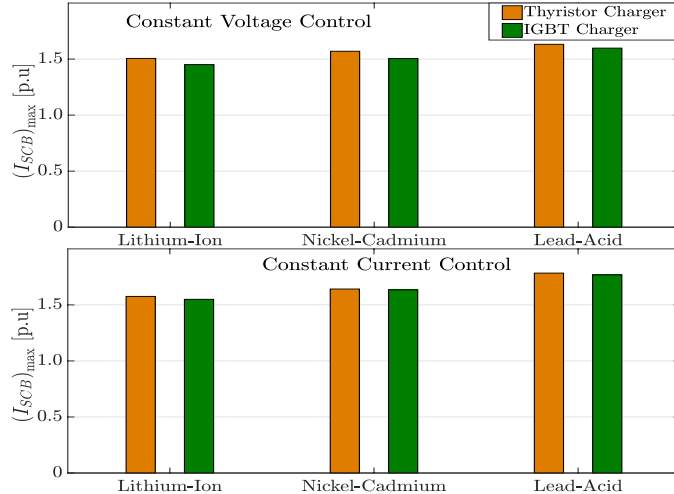


Fig. 6. Effects of charger controller actions on $(I_{SCB})_{max}$ for the tested Lithium-Ion, Nickel-Cadmium, and Lead-Acid battery units. The base value of I_{SCB} is 8 A. $k_{CV} = 0.84$, $k_{CC} = 0.63$, $\beta_1 = 0.92$, $\beta_2 = 0.24$.

It can be seen from Fig. 6 that both charger controllers managed to reduce $(I_{SCB})_{max}$ (relative to Fig. 4) for the three tested battery units. The reductions in $(I_{SCB})_{max}$ could also be observed for thyristor and IGBT chargers, when operated by constant voltage and constant current controllers. Observed reductions in $(I_{SCB})_{max}$ resulted from actions of the charger controller to adjust V_{dc} to its desired value during the short circuit at the dc bus. The adjustments in V_{dc} did allow the SOC to quickly change, thus limiting the discharge current during the short circuit at the dc bus.

IV. TESTING BATTERY CONTRIBUTIONS TO FAULT CURRENTS IN GRID-CONNECTED BSSs

The testing of battery contributions to fault currents was conducted for a 1 MW grid-connected BSS. This BSS was modeled using e-TAP, and its controller parameters were selected using MATLAB/SIMULINK tools. The tested BSS was operated for frequency regulation, which required a frequency droop controller as a second controller. The data for the tested grid-connected BSS is listed in Table I.

TABLE I
DATA FOR THE TEST 1 MW, 3ϕ , GRID-CONNECTED BSS

Parameter	Value
Rated DC Bus Voltage	960 V
Battery Type	Lead-Acid
Energy Capacity	240 kWh
Capacity	260 Ah
Maximum DoD	20%
Parallel Strings	30
R_B for Each String	6.26 Ω
Rated Current for Each String	34.5 A
Charger Type	Bi-Directional IGBT PEC
Charger Rated Current	770 A
Charger Pulsed Current	1600 A (over 1 ms)
Charger Controller	Constant Voltage: $k_{CV} = 0.78$
Frequency Droop Controller	$G_D = 0.3$, $DB = [49.9, 50.1]$ Hz
Rated AC Bus Voltage	960 V
Grid-Tie Filter	$L = 6.0$ mH
Grid-Connection Transformer	1.2 MVA, 11/0.96 kV, 60 Hz, $\Delta-Y$

G_D : the droop constant.

DB: the frequency dead-band.

DoD: Depth of discharge.

Fig. 7 shows a single line diagram for the test grid-connected BSS.

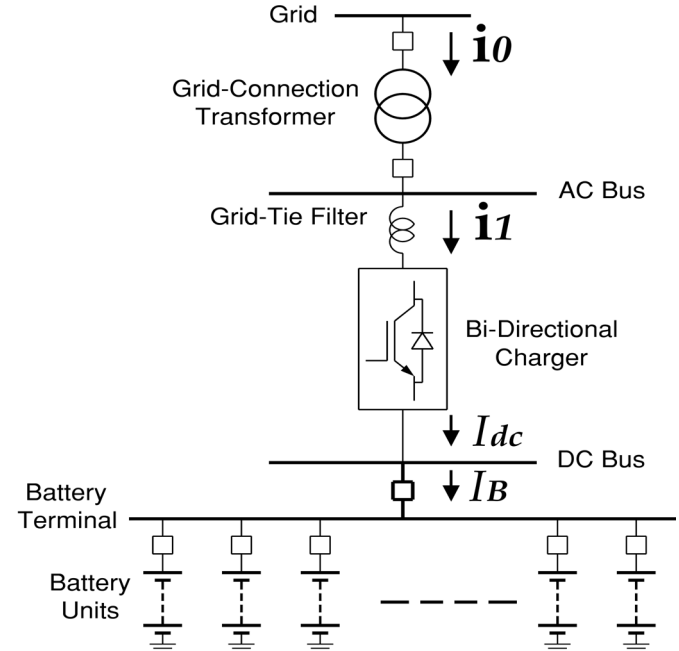


Fig. 7. A single line diagram for the test 1 MW grid-connected BSS.
 $i_0 = [i_{a0}, i_{b0}, i_{c0}]$ and $i_1 = [i_{a1}, i_{b1}, i_{c1}]$.

The e-TAP model for the test grid-connected BSS was tested for several fault events. The following fault events are presented and discussed in this paper:

- A) Charging and discharging operations of the BSS.
- B) Short circuit on the dc bus during the charging operation.

A. Charging and Discharging Operations of the BSS

This test aimed to investigate the normal operating modes of the test grid-connected BSS. The charging and discharging operations were tested through the load flow analysis. The charging operation was conducted with SOC set as SOC = 80%. It should be noted that SOC = 80% was selected as it represented the lowest acceptable SOC for the used Lead-Acid battery units. As a result, SOC = 80% provided the maximum charging current for the tested grid-connected BSS. The 3 ϕ currents i0, i1, dc currents I_{dc} , I_B , ac bus voltage, and dc bus voltage were collected for the charging operation as listed in Table II:

TABLE II
LOAD FLOW RESULTS FOR THE CHARGING OPERATION OF THE GRID-CONNECTED BSS

Quantity	Magnitude	Angle
i_{a0}	46.1 A	-2.86°
i_{b0}	46.1 A	-122.86°
i_{c0}	46.1 A	117.14°
i_{a1}	595.8 A	-3.03°
i_{b1}	595.8 A	-123.03°
i_{c1}	595.8 A	116.97°
I_{dc}	436.4 A	
I_B	436.4 A	
v_a	0.95 kV	-0.03°
v_b	0.95 kV	-120.03°
v_c	0.95 kV	119.97°
V_{dc}	0.96 kV	

The discharging operation was initialized for SOC = 96%, to ensure high discharging current. The grid-connected BSS injected power into the grid as:

$$P = 992 \text{ [kW]} \text{ and } Q = 86 \text{ [kVAR]}$$

Table III lists the 3 ϕ currents i0, i1, dc currents I_{dc} , I_B , ac bus voltage, and dc bus voltage obtained from the load flow analysis for the discharging operation of the grid-connected BSS: It should be noted that the currents in Table were taken

TABLE III
LOAD FLOW RESULTS FOR THE DISCHARGING OPERATION OF THE GRID-CONNECTED BSS

Quantity	Magnitude	Angle
i_{a0}	-52.9 A	-5.15°
i_{b0}	-52.9 A	-125.15°
i_{c0}	-52.9 A	114.85°
i_{a1}	-683.7 A	-4.62°
i_{b1}	-683.7 A	-124.62°
i_{c1}	-683.7 A	115.38°
I_{dc}	-500.8 A	
I_B	-500.8 A	
v_a	0.95 kV	-0.02°
v_b	0.95 kV	-120.02°
v_c	0.95 kV	119.98°
V_{dc}	0.96 kV	

with the convention that currents flowing from the grid had positive sign.

The results in Table II and Table III demonstrated stable charging and discharging operations of the tested grid-connected BSS. These results also showed that during steady-state conditions, I_{dc} and I_B had identical values. This feature was a result from the absence of any loads connected to the dc bus, and confirmed the power flow from and to the battery units. Finally, the data obtained from this test provided a base case for the steady-state operation of the grid-connected BSS.

B. Short Circuit on the DC Bus During the Charging Operation

The objective of this test was to examine the contribution of the battery units to a short circuit at the dc bus during the charging operation. The short circuit was created through a resistance of $R_F = 2 \Omega$, with SOC = 80%. The short circuit analysis tool of e-TAP was used to determine the currents through the grid-connected BSS. The 3 ϕ currents i0, i1, dc currents I_{dc} , I_B , ac bus voltage, and dc bus voltage were collected for the short circuit at the dc bus, and listed in Table IV. It should be noted that I_B had a negative sign to indicate its direction was out of the battery units.

TABLE IV
RESULTS FOR THE SHORT CIRCUIT AT THE DC BUS DURING CHARGING OPERATION WITH THE CONSTANT VOLTAGE CONTROLLER

Quantity	Magnitude	Angle
i_{a0}	16.73 A	-30.1°
i_{b0}	16.73 A	-150.1°
i_{c0}	16.73 A	89.9°
i_{a1}	216.09 A	-32.2°
i_{b1}	216.09 A	-152.3°
i_{c1}	216.09 A	87.8°
I_{dc}	198.27 A	
I_B	-282.94 A	
v_a	0.91 kV	-3.8°
v_b	0.91 kV	-123.8°
v_c	0.91 kV	116.2°
V_{dc}	0.92 kV	

For purposes of demonstrating the effects of the charger controller, the short circuit at the dc bus was created with constant voltage controller disabled. Table V lists the 3 ϕ currents i0, i1, dc currents I_{dc} , I_B , ac bus voltage, and dc bus voltage for the short circuit at the dc bus:

TABLE V
RESULTS FOR THE SHORT CIRCUIT AT THE DC BUS DURING CHARGING OPERATION WITHOUT THE CONSTANT VOLTAGE CONTROLLER

Quantity	Magnitude	Angle
i_{a0}	4.78 A	-11.9°
i_{b0}	4.78 A	-131.8°
i_{c0}	4.78 A	108.1°
i_{a1}	61.74 A	-13.2°
i_{b1}	61.74 A	-133.1°
i_{c1}	61.74 A	106.8°
I_{dc}	45.22 A	
I_B	-418.79 A	
v_a	0.92 kV	-0.04°
v_b	0.92 kV	-120.04°
v_c	0.92 kV	119.96°
V_{dc}	0.83 kV	

The results of this test demonstrated the effects of the charger controller on battery contributions to the short circuit current. The data in Table IV and Table V showed that actions of the constant voltage controller supported V_{dc} by increasing I_{dc} . These actions resulted in limiting I_B flowing to the short circuit branch. The changes in I_{dc} , I_B , and V_{dc} could be seen from the values of these quantities in Table IV and Table V.

In order to demonstrate the effects of charger controller and SOC on I_B , the short circuit at the dc bus was created for several values of SOC with and without the actions of the constant voltage controller. Fig. 8 shows I_B due to the short circuit at the dc bus, for several values of SOC with and without the charger controller. The results in Fig. 8 showed effects of the charger controller and SOC on the contribution of battery

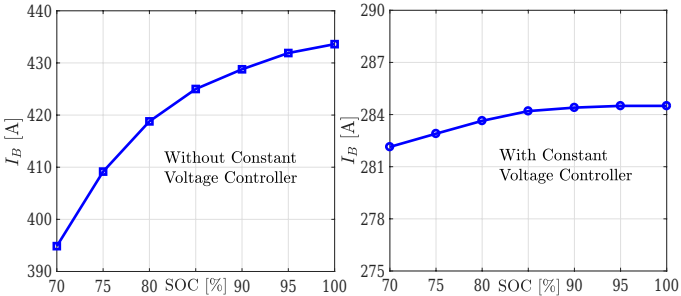


Fig. 8. The contribution of the battery units to the short circuit current, I_B , at the dc bus for different values of SOC, with and without the actions of the constant voltage controller.

units to the short circuit current. Actions of the constant voltage controller regulated V_{dc} , and limited I_B triggered by the short circuit at the dc bus.

The tested cases have demonstrated the effects of the state-of-charge (SOC) and actions of the charger controller on the contributions of battery units to faults in grid-connected BSSs. In all tested cases, low SOC values have resulted in lower currents drawn from battery units due to fault events. Furthermore, actions of charger controller have been found able to limit the reductions in dc voltage at battery terminals. These controller actions have resulted in limiting the contributions of battery units to fault currents. These effects of the SOC and charger controller have been observed for faults in different locations of the grid-connected BSS. Finally, the effects of the SOC and charger controller on battery contributions to fault currents have been observed during the charging and discharging operation. Table VI provides a summary of I_B and V_{dc} for different fault events at different locations of a grid-connected BSS. These values are determined at SOC = 100%, with and without controller actions (constant voltage), and using IEEE Standard 1375 and IEEE Standard 946.

TABLE VI

BATTERY CURRENT AND TERMINAL VOLTAGE DURING FAULTS IN DIFFERENT LOCATIONS IN A GRID-CONNECTED BSS

Fault	With Controller	Without Controller	IEEE Standards
Short-Circuit at DC Bus	$I_B = 286.5 \text{ A}$ $V_{dc} = 0.93 \text{ kV}$	$I_B = 433.6 \text{ A}$ $V_{dc} = 0.78 \text{ kV}$	$I_B = 4064.9 \text{ A}$ $V_{dc} = 0.96 \text{ kV}$
3 ϕ Fault at AC Bus	$I_B = 329.7 \text{ A}$ $V_{dc} = 0.94 \text{ kV}$	$I_B = 731.3 \text{ A}$ $V_{dc} = 0.72 \text{ kV}$	$I_B = 7700 \text{ A}$ $V_{dc} = 0.96 \text{ kV}$
Line-to-Ground at AC Bus	$I_B = 466.8 \text{ A}$ $V_{dc} = 0.94 \text{ kV}$	$I_B = 882.4 \text{ A}$ $V_{dc} = 0.77 \text{ kV}$	$I_B = 7700 \text{ A}$ $V_{dc} = 0.96 \text{ kV}$
Line-to-Line at AC Bus	$I_B = 394.6 \text{ A}$ $V_{dc} = 0.93 \text{ kV}$	$I_B = 782.2 \text{ A}$ $V_{dc} = 0.80 \text{ kV}$	$I_B = 7700 \text{ A}$ $V_{dc} = 0.96 \text{ kV}$

The data in Table VI shows the effects of the charger controller on battery currents and terminal voltage due to faults in different locations of a grid-connected BSS. The data in Table VI confirms the effects of the SOC and charger controller on I_B and V_{dc} for fault conditions. Observed effects of the SOC and charger controller on I_B and V_{dc} can be used for developing accurate and reliable detection of faults in grid connected BSSs.

V. CONCLUSIONS

This paper has presented the factors that affect battery contributions to fault currents in grid-connected battery storage systems (BSSs). The typical determination of battery contributions to fault currents is based on IEEE standards 1375 and 946, which use the rated battery terminal voltage and internal

resistance. These standards are widely used to select and size protective devices for battery units used in stationary BSSs (see Fig. 2). Grid-connected BSSs do not have loads connected to the dc bus, thus battery currents only flow through the charger PEC. Battery currents are directly related to the state-of-charge (SOC) and actions of the charger controller. Effects of the SOC and charger controller on the currents drawn from battery units due to faults have been investigated for the charging and discharging operations. Investigation results have shown that the currents drawn from battery units, due to faults, are directly related to the SOC and actions of charger controller. Observed effects can be critical for developing fault detection methods to improve the protection and operation of grid-connected BSSs.

REFERENCES

- [1] *IEEE Application Guide for IEEE Standard for Interconnecting Distributed Resources With Electric Power Systems*, IEEE Std. 1547.2-2008, 2008.
- [2] *IEEE Recommended Practice for the Design of DC Power Systems for Stationary Applications*, IEEE Std. 946-2020, 2020.
- [3] *IEEE Recommended Practice for Sizing Lead-Acid Batteries for Stand Alone Photovoltaic (PV) Systems*, IEEE Std. 1013-2007, 2007.
- [4] *IEEE Guide for the Protection of Stationary Battery Systems*, IEEE Std. 1375-1998, 1998.
- [5] *IEEE Recommended Practice for Industrial and Commercial Power Systems Analysis*, IEEE Std. 399-1997, 1997.
- [6] S. A. Saleh, E. Ozkop, C. Mardegan, and M. Valdes, "Bus Differential Protection for Buses Interconnecting Battery Storage Systems," *In Proc. of the 57th IEEE IAS Industrial and Commercial Power Systems Technical Conference (I&CPS)*, Las Vegas, NV, pp. 1-8, May 2021.
- [7] G. Wang, G. Konstantinou, C. D. Townsend, J. Pou, S. Vazquez, G. D. Demetriades, and V. G. Agelidis, "A Review of Power Electronics for Grid Connection of Utility-Scale Battery Energy Storage Systems," *IEEE Transactions on Sustainable Energy*, Vol. 7, No. 4, pp. 1778-1790, 2016.
- [8] M. Farhadi and O. Mohammed, "Energy Storage Technologies for High-Power Applications," *IEEE Trans. on Industry Applications*, Vol. 52, No. 3, pp. 1953-1961, 2016.
- [9] M. A. Haj-ahmed and M. S. Illindala, "Investigation of Protection Schemes for Flexible Distribution of Energy and Storage Resources in an Industrial Microgrid," *IEEE Trans. on Industry Applications*, Vol. 51, No. 3, pp. 2071-2080, 2015.
- [10] P. Rakhra, P. J. Norman, S. D. A. Fletcher, S. J. Galloway, and G. M. Burt, "Evaluation of the Impact of High-Bandwidth Energy-Storage Systems on DC Protection," *IEEE Trans. on Power Delivery*, Vol. 31, No. 2, pp. 586-595, 2016.
- [11] S. A. Saleh, C. Richard, X. F. St-Onge, J. Meng, and E. Castillo-Guerra, "Comparing the Performance of Protection Coordination and Digital Modular Protection for Grid-Connected Battery Storage Systems," *IEEE Trans. on Industry Applications*, Vol. 55, No. 3, pp. 2440-2454, 2019.
- [12] S. A. Saleh, R. McSheffery, and R. Meng, "Testing the Performance of the Digital Modular Protection for Grid-Connected Battery Storage Systems," *IEEE Trans. on Industry Applications*, Vol. 54, No. 3, pp. 2059-2070, 2018.
- [13] A. C. Gaunce, X. Wu, J. D. Mandeville, D. J. Hoffman, A. S. Khalsa, J. Sottile, and R. J. Wellman, "DC Arc Flash: Testing and Modeling Incidents in a 125-V Substation Battery Backup System," *IEEE Trans. on Industry Applications*, Vol. 56, No. 3, pp. 2138-2147, 2020.
- [14] R. Hedding and P. Hayes, "Protection of Battery Energy Storage System," *In Proc. of the 64th IEEE Annual Conference for Protective Relay Engineers*, College Station, TX, pp. 155-159, April 2011.
- [15] L. Tao, G. Chunlin, Y. Jingjing, W. Jianing, Z. Chenliang, and M. Huiyuan, "Analysis on DC Side Protection Strategy for Grounded Power Battery Energy Storage System," *In Proc. of the 2020 IEEE IAS Industrial and Commercial Power System Asia Technical Conference*, Weihai, China, pp. 1006-1011, July 2020.
- [16] S. A. Saleh, A. S. Aljankawey, B. Alsayid, and M. S. Abu-Khaizaran, "Influences of Power Electronic Converters on Voltage-Current Behaviors During Faults in DGUs-Part II: Photovoltaic Systems," *IEEE Trans. on Industry Applications*, Vol. 51, No. 4, pp. 2832-2845, 2015.
- [17] W. Hartmann, R. Fleck, R. Graba and M. Hergt, "Characterization of Commercial IGBT Modules for Pulsed Power Applications," *In Proc. of the 13th IEEE Pulsed Power Conference (PPC)*, San Francisco, CA, pp. 1-4, October 2013.

- [18] *IEEE Recommended Practice for Conducting Short-Circuit Studies and Analysis of Industrial and Commercial Power Systems, IEEE Std. 3002.3-2018*, 2018.
- [19] M. Coleman, C. K. Lee, C. Zhu, and W. G. Hurley, "State-of-Charge Determination from EMF Voltage Estimation: Using Impedance, Terminal Voltage, and Current for Lead-Acid and Lithium-Ion Batteries," *IEEE Trans. on Industrial Electronics*, Vol. 54, No. 5, pp. 2550–2557, 2007.
- [20] *Power System Toolbox User Guide*. Natick, MA: Math Works, 2017.
- [21] *e-TAP 19.01: Short Circuit Analysis Toolbox*. Irvine, CA, e-TAP, 2019.
- [22] D. Sha, G. Xu, and Y. Xu, "Utility Direct Interfaced Charger/Discharger Employing Unified Voltage Balance Control for Cascaded H-Bridge Units and Decentralized Control for CF-DAB Modules," *IEEE Trans. on Industrial Electronics*, Vol. 64, No. 10, pp. 7831–7841, 2017.
- [23] R. Metidji, B. Metidji, and B. Mendil, "Design and Implementation of a Unity Power Factor Fuzzy Battery Charger using an Ultrasparse Matrix Rectifier," *IEEE Trans. on Power Electronics*, Vol. 28, No. 5, pp. 2269–2276, 2013.
- [24] L. Y. Wang, M. P. Polis, G. G. Yin, W. Chen, Y. Fu, and C. C. Mi, "Battery Cell Identification and SOC Estimation Using String Terminal Voltage Measurements," *IEEE Trans. on Vehicular Technology*, Vol. 61, No. 7, pp. 2925–2935, 2012.

Modeling and Fault Characteristic Analysis of Grid-forming Electrochemical Energy Storage

Yuanhang Xu
School of Electrical Engineering
Beijing Jiaotong University
Beijing, China
23121499@bjtu.edu.cn

Jinghan He
School of Electrical Engineering
Beijing Jiaotong University
Beijing, China
juhe@bjtu.edu.cn

Meng Li
School of Electrical Engineering
Beijing Jiaotong University
Beijing, China
lmeng@bjtu.edu.cn

Xiaotong Du
School of Electrical Engineering
Beijing Jiaotong University
Beijing, China
22110453@bjtu.edu.cn

Xiang Chen
School of Electrical Engineering
Beijing Jiaotong University
Beijing, China
22121435@bjtu.edu.cn

Guohong WU
Dept. of Electrical & Electronics Eng.
Tohoku Gakuin University
Miyagi, Japan
wugh@mail.tohoku-gakuin.ac.jp

Abstract—With the extensive application of energy storage technology, electrochemical energy storage has become a hot solution for addressing the challenges of integrating new energy sources into the grid. However, the switching between charging and discharging modes and the differences in control strategies can all impact the fault characteristics of energy storage systems. Therefore, it is necessary to conduct a comprehensive and in-depth analysis of their fault characteristics. This paper establishes a grid-forming energy storage power station system model based on the system topology and control strategies of energy storage power stations. It simulates the differences in characteristics under normal operation and fault ride-through scenarios in both charging and discharging modes, and analyzes the reasons for these differences. Finally, a grid-forming energy storage power station simulation model is built on PSCAD, providing a reference for subsequent research on the protection and control strategies of grid-forming energy storage grid-connected systems.

Keywords—*Electrochemical energy storage, grid-forming control, fault characteristic analysis, fault ride-through.*

I. INTRODUCTION

Currently, environmental issues are intensifying, and the world is focusing on two key topics: "carbon peak" and "carbon neutrality". In the power industry, generating electricity from renewable energy sources such as wind and solar energy is one of the effective ways to address this challenge. However, renewable energy sources like wind power and photovoltaic have significant differences from traditional energy sources in terms of power generation principles and control methods. As their proportion in the power system increases, the stability, operation, and planning of the system face significant changes. The main challenge lies in dealing with the intermittency of renewable energy and the uncertainty brought by the electrification of power [1]. In the context of a smart grid, energy

storage technology is crucial for the integration and utilization of large-scale new energy. Energy storage technology is the core of achieving flexible conversion and comprehensive utilization of electrical energy with other forms of energy, solving the problem of mismatch between energy production and consumption in terms of time and space, and enhancing the mobility and shareability of energy [2-4], among which electrochemical energy storage technology is relatively mature. The use of power electronic devices in energy storage systems and the four-quadrant operation characteristics of energy storage increase the complexity of system faults. Among them, the ways of inverter-type energy storage access are divided into grid-following and grid-forming, compared with grid-following control (GFLC), grid-forming control (GFMC) technology can make better use of the flexibility and controllability of voltage source converters (VSC). This technology shows excellent adaptability and stability in weak power grids, capable of quickly autonomously constructing system voltage, and supplementing the system's missing inherent inertia and damping characteristics, providing stable voltage and frequency support for the power grid [5]. Therefore, it is very necessary to establish a grid-forming energy storage power station model suitable for fault analysis and to study its fault characteristics under different conditions.

Currently, scholars have conducted extensive research on the construction of simulation models and the study of fault characteristics of electrochemical energy storage power stations. Reference [6] discusses the electromagnetic transient behavior of lithium-ion batteries under AC grid faults and analyzes the impact of the battery's state of charge (SOC) and converter control strategy on fault current characteristics. References [7-8] have constructed multi-timescale energy storage models to explore the electromechanical transient and medium to long-term dynamic characteristics of battery energy storage systems. Reference [9] has developed an energy storage model suitable for electromechanical transient analysis using virtual

This work is supported by National Natural Science Foundation of China (Grant No.U23B6007, Fundamental Theory and Methods for Form Evolution and High Efficient Safe Operation of New Power Distribution Systems).

synchronous machine technology. References [10-11] have built an electromechanical transient model of an energy storage system considering the charging and discharging power of batteries in the PSASP simulation environment, and the models uniformly adopt frequency-active power control and voltage-reactive power control strategies. Reference [12] discusses the dynamic behavior of energy storage power stations under grid faults and points out that the differences in characteristics exhibited by energy storage power stations in charging and discharging states are a key factor that needs to be considered in relay protection. Reference [13] proposes an electromagnetic transient modeling method for lithium battery energy storage systems and analyzes the differences in fault characteristics of energy storage power stations under different charging and discharging modes. Existing literature mostly focuses on modeling energy storage power stations in grid-following mode, and models with grid-forming control are mostly concentrated on new energy sources such as photovoltaics. Moreover, there is more analysis on fault characteristics under discharging states. Therefore, existing research is insufficient to reflect the fault characteristics of grid-forming energy storage systems. To analyze the fault characteristics of grid-forming energy storage systems, this paper takes lithium-ion battery energy storage as the research subject and establishes an electromagnetic transient model of the energy storage system for both normal operation and fault operation conditions. Furthermore, it compares and analyzes the operational differences of energy storage in charging and discharging modes.

II. ENERGY STORAGE POWER STATION TOPOLOGY

A. Energy Storage Power Station

The grid-connected electrochemical energy storage system adopts a dual-stage topology as shown in Fig.1, which has a wider operating voltage range compared to a single-stage type. The grid-connected system consists of lithium-ion energy storage, a bidirectional DC/DC converter(BDC), an energy storage power converter system(PCS), and an LC filter. The lithium battery is boosted by the BDC, then connected to the AC grid after being inverted by the PCS and filtered by the filter. The BDC is used to maintain the stability of the DC-side voltage and to meet the power transmission requirements in both charging and discharging modes. The PCS employs virtual synchronous control to independently control the AC-side voltage, frequency, active power, and reactive power, possessing strong frequency and voltage support capabilities. In the figure, E_{bat} and R_{bat} represent the internal electromotive force and internal resistance of the lithium battery energy storage, C_1 and C_2 are the capacitors on the low-voltage side and high-voltage side of the DC/DC converter, respectively, U_{dc} is the DC bus voltage, and L_N and C_N are the inductor and capacitor of the LC filter.

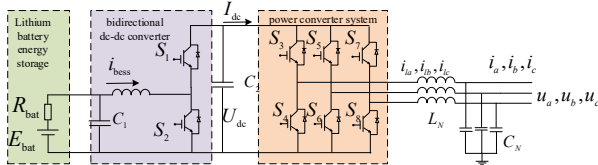


Fig. 1. Energy Storage Power Station Grid-connection System

B. Battery Model

In previous literature, various equivalent circuit models have been proposed. These include the RC model, Thevenin equivalent circuit model, PNGV model, Peuker model, and Shepherd model, among others. Among them, the Shepherd model has a relatively simple structure and is easy to implement and simulate on a computer. By adjusting the parameters in the model, it is possible to simulate different types of batteries and different operating conditions, and it can describe the dynamic response of batteries during the charging and discharging process, including transient and steady-state behavior.

The equivalent circuit model of the battery is shown in reference[14] which is represented as a controlled source in series with a resistor. The expression for the internal electromotive force is given by:

$$E_{bat} = E_0 - K \frac{Q}{Q-it} + A \cdot e^{-B \cdot it} \quad (1)$$

In the formula, E_{bat} represents the internal electromotive force, E_0 is the constant voltage of the battery; K is the polarization voltage; Q is the battery capacity; A is the amplitude of the exponential region; B is the inverse of the time constant in the exponential region; it is the electrical charge that the battery has absorbed/released. The parameters of the model are all calculated from the discharge characteristic curve of the battery, and the specific discharge characteristic curve can be found in reference [14].

The battery voltage equation can be modified as follows to replace it with the ratio of the remaining capacity to the total capacity, SOC, to represent:

$$E_{bat} = E_0 - K \frac{1}{SOC} + A \cdot e^{-B \cdot Q(1-SOC)} \quad (2)$$

III. GRID-CONNECTION SYSTEM CONTROL STRATEGY

A. BDC Control Strategy

The DC/DC converter is connected to the battery energy storage on one side and the DC side of the PCS on the other, and is used to maintain a constant DC bus voltage. The specific control strategy is shown in Fig.2. The control method adopts a dual-loop control, the specific control method is as follows: by setting a reference value for the outer loop DC voltage, a reference value for the inner loop current is given based on the difference, and the difference between the current reference value and the actual value is passed through a proportional-integral controller to obtain the duty cycle of the thyristors S1 and S2, ultimately obtaining the triggering signal.

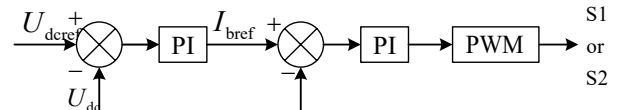


Fig. 2. Control Strategy for Constant DC Bus Voltage

B. PCS Control Strategy

As shown in Fig.1 and Fig.3, the four-quadrant operation function of the energy storage system is realized by controlling

the conduction and interruption of the switching tubes. The PCS adopts grid-forming control, with the specific control method being virtual synchronous machine control.

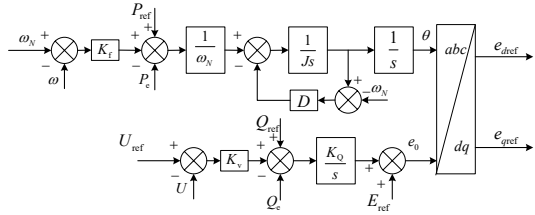


Fig. 3. Virtual Synchronous Machine Control

The control method during the normal operation mode of the energy storage system is as follows: the outer loop consists of a virtual synchronous control loop, which includes two parts: active power-frequency control loop and reactive power-voltage control loop. In Fig.3., P_{ref} and P_e represent the reference and actual values of active power, respectively; Q_{ref} and Q_e represent the reference and actual values of reactive power, respectively. J , D , K_f , K_v , K_Q , ω , and ω_N represent virtual inertia, virtual damping, active power frequency control coefficient, reactive power voltage control coefficient, reactive power voltage integral coefficient, virtual internal electromotive force angular frequency, and rated angular frequency, respectively. U_{ref} is the base voltage value, while E_{ref} is the static working point electromotive force. During normal operation, U_{ref} equals U_N . The active power-frequency control loop simulates the motion equation of the generator rotor [15], providing damping and inertia support to the power grid, and outputs the virtual internal electromotive force phase angle θ . The reactive power-voltage control loop simulates the excitation of the synchronous machine to simulate the reactive power-voltage regulation characteristics, outputting the virtual internal electromotive force amplitude e_0 . The basic control equations for both are as follows:

$$\begin{cases} J \frac{d^2\theta}{dt^2} = \frac{P_{\text{ref}} - P_e}{\omega_0} - D(\omega - \omega_0) \\ e_0 = \frac{K_Q}{S}(K_v(U_{\text{ref}} - U) + Q_{\text{ref}} - Q) + E_{\text{ref}} \end{cases} \quad (3)$$

As shown in Fig.4, the intermediate link is a virtual impedance loop. By simulating the internal impedance characteristics of the synchronous generator, it effectively enhances the operational stability of virtual synchronous control.

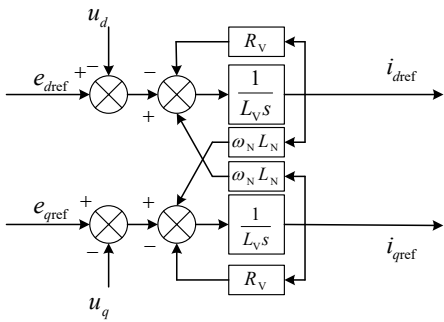


Fig. 4. Virtual Impedance Link

The basic control equation is as follows:

$$\begin{cases} e_{d\text{ref}} - u_d = L_V \frac{di_{d\text{ref}}}{dt} + R_V i_{d\text{ref}} - \omega_N L_N i_{q\text{ref}} \\ e_{q\text{ref}} - u_q = L_V \frac{di_{q\text{ref}}}{dt} + R_V i_{q\text{ref}} + \omega_N L_N i_{d\text{ref}} \end{cases} \quad (4)$$

In the formula, in the virtual synchronous control link, the virtual impedance control link includes L_N , L_V and R_V as the actual inductance, virtual resistance, and inductance values, respectively. $e_{d\text{ref}}$ and u_{dq} are the d-axis and q-axis component values of the virtual internal electromotive force and the grid connection point voltage, respectively.

The final link is the inner current loop, which is similar to the current control link in traditional grid-following control. The control still uses PI control to achieve current tracking, and the basic control equation is as follows:

$$\begin{cases} V_d = K_p(i_{d\text{ref}} - i_{d\text{d}}) + K_i \int (i_{d\text{ref}} - i_{d\text{d}}) dt - \omega_N L_c i_{q\text{ref}} + u_d \\ V_q = K_p(i_{q\text{ref}} - i_{q\text{d}}) + K_i \int (i_{q\text{ref}} - i_{q\text{d}}) dt + \omega_N L_c i_{d\text{ref}} + u_q \end{cases} \quad (5)$$

In the formula, V_{dq} represents the reference value of the converter's dq-axis voltage, $i_{dq\text{ref}}$ and $i_{dq\text{d}}$ represent the reference and actual values of the converter's dq-axis current, respectively, and K_p and K_i are the proportional and integral coefficients of the PI control loop.

C. Fault Ride-Through Control

When an external short circuit fault occurs, the topology of the external network changes accordingly, which may cause a certain fluctuation in the grid connection point voltage. Therefore, it is necessary to change the control strategy under the normal operation model to prevent excessive fault current from damaging the equipment, and to continue operating without disconnecting from the grid after the fault occurs. Thus, a fault ride-through control strategy is introduced during the fault period. The conventional fault ride-through control strategy is similar to the traditional grid-following fault ride-through control strategy, which abandons the outer loop control after the fault and directly controls the current loop. However, in order to maintain the high inertia characteristics of the virtual synchronous machine, this paper uses a fault ride-through control strategy that does not change the original control characteristics. Only the voltage reference value of the reactive power loop is changed to track the actual value of the grid connection point voltage. The active power and reactive power are given by the following formulas:

$$Q_{\text{ref}} = \begin{cases} 0, U > 0.8U_N \\ 1.5(0.8 - \frac{U}{U_N})I_N U, \quad U \in [0, 0.8U_N] \end{cases} \quad (6)$$

In the formula, U_N represents the rated voltage, and I_N represents the rated current.

Based on the reactive power reference value, the formula for the active power reference value can be derived as follows:

$$P_{\text{ref}} = \begin{cases} P_{\text{ref0}}, U > 0.8U_N \\ |U|I_{\text{p-ref}} = |U|\sqrt{I_N^2 - \left(1.5\left(0.8 - \frac{U}{U_N}\right)I_N\right)^2}, \\ U \in [0, 0.8U_N] \end{cases}, \quad (7)$$

In the formula, P_{ref0} represents the initial power reference value, and $I_{\text{p-ref}}$ represents the active current value.

When an unbalanced fault occurs during power grid operation, it causes the generation of negative sequence currents, increasing the degree of grid imbalance. To ensure the safety and stability of the power system, a negative sequence control strategy is introduced to reduce the impact of negative sequence currents. This control strategy is mainly implemented through the inner current loop, where the negative sequence current is directly given a reference value of 0 through the inner loop, thereby effectively suppressing the negative sequence current. The positive sequence components continue to maintain their original control strategy.

IV. MODEL VERIFICATION AND FAULT ANALYSIS

To verify the effectiveness of the constructed energy storage power station model and its control strategy, and to further analyze the complex fault characteristics of the energy storage power station, an energy storage grid-connected system is built on the PSCAD/EMTDC simulation platform. A configuration of 20 battery energy storage systems with a capacity of 0.5MWh each is used, connected through a 380V/10kV transformer and then through a 2km transmission line for grid connection. Model validity and fault analysis are conducted under different scenarios.

A. Normal Operation Mode

First, set the energy storage to discharge mode with an initial capacity of 50%. The discharge power is set to 0.015MW. At 1.9 seconds, switch the discharge mode to charge mode. The power transition and phase change curves are shown in Fig.5 and Fig.6, respectively.

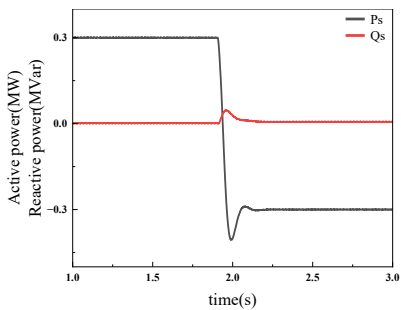


Fig. 5. Power Change Curve for Normal Mode Charge-Discharge Transition

It can be seen that after the mode switch command is initiated, the power can quickly track the specified value and stabilize around -0.015MW. As shown in Fig.6, the phase difference between voltage and current changes from 0° to approximately 180° . The experimental results indicate that the model can quickly respond to the transition between charge and discharge modes.

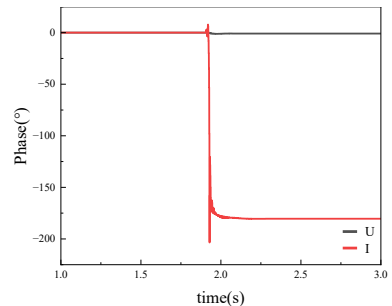
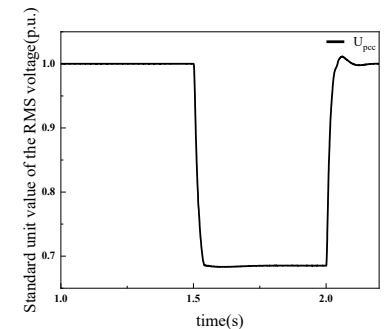


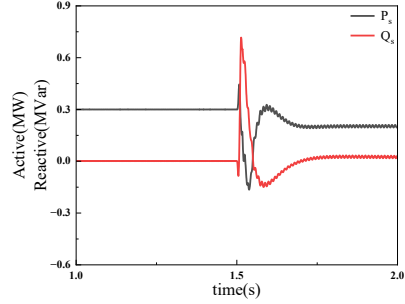
Fig. 6. Voltage and Current Phase Relationship During Normal Mode Charge-Discharge Transition

B. Fault Ride-Through Capability

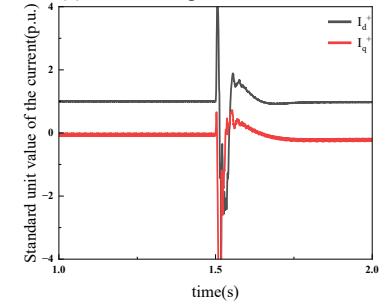
For the energy storage system in discharge mode, a single-phase grounding fault is set at the end of the outgoing line, and the fault is initiated at 1.5 seconds. As shown in Fig.7, the figures depict the effective value of the grid connection point voltage, fault power, dq-axis positive and negative sequence currents, and the AC-side current waveform.



(a)Effective Value of Grid Connection Point Voltage



(b)Power Change Waveform



(c)Positive Sequence dq-Axis Current

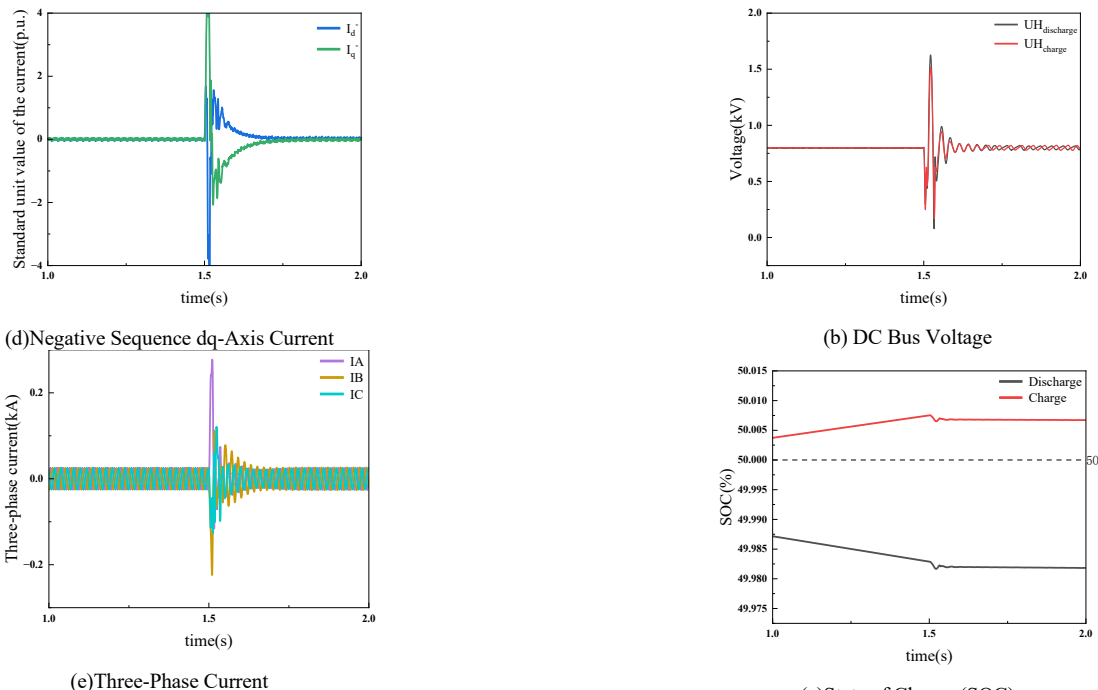


Fig. 7. Unsymmetrical Fault Simulation Results

As shown in Fig.7(a), after the fault occurs, the grid connection point voltage drops to around 0.69 p.u. As shown in Fig.7(b) and 7(c), to support the voltage and prevent overcurrent, the fault control strategy changes the reference value of the power loop, and the positive sequence current changes in response to the reference value of the power loop, with a similar trend. Due to the implementation of a negative sequence current suppression strategy, the negative sequence current component is suppressed to zero, as shown in Fig.7(d). Due to changes in the working state and the PCS control strategy, the reference values of the d and q-axis currents change abruptly, causing the output current amplitude and phase to change abruptly. The amplitude of the fault steady-state current is about 1.05 times the rated current, as shown in Fig.7(e).

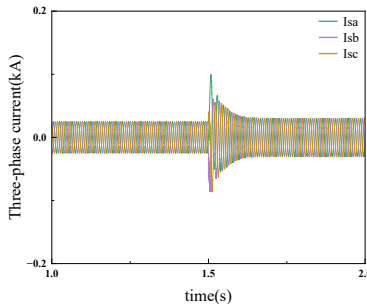
C. Differences in Fault Characteristics between Charging and Discharging Scenarios

To analyze the impact of charging and discharging modes on fault characteristics, the energy storage power station is set to operate in charging and discharging modes at the start of the simulation, with a three-phase non-metallic short circuit fault set at the end of the outgoing line, and the fault is initiated at 1.5 seconds. The simulation results are shown in Fig.8.



(a) Charging and Discharging Active Power

(f) Three-Phase Current during Deep Voltage Sag in Discharging Mode



(g)Three-Phase Current during Shallow Voltage Dip in Discharging Mode

Fig. 8. Charging/Discharging Fault Simulation Results

As shown in Fig.8(a), it can be seen that under normal charging and discharging modes, when the voltage drops, the power reference value changes, and it is lower than the reference value under normal operation mode. However, due to the constant voltage control of the BDC, the power absorbed/released by the energy storage is consistent with the power transmitted by the PCS, as shown in Fig.8(b), the DC bus voltage can still be maintained at around 0.8kV after the fault. But the rate of change of SOC is slowed down, as shown in Fig.8(c). As shown in Fig.8(d) and 8(e), The phase difference between voltage and current exists after the fault due to the different directions of active power transmission in charging/discharging modes. Therefore, when conducting related research in relay protection, it is necessary to consider the impact of the phase difference caused by charging/discharging modes on the protection strategy.

The magnitude of the fault current is related to the degree of voltage drop at the grid connection point, and since the power reference value is proportional to the grid connection point voltage. When the degree of voltage drop at the grid connection point is large, the fault current after the fault is less than the rated current, as shown in Fig.8(f), which may cause the protection to fail to act. When the grounding resistance is changed to 1Ω and the degree of voltage drop at the grid connection point is lower, the fault current is greater than the rated current, about 1.2 times the rated current, as shown in Fig.8(g), and the protection setting value can be set according to the current magnitude.

V. CONCLUSION

This paper, based on the structure and control strategy of the electrochemical energy storage power station, has established a simulation model of the energy storage power station. It focuses on analyzing the fault characteristics of the energy storage power station under charging/discharging scenarios and considers the impact of the degree of voltage dip. The main conclusions are as follows:

- 1) The proposed model can respond to power command changes in a timely manner, quickly switch between charging and discharging states, and achieve stable regulation of transmitted power; it has fault ride-through capabilities and can reflect the fault characteristics of the energy storage power station under charging/discharging scenarios.

- 2) Under charging/discharging scenarios, when a grid-side fault causes a deep voltage dip at the grid connection point of the energy storage power station, the steady-state fault current is less than the rated working current; when the dip is shallow, the fault current is generally greater than the rated working current; the particularity of this fault characteristic may have a certain impact on existing current protection schemes or settings.

- 3) In charging/discharging scenarios, after a fault occurs on the grid side, the energy storage power station can still achieve stable DC bus voltage and balance the power transmission on both sides of the PCS through constant voltage control of the BDC.

REFERENCES

- [1] KANG C, YAO L. Key scientific issues and theoretical research framework for power systems with high proportion of renewable energy [J]. Automation of Electric Power Systems, 2017, 41(9): 1-11.
- [2] Zhou L, Huang Y, Guo K, et al. A Review of Energy Storage Technology in Microgrids. Electric Power Systems Research, 2011, 39(7): 147-152.
- [3] Yuan, X., Cheng, S., Wen, J. Prospects of energy storage technology in addressing the challenges of large-scale wind power integration. Automation of Electric Power Systems, 2013, 37(1): 14-18.
- [4] Luo, X., Wang, J., Ma, Z. A review of energy storage technologies and their application prospects in smart grids. Smart Grid, 2014, 2(1): 7-12.
- [5] Wang, L., Hu, P., Yu, Y., et al. Transient stability analysis of grid-forming converters under asymmetrical faults based on hybrid synchronous control. Automation of Electric Power Systems, 1-15 [2024-09-10].
- [6] SALEH SA, OZKOP E, VALDES M E, et al. On the factors affecting battery unit contributions to fault currents in grid-connected battery storage systems[J]. IEEE Transactions on Industry Applications, 2022, 58(3): 3019-3028.
- [7] Lu, Q., Hu, W., Zheng, L., et al. Multi-timescale modeling and analysis application of battery energy storage systems. Proceedings of the CSEE, 2013, 33(16): 86-93, 14.
- [8] Ye, X., Liu, T., Wu, G., et al. Research on multi-timescale simulation modeling of battery energy storage systems and analysis of large-scale grid-connected characteristics. Proceedings of the CSEE, 2015, 35(11): 2635-2644.
- [9] He, P., Li, Z., Li, C., et al. Modeling of electromechanical transient characteristics of energy storage based on virtual synchronous machine technology. Electric Power System Protection and Control, 2022, 50(7): 11-22.
- [10] Li, J., Niu, M., Zhang, B., et al. Electromechanical Transient Simulation Model of Battery Energy Storage System. Transactions of China Electrotechnical Society, 2018, 33(8): 1911-1918.
- [11] Li, Y., Jing, P., Wang, L., et al. Research on the Mathematical Model of Universal Energy Storage System and Its PSASP Modeling. Power System Technology, 2012, 36(1): 51-57.
- [12] BERGER M, KOCAR I, FARANTATOS E, et al. Modeling of Li-ion battery energy storage systems (BESSs) for grid fault analysis[J]. Electric Power Systems Research, 2021, 196: 107160.
- [13] Zhang, J., Liu, P., Xie, X., et al. Electromagnetic Transient Modeling Method of Lithium-ion Battery Energy Storage for Fault Characteristic Analysis. Automation of Electric Power Systems, 2023, 47(7): 166-173.
- [14] Qi, L., Wang, X., Zhu, Y., et al. Modeling of Energy Storage Battery and PSCAD Simulation. Electrical Applications, 2014, 33(11): 85-89.
- [15] Jia L, Miura Y, Ise T. Comparison of Dynamic Characteristics Between Virtual Synchronous Generator and Droop Control in Inverter-Based Distributed Generators[J]. IEEE Transactions on Power Electronics, 2015,31(5):3600-3611.

Modeling and Fault Characteristics Analysis of Multi-Energy Complementary Microgrids

Chunyan Li

School of Electrical and Electronic Engineering,
Chongqing University of Technology, Chongqing,
China

lichunyan59@cqut.edu.cn

Huimin Huang

School of Electrical and Electronic Engineering,
Chongqing University of Technology, Chongqing,
China

2602146451@qq.com

Yan Chen

School of Electrical and Electronic Engineering,
Chongqing University of Technology, Chongqing,
China

Chenyan2012@cqut.edu.cn

Wenyan Li

Chongqing Communication Design Institute Co., Ltd,
Chongqing, China
liwy1.cq@chinaccs.cn

Abstract—To promote the achievement of the 'dual carbon' goals and address the threats posed by the uncertainties of new energy sources to grid operation, it is urgent to study the operational characteristics of multi-energy microgrids that include wind, solar, and storage systems. The doubly-fed induction generator (DFIG) is the mainstream model for wind energy utilization due to its wider speed regulation range and higher energy conversion efficiency. The stator is directly linked to the grid, while the rotor excitation voltage is supplied by converters connected on both the rotor side and the grid side. This configuration enables variable speed constant frequency operation through converter control. This paper first proposes the control approach for the converters: the grid-side converter (GSC) maintains a constant DC capacitor voltage with good dynamic response capability, while the rotor-side converter (RSC) controls the speed to achieve maximum power tracking of wind energy. To improve the wind turbine's fault ride-through capability, a new crowbar protection strategy is proposed for the rotor side by incorporating the instantaneous rotor current, system voltage, and a fixed time delay as key features. Secondly, the control strategy for the photovoltaic power generation system inverter is studied, also adopting maximum power tracking to achieve efficient energy utilization. Then, a control strategy for the storage battery as the main control micro-source is proposed: during grid-connected operation, fixed active and reactive power output is used; during islanded operation, droop control is employed to maintain the stability of the microgrid's voltage and frequency. To ensure a seamless transition from isolated operation to grid-connected operation, a synchronization module is integrated into the battery storage control system. Subsequently, a microgrid model is developed using Matlab/Simulink to simulate the complementary operational characteristics of various micro-sources and the seamless transition of the microgrid operational mode. This process verifies the accuracy and effectiveness of the model.

Keywords—Wind Power Generation System; MPPT; Multi-Energy Microgrid; Storage Batteries

I. INTRODUCTION

The achievement of 'dual carbon' goals necessitates efficient utilization of clean energy sources such as wind and solar power. However, the variability and intermittency of clean energy pose challenges to grid regulation, operation, and safety control. Therefore, addressing the inherent uncertainties of wind and solar power and their impact on grid stability is crucial [1,2]. Wind and solar power can complement each other effectively, and when combined with distributed or centralized new energy generation, storage batteries can mitigate power fluctuations. This represents an effective approach to addressing operational

challenges associated with new energy sources [3]. As a result, hybrid microgrids comprising wind energy, solar energy, and energy storage have garnered significant attention due to their potential for high efficiency and energy savings [4].

Effective coordination and control of micro-sources within a microgrid are crucial for ensuring its stable operation. The Doubly Fed Induction Generator (DFIG) has historically dominated wind power generation due to its cost-effectiveness, small converter capacity, and flexible control capabilities. However, its direct grid-connected stator winding makes the DFIG particularly sensitive to grid voltage faults, necessitating advanced control of both grid-side and rotor-side inverters to ensure low voltage ride-through (LVRT) capability [5]. Reference [6] introduced a hybrid system integrating pumped storage, solar energy, and wind energy, establishing a mathematical model, albeit without providing detailed wind and solar energy model explanations. Reference [7] developed a comprehensive renewable energy system model utilizing solar and wind energy as micro-sources and lithium-ion batteries for storage. Reference [8] proposed models for photovoltaic systems, wind turbines, battery packs, and inverters, using neural networks to design power and energy curves, but lacked detailed micro-source control strategy explanations. Reference [9] described a configuration including PV arrays, diesel generators, wind turbines, and BESS connected to both AC and DC buses, primarily focusing on off-grid operational characteristics. Reference [10] described an autonomous microgrid system that integrates PV panels, wind turbines, batteries, a diesel generator, and an inverter. The study introduced an optimization design approach utilizing a metaheuristic algorithm, though it included oversimplified micro-source modeling and primarily focused on off-grid systems. Reference [11] proposed a model predictive control strategy for grid-connected microgrids utilizing wind and solar energy, emphasizing integrated management of hydrogen-ESS and battery-ESS. Further research is required to ensure stable operation in both off-grid and grid-connected modes, including smooth mode transitions to enhance power quality, especially considering the battery's role as the primary control power source of the microgrid.

Addressing these issues, this study initially investigates models and control strategies for doubly-fed induction wind power generation systems and photovoltaic systems. Furthermore, crowbar protection is integrated on the rotor side of the doubly-fed induction motor to enable LVRT capability. This paper proposes a new low-voltage ride-through activation and deactivation strategy by incorporating the instantaneous

rotor current, system voltage, and a fixed time delay as key features. Subsequently, the study explores control strategies for energy storage batteries: during microgrid grid-connected operations. Synchronous control is also integrated to ensure smooth transitions between operating in islanded mode and connecting to the grid. Lastly, utilizing the MATLAB/Simulink, a hybrid energy microgrid model is constructed.

II. MODELING AND CONTROL OF DOUBLY-FED INDUCTION WIND POWER GENERATION SYSTEM

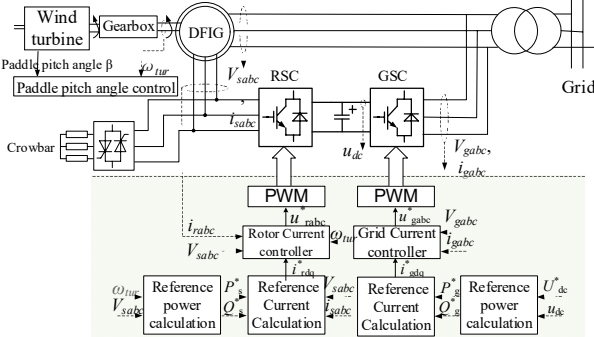


Fig. 1. Structure and control of doubly-fed induction wind turbine

Figure 1 illustrates the configuration of the doubly-fed induction wind turbine. The wind turbine, gearbox, and generator shaft are integrated, facilitating the direct transmission of mechanical energy from the wind turbine to the generator shaft. The DFIG then converts this mechanical energy into electrical energy. Its stator connects directly to the grid, while the rotor interfaces with the grid through converters positioned on both the rotor and grid sides. This configuration supports wind turbine operation at variable speeds with a constant frequency, enabling precise control over active and reactive power equilibrium. The DFIG then converts this mechanical energy into electrical energy. The stator of the DFIG is directly connected to the grid, while the rotor is connected to the grid through rotor-side and grid-side converters. This configuration enables variable-speed constant-frequency operation of the wind turbine, as well as control over real and reactive power equilibrium.

The GSC employs grid voltage-oriented vector control, aiming to achieve excellent dynamic response capability of the DC bus voltage and enable bidirectional power flow. In Figure 1, the reference active power P_g^* for the GSC is determined from the difference between the DC side voltage target U_{dc}^* and the actual voltage u_{dc} , while its reactive power target Q_g^* is set to zero.

If the control method for the RSC is the same as that for the GSC, the d-axis component of the rotor current is associated with the active power output, while the q-axis component is linked to the reactive power output. Thus, by adjusting the d-axis and q-axis components of the rotor reference values, it is possible to manage the generation of active and reactive power outputs.

Based on the previous analysis, the MPPT of the DFIG can be achieved by changing the generator angular speed. First, calculate the reference angular speed corresponding to the

maximum output, then compare the actual angular speed with the reference angular speed to generate control commands, achieving the goal of tracking the maximum power. Figure 2 shows the specific tracking curve. In Figure 1, the rotor angular speed ω_r in the reference power calculation block corresponds to the desired active power reference P_s^* at the maximum power point, whereas the reference value for reactive power Q_s^* is derived from the u_{sabc} of the grid.

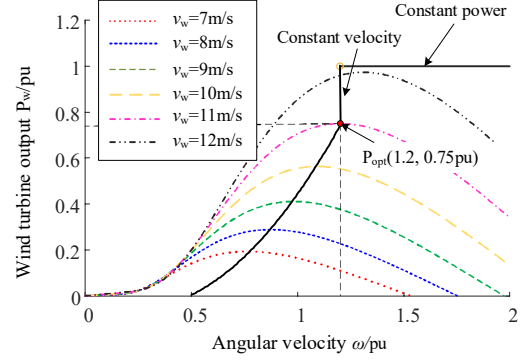


Fig. 2. Wind Turbine MPPT Curve

To prevent damage to the converter caused by the rise in stator and rotor currents, a Crowbar protection circuit, consisting of switches and bypass resistors, is proposed on the rotor side of the doubly-fed induction generator (DFIG). The protection works as follows: during a fault, Crowbar protection is activated by monitoring the over-limit rotor current, which locks the rotor-side converter. The main function of this protection is to provide a bypass circuit for the overcurrent generated by the rotor during grid faults, thus preventing the converter from being damaged by the overcurrent. This allows the wind power generation system to continue supplying reactive power to the grid during faults, preventing voltage collapse. Once the fault is cleared, the bypass resistors are removed by monitoring the grid voltage and rotor current, and the converter returns to normal operation. This Crowbar protection strategy combines the instantaneous values of the three-phase rotor current, grid voltage, and fixed delay, as shown in Figure 3.

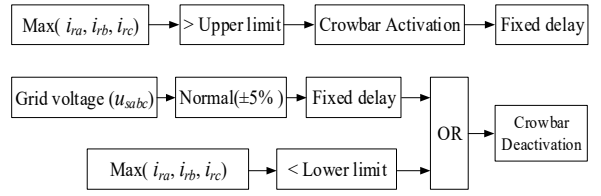


Fig. 3. Crowbar Protection Activation and Deactivation Strategy

III. MATHEMATICAL MODELING AND CONTROL OF PHOTOVOLTAIC POWER GENERATION SYSTEMS

The photovoltaic power generation system first converts solar energy into DC electricity through a photovoltaic array, and then uses inversion technology to convert the DC into AC for connection to the AC bus. To avoid the issues of increased power electronic devices and reduced conversion efficiency associated with multi-level inversion, this article adopts single-stage inversion technology.

Photovoltaic cells are encapsulated into photovoltaic modules through series and parallel connections, and these modules are then further interconnected in series and parallel configurations to form a photovoltaic array according to practical requirements. Considering the correction of the photovoltaic cell's output characteristics with environmental changes, the specific formula for photovoltaic modules can be expressed as,

$$I = I_{SC} [1 - g_1(e^{V/(g_2 V_{OC})} - 1)] \quad (1)$$

where,

$$\begin{aligned} g_1 &= (1 - I_m / I_{SC}) e^{-V_m/(g_2 V_{OC})} \\ g_2 &= (V_m / V_{OC} - 1) / \ln(1 - I_m / I_{SC}) \end{aligned} \quad (2)$$

I_{SC} and V_{OC} signify the current under short-circuit conditions and the voltage under open-circuit conditions, respectively, whereas I_m and V_m indicate the maximum current and voltage at the peak power point. Considering the effects of solar radiation and temperature changes requires introducing correction terms for current (dI) and voltage (dV). This results in the voltage-current relationship of the photovoltaic array that reflects actual environmental variations,

$$I = N_p \left\{ I_{SC} [1 - g_1(e^{(V/N_s - dV)/(g_2 V_{OC})} - 1)] + dI \right\} \quad (3)$$

where,

$$\begin{aligned} dI &= aS / S_{ref} \times dT + (S / S_{ref} - 1) \times I_{SC} \\ dV &= -b \times dT - R_s \times dI \\ dT &= T - T_{ref} \end{aligned} \quad (4)$$

S_{ref} denotes the reference sunlight intensity, T_{ref} represents the reference temperature, and R_s stands for the series resistance of the photovoltaic module. When the sunlight intensity S equals S_{ref} , the temperature coefficients of current and voltage changes are denoted by a and b , respectively. N_s and N_p are the numbers of photovoltaic modules connected in series and parallel.

A photovoltaic inverter achieves independent regulation of active and reactive power by managing the d and q axis elements of its output current. The inverter control uses a dual-loop control of current and voltage. The DC voltage reference value is obtained through MPPT calculation. This reference value is compared against the actual value and processed through PI control to generate the d-axis current reference. The q-axis current reference is derived from the reactive power via a PI loop. The voltage control loop then converts these into d-axis and q-axis voltage reference values, which are then transformed into trigger signals through the Park transformation.

IV. MODELING AND CONTROL OF STORAGE BATTERIES AS MICRO SOURCES

When a multi-energy complementary hybrid microgrid is integrated with the primary grid, the frequency is supported by the main grid, and the battery only needs to suppress active power fluctuations from the wind and photovoltaic systems through control strategies. However, when the hybrid microgrid operates in islanded mode, a main control power source must be present to ensure the steadiness of microgrid voltage and

frequency. Due to the significant environmental impact on wind and solar energy, and to enhance power utilization efficiency, MPPT control is employed for both. Therefore, the battery serves as the main control unit in the microgrid, modulating active and reactive power to ensure stable microgrid operation.

A. Dual closed-loop control

The inverter employs dual-loop control of voltage and current. It utilizes measured voltage as feedback to achieve grid-side voltage tracking by contrasting the feedback signal with the external voltage setpoint. The resultant disparity from this evaluation undergoes PI control to derive the current setpoint for the inner loop. This reference value is then compared with the actual current value and subjected to PI control to achieve modulation and generate trigger signals.

B. Reconnect synchronization control

To avoid transient oscillations when transitioning the microgrid from islanded mode to grid-connected mode and to reduce potential damage to the system, it is proposed to integrate a voltage phase and amplitude compensation module into the droop control loop. This module measures peak voltages and phase differences across the grid connection switch and uses these signals as compensation inputs (highlighted in red in Figure 4) to ensure stability during the grid connection process.

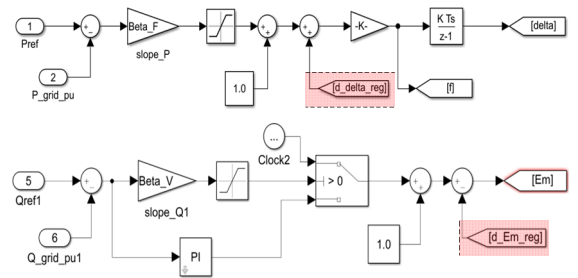


Fig. 4. Synchronous Control

V. OPERATIONAL CHARACTERISTICS OF HYBRID MICROGRID

The hybrid microgrid structure adopted in this article is illustrated in Figure 5.

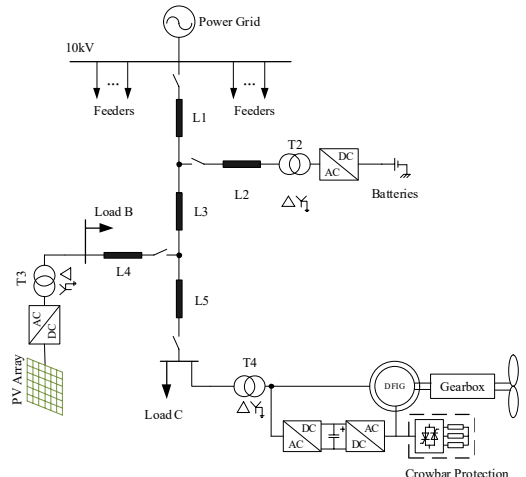


Fig. 5. Multi-Energy Microgrid Structure

A. Stable Operating Characteristics of Microgrids

To verify the effectiveness of maximum power tracking during grid-connected operation, simulation analysis is conducted with varying wind speeds. Initially, the wind speed was 10 meters per second, and it increased to 12 meters per second at $t=3$ seconds. As depicted in Figure 6, the active power output of the DFIG followed the wind speed due to MPPT control after the speed change.

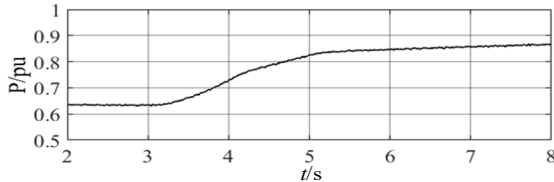


Fig. 6.MPPT of DFIG power system

Assume at $t=4$ s, the microgrid transitions from grid-connected to islanded operation, it reconnects to the grid after 7 seconds, with synchronization beginning $\Delta t=0.7$ s before reconnection to ensure voltage synchronization on both sides of the parallel switch (Figure 7). The microgrid reconnection synchronization process is also depicted in Figure 7. From the observation of the diagram, the voltage on both sides of the grid connection switch (yellow and blue lines) demonstrates a smooth transition of the microgrid from islanded to grid-connected mode through reconnection synchronization control.

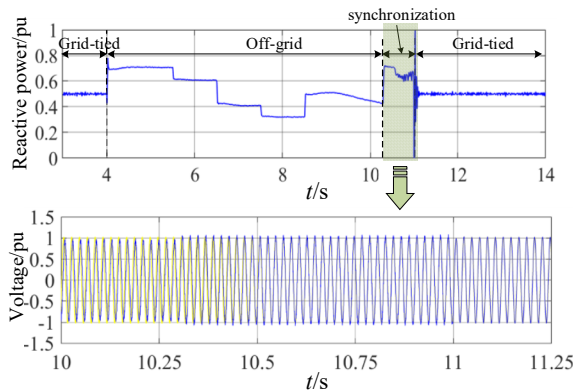


Fig. 7. Mode Transition Between Islanded and Grid-Connected Operation in Microgrids (Including Synchronization Stages)

B. Low Voltage Ride Through of Wind Power Generation Systems

The wind power generation system is operating at a wind velocity of 11 meters per second when, at $t=5$ s, there is a sudden 80% drop in voltage which lasted for 0.2s. The crowbar protection system of the turbine is immediately activated upon detecting the fault, bypassing the RSC while allowing the GSC to continue operating. By detecting the fault current and voltage, the crowbar protection is deactivated after the fault is cleared, and the rotor-side converter resumes operation. Figure 8 shows the transient impact on the stator-side voltage and current. The solid blue line, dashed green line, and dotted pink line in the figures represent phases A, B, and C respectively.

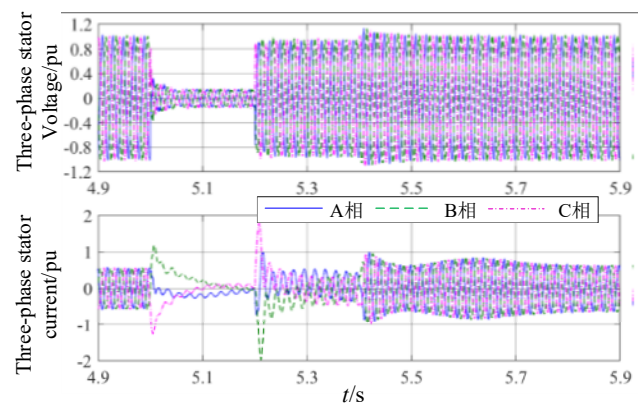


Fig. 8. Three-phase current and voltage on the stator side

VI. CONCLUSION

Through simulation analysis, the MPPT characteristics of wind power and the output characteristics under different microgrid operating modes were investigated. The simulation results show: 1)The reconnection synchronization phase helps the microgrid transition smoothly from islanded mode to grid-connected mode. 2) The effectiveness of the low voltage ride-through (LVRT) strategy was verified.

ACKNOWLEDGMENTS

This work was supported by the Natural Science Foundation of Chongqing (CSTB2023NSCQ-MSX0279) and the Science and Technology Research Program of Chongqing Municipal Education Commission (KJQN202201119).

REFERENCES

- [1] S. Ghoudelbouk, N. B. S. Ali, M. Bayaud, et al.: "Energy Management Strategies for Hybrid Micro Grid System", 2023 IEEE 11th International Conference on Systems and Control (ICSC). December 18-20, 2023 Sousse, Tunisia.
- [2] Q. Peng, X. Wang, Y. Kuang, Y. Wang, et al.: "Hybrid Energy Sharing Mechanism for Integrated Energy Systems Based on the Stackelberg Game", CSEE J. Power Energy, 2021, vol.7, no.5, pp. 911-921.
- [3] X. Cheng, T. Wu, W. Yao and Y. Yang: "Selection Method for New Energy Output Guaranteed Rates Considering Optimal Energy Storage Configuration", CSEE J. Power Energy, 2024, vol.10, no.2, pp. 539-547.
- [4] N. Pang, Q. Meng, M. Nan: "Multi-Criteria Evaluation and Selection of Renewable Energy Battery Energy Storage System-A Case Study of Tibet, China", IEEE Access, 2021, vol. 9, pp. 119857-119870.
- [5] Z. Rafiee, R. Heydari, M. Rafiee, et al.: "Enhancement of the LVRT Capability for DFIG-Based Wind Farms Based on Short-Circuit Capacity", IEEE Syst. J., 2022, vol.16, no.2, pp. 3237-3248.
- [6] T. Ma, H. Yang, L. Lu, et al.: "Technical feasibility study on a standalone hybrid solar-wind system with pumped hydro storage for a remote island in Hong Kong. Renew", Energ., 2014, vol.69, pp. 7-15.
- [7] K. Doshi, V. S. K. V. Harish: "Analysis of a wind-PV battery hybrid renewable energy system for a dc microgrid", Mater Today: Proc., 2021, vol.46, pp. 5454-5457.
- [8] A. J. Aristizábal, J. Herrera, M. Castaneda, et al.: "A new methodology to model and simulate microgrids operating in low latitude countries", Energy Procedia, 2018, vol.157, pp. 825-836.
- [9] Z. Belboul, B. Toual, A. Kouzou, et al.: "Multiobjective Optimization of a Hybrid PV/Wind/Battery/Diesel Generator System Integrated in Microgrid: A Case Study in Djelfa, Algeria", Energies, 2022, vol.15, pp. 1-30.

- [10] K. Karunanithi, S. P. Rajia, S. Ramesh, et al.: “Investigations on Off-Grid Hybrid Renewable Energy Microgrid for Sustainable Development Growth”, J. Circuit Syst. Comp., 2022, vol.31, no.6, pp. 1-21.
- [11] M. B. Abdelghany, A. Al-Durra, F. Gao: “A Coordinated Optimal Operation of a Grid-Connected Wind-Solar Microgrid Incorporating Hybrid Energy Storage Management Systems”, IEEE T. Sustain. Energ., 2024, vol.15, no.1, pp. 39-51.

On the Factors Affecting Battery Unit Contributions to Fault Currents in Grid-Connected Battery Storage Systems

Saleh A. Saleh^{ID}, Senior Member, IEEE, Emre Ozkop^{ID}, Senior Member, IEEE, Marcelo E. Valdes^{ID}, Fellow, IEEE, Ahmet Yuksel^{ID}, Student Member, IEEE, Mohammed Haj-Ahmed^{ID}, Member, IEEE, Zaid G. Sanchez, Member, IEEE, and Claudio S. Mardegan^{ID}, Senior Member, IEEE

Abstract—This article investigates factors affecting the contributions of battery units to fault currents in grid-connected battery storage systems (BSSs). The work in this article is intended to examine the effects of the state-of-charge (SOC) on battery currents that are drawn due to faults. This article also examines the impacts of charger controller actions on the currents drawn from battery units to faults in grid-connected BSSs. The impacts of the SOC and charger controller on battery currents due to faults are examined for the lead-acid, lithium-ion, and nickel–cadmium battery units. Examination results show that the battery currents due to faults are directly dependent on the SOC. Moreover, these results show that actions of charger controller can support the battery terminal voltage, thus preventing the fast reduction of the SOC. The support of the battery terminal voltage helps in limiting the currents drawn from battery units during faults. The effects of the SOC and charger controller are verified using a 1-MW, 3 ϕ grid-connected BSS, which has lead-acid battery units. Several faults have been created during charging and discharging operations, and at different values of SOC. Test results confirm the direct dependence of battery currents (due to faults) on the SOC. In addition, obtained results demonstrate the ability of charger controller to limit the currents

Manuscript received July 20, 2021; revised December 6, 2021; accepted December 14, 2021. Date of publication January 31, 2022; date of current version May 20, 2022. This work is funded in part by a grant from ACOA for Saleh A. Saleh. Paper 2021-CSC-0985.R1, presented at the 2021 IEEE Industry Applications Society Annual Meeting (IAS), Vancouver, BC, Canada and approved for publication in the IEEE TRANSACTIONS ON INDUSTRY APPLICATIONS by the Codes and Standards Committee of the IEEE Industry Applications Society. (*Corresponding author: Saleh A. Saleh.*)

Saleh A. Saleh is with the Department of Electrical and Computer Engineering, University of New Brunswick, Fredericton, NB E3B 5A3, Canada (e-mail: asaleh@unb.ca).

Emre Ozkop is with the Department of Electrical and Electronics Engineering, Karadeniz Technical University (KTU), 61080 Trabzon, Turkey (e-mail: eozkop@ktu.edu.tr).

Marcelo E. Valdes is with the ABB Electrical Solutions, Chapel Hill, NC 27517 USA (e-mail: marcelo.e.valdes@ieee.org).

Ahmet Yuksel is with the Energy Institute Ankara Branch, TUBITAK MAM, METU Campus, 41470 Gebze, Turkey (e-mail: ahmet.yuksel@tubitak.gov.tr).

Mohammed Haj-Ahmed is with the Department of Electrical Engineering, The University of Jordan, Amman 11942, Jordan (e-mail: m.hajahmed@ju.edu.jo).

Zaid G. Sanchez is with the Energy and Environment Center, Carlos Rafael Rodriguez University of Cienfuegos, Cienfuegos 59430, Cuba (e-mail: zgarcia@ucf.edu.cu).

Claudio S. Mardegan is with the EngePower, Santana de Parnaiba, Sao Paulo 06540-030, Brazil (e-mail: claudio.mardegan@engepower.com).

Color versions of one or more figures in this article are available at <https://doi.org/10.1109/TIA.2022.3147149>.

Digital Object Identifier 10.1109/TIA.2022.3147149

drawn from battery units due to faults in different parts of a grid-connected BSS.

Index Terms—Grid-connected battery storage systems, grid-connected power electronic converters, IEEE Standard 946, IEEE Standard 1375, power system faults.

I. INTRODUCTION

A. General

HIGH-POWER-RATED battery storage systems (BSSs) have gained popularity in power systems due to their fast response, high power density, and dynamic charge/discharge characteristics. Applications of BSSs in power systems include supporting voltage/frequency stability, improving the power quality, and mitigating variations of the power generated by renewable energy systems [1]–[9]. Despite their capabilities to enhance power systems functions, the interconnection of BSSs can create challenges for protection systems and devices. Such challenges are created by [1]–[8]

- 1) bidirectional power flows to charge/discharge the BSS;
- 2) actions of the BSS controller to regulate the power flow;
- 3) features of interfacing power electronic converters (PECs); and
- 4) contributions of the BSS to fault currents.

References [10]–[13] provide various aspects for designing accurate and reliable protection systems for interconnected BSSs. Test results of these protection systems have demonstrated their abilities to accommodate bidirectional power flows, actions of BSS controllers, and features of interfacing PECs [1], [13]. However, the accurate determination of BSS contributions to fault currents has not been fully addressed, when considering the actions of BSS controller and features of the interfacing PEC. In this regard, PECs used in interconnected BSSs are typically featured with built-in protection measures to limit the maximum current flowing through their switching elements. Furthermore, actions of the PEC controller are initiated to maintain the voltage on its ac side as close as possible to that of the host grid. Such controller actions represent additional limitations to the maximum current to flow through PEC switching elements during fault and nonfault events. These operational behaviors

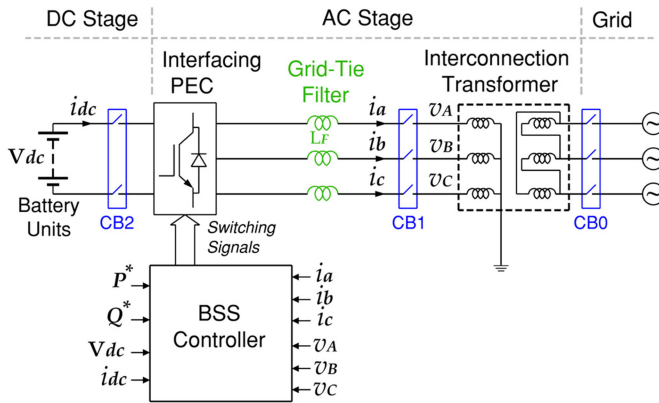


Fig. 1. A circuit diagram for a 3ϕ grid-connected BSS.

of PECs and its controller (used in interconnected BSSs) directly impact the contributions of an interconnected BSS to fault currents.

B. Overview of IEEE Standard 946 and IEEE Standard 1375

BSSs have become essential components in many industrial systems, including data centers, communications systems, renewable energy systems, uninterrupted power supplies, power systems, and others. In these applications, a BSS is considered to have a dc stage and an ac stage that are fed from the utility grid via an interconnection transformer, as shown in Fig. 1. The dc stage is composed of the battery units and protection devices. The ac stage is composed of the interfacing PEC, grid-tie filter, interconnection transformer, grid-synchronizing, and protective devices [1], [3]–[6]. Several industrial sectors have developed standards and best practices for the design, operation, and protection for grid-connected BSSs [1]–[9].

Similar to other components of a power system, grid-connected BSSs can experience various types of faults, which can occur in the dc stage, ac stage, and grid. However, due to the charging and discharging operation of battery units, the behavior of a grid-connected BSS during faults can be influenced by several factors. For example, a fault in the dc stage during the charging operation may trigger a different current from the same fault, when it occurs during the discharging operation. An other example can be a fault in the ac stage may trigger a discharge current that is dependent on the state-of-charge (SOC) of the battery units [1]–[7], [13], [14]. In order to avoid equipment damages and/or service interruptions, grid-connected BSSs have to be featured with adequate protective devices (relays, circuit breakers, and fuses) with proper sizing and settings [1]–[5]. The selection of such protective devices requires determining currents that are triggered by faults at different stages of a grid-connected BSS.

IEEE Standard 1375

This standard [5] details recommended practices for the protection of stationary battery units. These battery units are typically connected to a dc bus that may feed some dc loads, and be connected to several PECs (chargers and inverters). The IEEE Standard 1375 addresses the short-circuit in battery units,

grounding of battery units, and protection devices for battery units. For faults in the dc stage, the IEEE Standard 1375 sets the battery contribution to the fault current based on

- 1) the battery time-constant;
- 2) the equivalent impedance as seen from the fault location; and
- 3) the battery-rated terminal voltage.

IEEE Standard 946

This standard [3] provides recommendations for designing stationary BSSs with a dc bus, dc loads, and multiple PECs (chargers and inverters). The IEEE Standard 946 provides guidance for designing protection systems for stationary BSSs, where protective devices are selected for ac and dc stages based on the maximum possible current triggered by faults in the ac and dc stages. This standard states that the maximum possible fault current is the sum of contributions by the battery units, active dc loads (connected to the dc bus), and filters on both sides of the charging PECs. The IEEE Standard 946 sets the contributions of battery units to faults in the ac or dc stages based on their rated voltages and equivalent impedance as seen from the fault location [1], [3], [10]–[14].

Other reported research works [15], [16] have investigated the protection of BSSs with different structures. In these works, the selection of the protective devices has been based on the IEEE Standards 1375 and 946. Moreover, the fault detection has been adapted from methods used in PEC protection as discussed [13], [17], [18]. Nonetheless, these works have not addressed the battery units contributions to fault currents.

C. Article Objectives and Contributions

Currents triggered by faults in grid-connected BSS have components contributed by the battery units and charger PEC. The existing methods to estimate these contributions do not consider the effects of the SOC and actions of the charger PEC. This article aims to investigate the factors affecting the currents drawn from battery units due to faults in grid-connected BSSs. The objectives of this article can be summarized as follows.

- 1) To examine effects of the controller actions on the currents drawn from battery units due to faults.
- 2) To examine the effects of the SOC on the battery currents during faults in a grid-connected BSS.

Achieving these objectives ensures the following contributions.

- 1) The factors (SOC and actions of BSS controller) affecting the currents drawn from battery units due to faults in grid-connected BSSs.
- 2) The verification of these factors using a 1-MW grid-connected BSS.

II. FAULT CURRENTS IN BATTERY STORAGE SYSTEMS

There exist several approaches to determine fault currents in BSSs. Among these approaches are the IEEE Standard 1375 and IEEE Standard 946, which are intended for stationary BSSs. Fig. 2 depicts the single-line diagram for a stationary BSS.

The IEEE Standards 1375 and 946 determine a fault current, in a stationary BSSs, as a combination of contributions by

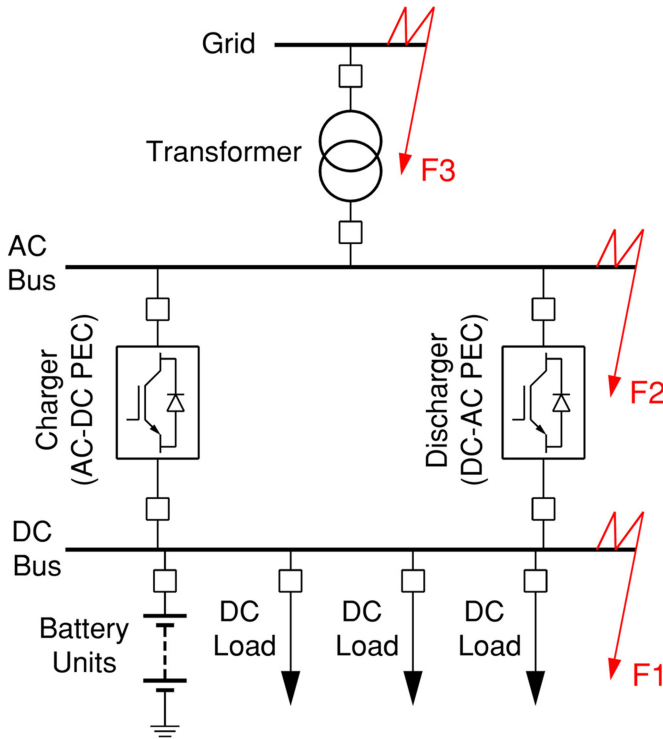


Fig. 2. A single-line diagram of a stationary battery storage systems [1].

the battery units and interfacing PECs (chargers and/or inverters) [1]–[6].

A. Calculating Fault Currents Using IEEE Standard 1375

The IEEE Standard 1375 sets the maximum current triggered by a fault in the dc bus (fault F1 in Fig. 2) as [5]

$$(i_{F1})_{\max} = \frac{V}{R} \left(1 - e^{-\frac{t}{\tau_{bs}}} \right) + 10 (I_{PEC})_{\text{Rated}} \quad (1)$$

where $(i_{F1})_{\max}$ is the maximum fault current triggered by F1, V is the prefault voltage on the terminals of the battery units, R is the equivalent resistance of the battery units, τ_{bs} is battery short-circuit time constant (see Table II in Ref. [5]), and $(I_{PEC})_{\text{Rated}}$ is the rated current of the charger. The IEEE Standard 1375 provides guidance for determining the value of R using the discharge characteristic curve of the battery units.

Remarks Regarding (1)

- 1) The value of $(i_{F1})_{\max}$ is intended only for determining the size and interruption capacity of protective devices to be installed in the dc bus.
- 2) The current contributed by the battery units to F1 is assumed to increase during the interval of $5 \times \tau_{bs}$ after the start F1. Nonetheless, this interval can be long enough for a significant reduction V , thus limiting the current contributed by the battery units.
- 3) The current contributed by the charger cannot exceed the rated pulsing current of individual switching elements comprising the charger. Such a current is less than $10(I_{PEC})_{\text{Rated}}$.

B. Calculating Fault Currents Using IEEE Standard 946

This standard determines the maximum current triggered by a fault in the dc bus (F1) as

$$(i_{F1})_{\max} = \frac{V_{Br}}{R_{eq}} + 10 (I_{PEC})_{\text{Rated}} \quad (2)$$

where V_{Br} is the rated terminal voltage of the battery units, and R_{eq} is the equivalent resistance seen in the location of F1. For a fault in the ac bus (Fault F2 in Fig. 2), the IEEE Standard 946 sets the maximum fault current as [3]

$$(i_{F2})_{\max} = 10 (I_{PEC})_{\text{Rated}} + (i_{acI})_{\max} (1 + e^{-\gamma}) \quad (3)$$

where $(i_{acI})_{\max}$ is the maximum ac current provided by the inverters (see Tables II and III in Ref. [19]), and γ is given as

$$\gamma = \frac{2\pi}{X/R} \left(0.49 - 0.1e^{-\frac{X/R}{3}} \right) \quad (4)$$

with X being the equivalent inductive impedance seen from the location of F2, and R being the equivalent resistance seen from the location of F2.

For a fault on the grid side (fault F3 in Fig. 2), the contributions of the battery units and inverter, $(i_4)_{F3}$, are set by the IEEE Standard 946 as

$$(i_4)_{F3} = 10 (I_{PEC})_{\text{Rated}}. \quad (5)$$

The grid contribution to faults on the grid-side is determined using the IEEE Standard 3002.3 as [19]

$$(i_0)_{F3} = (i_{acG})_{\max} (1 + e^{-\gamma}) \quad (6)$$

where $(i_{acG})_{\max}$ is the peak ac component of the grid current (see Tables II and III in Ref. [17]), and γ is determined by (4) for F3. The maximum current that can be triggered by F3, $(i_{F3})_{\max}$, is stated as

$$(i_{F3})_{\max} = 10 (I_{PEC})_{\text{Rated}} + (i_{acG})_{\max} (1 + e^{-\gamma}). \quad (7)$$

Remarks Regarding (3) and (7)

- 1) The values of $(i_{F2})_{\max}$ and $(i_{F3})_{\max}$, determined using the IEEE Standard 946, are used only for selecting the size and interruption capacity of protective devices in the dc and ac buses.
- 2) The contributions of battery units and inverter to faults in ac bus or grid are limited by the rated current of the inverter.
- 3) The contribution of the grid to fault currents in the ac stage can be determined using the IEEE Standard 3002.3.

III. FACTORS AFFECTING FAULT CURRENTS IN GRID-CONNECTED BSSS

In general, a battery unit can deliver an extremely high current during a short-circuit on its terminals. The short-circuit current delivered by a battery unit can reach more than 40 times its rated discharge current [1]–[4], [13]–[16]. However, short-circuit currents delivered by a battery unit can be affected by the battery type, SOC, protection devices, temperature, and equivalent resistance as seen from the terminals of the battery unit [18].

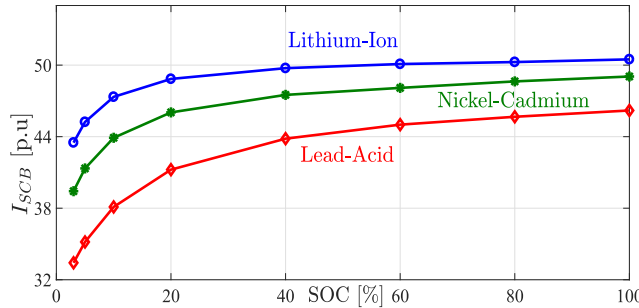


Fig. 3. Maximum short-circuit current at different values of the SOC for lithium-ion, nickel-cadmium, and lead-acid battery units. The base value of I_{SCB} is 8 A, and the value of Δt is $\Delta t = 10$ ms.

A. Effects of the SOC on the Short-Circuit Current

The SOC for a battery unit is a critical parameter that reflects its performance and facilitates its operation. The monitoring of the SOC of a battery unit helps preventing its overdischarge and improving its functions. The impacts of the SOC on the short-circuit of a battery unit can be illustrated by the relationship between the discharge current (I_{DS}) and SOC, that is [20]

$$I_{DS}(t) = \frac{C}{\Delta t} (\text{SOC}(t) - \text{SOC}(t - t_n)) \quad (8)$$

where C is nominal capacity of the battery unit in (Ah), Δt is a time interval, and t_n is set as $t_n = t - \Delta t$.

For purposes of demonstrating the effects of the SOC on the short-circuit current delivered by a battery unit, models for lithium-ion (LI-I), nickel–cadmium (N-C), and lead-acid (L-A) battery units have been created using e-TAP and MATLAB/SIMULINK software packages [21], [22]. These models have been used to test the short-circuit I_{SC} of these battery units at different values of the SOC. Each model is rated for 24 V, 20 A h, and a rated discharge current of 8 A. Fig. 3 shows the maximum short-circuit current at different values of the SOC for each battery unit.

Fig. 3 shows that the SOC value can have a significant influence on the maximum short-circuit current contributed by a battery unit. In addition, Fig. 3 demonstrates that the type of a battery unit has a direct influence on the maximum short-circuit current contributed by that battery unit.

The influences of the SOC on $(I_{SC})_{max}$ are further demonstrated by a comparison with $(I_{SC})_{max}$ determined by the IEEE Standards 946 and 1375 for three battery units. The internal resistances and short-circuit time constant for the LI-I, N-C, and L-A battery units are obtained from the data in Refs. [3] and [5] as follows.

- 1) LI-I battery unit: $R_B = 0.05 \Omega$.
- 2) N-C battery unit: $R_B = 0.073 \Omega$.
- 3) L-A unit: $R_B = 0.104 \Omega$.
- 4) Short-circuit time constant $\tau_{SC} = 3.3$ ms (Table II in Ref. [5]).

The values of $(I_{SCB})_{max}$ are determined by the IEEE Standards 946 and 1375 as follows.

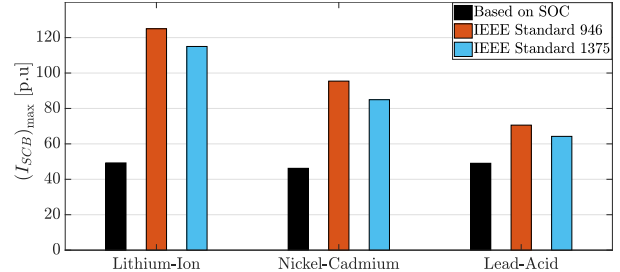


Fig. 4. Maximum short-circuit current for the tested lithium-ion, nickel–cadmium, and lead-acid battery units determined based on SOC= 100%, and IEEE Standards 946 and 1375. The base value of I_{SCB} is 8 A.

1) IEEE Standard 946:

$$(I_{SCB})_{max} = \frac{V_{Br}}{R_B} \quad (9)$$

with V_{Br} being the rated terminal voltage.

2) IEEE standard 1375:

$$(I_{SCB})_{max} = \frac{V}{R_B} \left(1 - e^{-\frac{t}{\tau_{bs}}} \right) \quad (10)$$

with V being the terminal voltage before the short-circuit.

Fig. 4 shows $(I_{SCB})_{max}$ for the three battery units determined based on the SOC, as well as the IEEE Standards 946 and 1375. It can be seen from Fig. 4 that the IEEE Standards 946 and 1375 yield $(I_{SCB})_{max}$ with higher values than that determined based on SOC. The differences between values of $(I_{SCB})_{max}$ (as determined by IEEE Standards 1375 and 946, as well as the SOC) are due to the fact that IEEE Standards 1375 and 946 use rated values of terminal and internal voltages of the battery unit. These differences in $(I_{SCB})_{max}$ are observed for the LI-I, N-C, and L-A battery units.

B. Effects of Controller Actions on the Short-Circuit Current

Battery chargers are usually operated by constant voltage and/or constant current controllers. Constant voltage controllers are designed to operate the charger (ac–dc PEC) to maintain the battery terminal voltage at a constant value by adjusting the charging current. Constant current controllers are designed to operate the charger to maintain a constant charging current until the battery terminal voltage meets a desired value [23], [24]. Refs. [23] and [24] have several designs for charger controllers.

A constant voltage-controlled 3ϕ charger (thyristor or switched ac–dc PEC) produces an average dc voltage, V_{dc} (over the n th switching interval) on its dc side as [24]

$$V_{dc}(n) = \frac{3}{2} V_{Ps} \cdot (k(n))_{CV} \quad (11)$$

where $(k(n))_{CV}$ ($0 \leq (k(n))_{CV} \leq 1$) is related to the actions of the constant voltage controller during n , and V_{Ps} is the rms value of the line voltage on the ac side of the 3ϕ charger. The value of $(k(n))_{CV}$ depends on the type of charger as follows.

- 1) For a thyristor-based charger, $(k(n))_{CV}$ is

$$(k(n))_{CV} = \cos(\alpha(n))$$

with $\alpha(n)$ being the firing angle during n .

2) For a transistor-based charger, $(k(n))_{CV}$ is

$$(k(n))_{CV} = m_a(n)$$

with $m_a(n)$ being the modulation index during n .

The output dc current during n , I_{dc} , can be stated as [23], [24]

$$I_{dc}(n) = \frac{2(k(n))_{CV}}{\pi} \left(|i_a(n)| + |i_b(n)| + |i_c(n)| \right) \quad (12)$$

where $i_a(n), i_b(n), i_c(n)$ are the 3ϕ currents on the ac side of the charger during n . The value of $(k(n))_{CV}$ during n is set by the constant voltage controller to achieve

$$V_{dc}(n) \xrightarrow{(k(n))_{CV}} V_{dc}^*(n) \quad (13)$$

where $V_{dc}^*(n)$ is the desired output dc voltage.

A constant current-controlled charger will maintain I_{dc} fixed as long as $V_{dc} = V_{dc}^*$. For a 3ϕ charger operated by a constant current controller, the output dc voltage during n is stated as [24]

$$V_{dc}(n) = \frac{3}{2} V_s \cdot (1 - k_{CC} \Delta V_{dc}(n)) \quad (14)$$

where k_{CC} is a parameter of the constant current controller, and $\Delta V_{dc}(n)$ is given as

$$\Delta V_{dc}(n) = V_{dc}^* - V_{dc}(n).$$

The dc current, during n , produced by a 3ϕ constant current-controlled charger can be expressed as [24]

$$I_{dc}(n) = (\beta_0 + \beta_1 \Delta V_{dc}(n)) (|i_a(n)| + |i_b(n)| + |i_c(n)|) \quad (15)$$

with β_0, β_1 being parameters for the constant current controller.

A short-circuit on the dc bus results in a sudden reduction of V_{dc} , and thus $\Delta V_{dc}(n) \neq 0$. The sudden reduction in V_{dc} triggers a response from the charger controller to restore V_{dc} to its desired value V_{dc}^* . A constant voltage controller will increase $(k(n))_{CV}$ to restore V_{dc} , causing I_{dc} to increase [see (12)]. A similar action will be initiated by a constant current controller, which tends to achieve $\Delta V_{dc} \rightarrow 0$. This action causes I_{dc} to increase as in (15). Since the response of a battery unit is slower than the response of the charger controller, fast increases in I_{dc} can affect I_{SCB} (the short-circuit current contributed by a battery unit).

The actions of charger controller (constant voltage or constant current) to restore V_{dc} will slow the decay of SOC, as a high current is drawn from the battery unit (due to a short-circuit at the dc bus). This can be illustrated by [25]

$$V_{dc}(n) = V_{B0} - \frac{C \cdot h_p (1 - SOC(n))}{SOC(n)} - \left(\frac{h_p}{SOC(n)} + R_B \right) (I_{DS})_{Rated} \quad (16)$$

where V_{B0} is the battery internal potential, and h_p is the polarization coefficient. The effects of V_{dc} on the SOC for LI-I, N-C, and L-A battery units are demonstrated in Fig. 5. The curves in Fig. 5 are obtained using the following data [21], [22]:

- 1) Li-I: $V_{B0} = 25.59$ V, $h_p = 0.1484$, $(I_{DS})_{Rated} = 8$ A, $R_B = 0.050$ Ω.

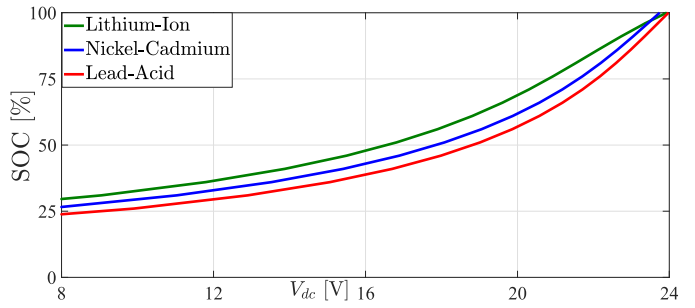


Fig. 5. Effects of changing V_{dc} (produced by the charger) on the SOC for the tested lithium-ion, nickel–cadmium, and lead-acid battery units.

- 2) N-C: $V_{B0} = 25.70$ V, $h_p = 0.1406$, $(I_{DS})_{Rated} = 8$ A, $R_B = 0.073$ Ω.
- 3) L-A: $V_{B0} = 25.93$ V, $h_p = 0.1373$, $(I_{DS})_{Rated} = 8$ A, $R_B = 0.104$ Ω.

It can be observed from Fig. 5 that regulating the terminal voltage of a battery unit will prevent the fast decay of the SOC. This observation is applicable to the three tested battery units. The adjustment of the SOC will change the maximum short-circuit current that can be drawn from a battery unit. It should be noted that Fig. 5 does not provide any relationship between the SOC and battery open-circuit terminal voltage (VOC).

In order to demonstrate the effects of charger controller actions, two models for chargers were constructed. One model was for a 3ϕ , 0.25 kW, 60 Hz, thyristor-based charger, which had an ac-side line voltage of 20 V. Another model was for a 3ϕ , 0.25 kW, 60 Hz, insulated-gate bipolar transistor (IGBT)-based charger, which had an ac-side line voltage of 20 V [21], [22]. Each of the tested LI-I, N-C, and L-A battery units was separately fed by the two chargers. Constant voltage and constant current controllers were designed, and employed to operate the thyristor and IGBT chargers. For each charger feeding each battery unit, a short-circuit was created at the terminals of the battery unit. For each short-circuit, $(I_{SCB})_{max}$ was measured, and plotted as shown in Fig. 6.

It can be seen from Fig. 6 that both charger controllers managed to reduce $(I_{SCB})_{max}$ (relative to Fig. 4) for the three tested battery units. The reductions in $(I_{SCB})_{max}$ could also be observed for thyristor and IGBT chargers, when operated by constant voltage and constant current controllers. Observed reductions in $(I_{SCB})_{max}$ resulted from actions of the charger controller to adjust V_{dc} to its desired value during the short circuit at the dc bus. The adjustments in V_{dc} did allow the SOC to quickly change, thus limiting the discharge current during the short-circuit at the dc bus.

IV. TESTING BATTERY CONTRIBUTIONS TO FAULT CURRENTS IN GRID-CONNECTED BSSS

The testing of battery contributions to fault currents was conducted for a 1-MW grid-connected BSS. This BSS was modeled using e-TAP, and its controller parameters were selected using MATLAB/SIMULINK tools. The tested BSS was operated for frequency regulation, which required a frequency

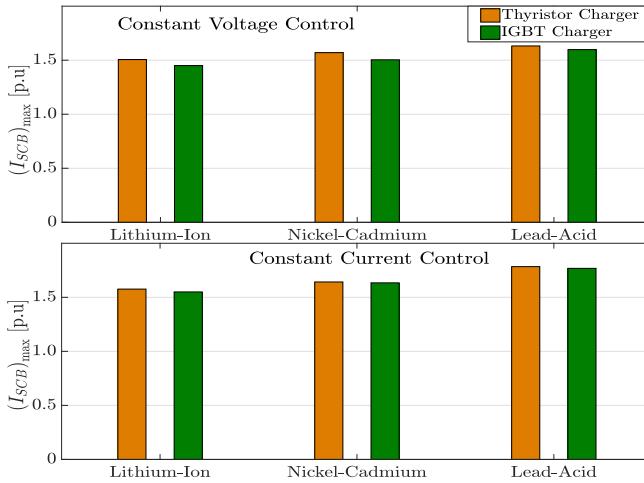


Fig. 6. Effects of charger controller actions on $(I_{SCB})_{\max}$ for the tested lithium-ion, nickel-cadmium, and lead-acid battery units. The base value of I_{SCB} is 8 A. $k_{CV} = 0.84$, $k_{CC} = 0.63$, $\beta_1 = 0.92$, $\beta_2 = 0.24$.

TABLE I
DATA FOR THE TEST 1 MW, 3 ϕ , GRID-CONNECTED BSS

Parameter	Value
Rated DC Bus Voltage	960 V
Battery Type	Lead-Acid
Energy Capacity	240 kWh
Capacity	260 Ah
Maximum DoD	20%
Parallel Strings	30
R_B for Each String	6.26 Ω
Rated Current for Each String	34.5 A
Charger Type	Bi-Directional IGBT PEC
Charger Rated Current	770 A
Charger Pulsed Current	1600 A (over 1.5 ms)
Charger Controller	Constant Voltage: $k_{CV} = 0.78$
Frequency Droop Controller	$G_D = 0.3$, DB = [49.9, 50.1] Hz
Rated AC Bus Voltage	960 V
Grid-Tie Filter	$L = 6.0$ mH
Grid-Connection Transformer	1.2 MVA, 11/0.96 kV, 60 Hz, Δ -Y

G_D : the droop constant; DB: the frequency dead-band; DoD: depth of discharge.

droop controller as a second controller. The data for the tested grid-connected BSS is listed in Table I. Fig. 7 shows a single-line diagram for the test grid-connected BSS.

The e-TAP model for the test grid-connected BSS was tested for several fault events. The following fault events are presented and discussed in this article.

- 1) Charging and discharging operations of the BSS.
- 2) Short-circuit on the dc bus during the charging operation.
- 3) Line-to-ground fault during the discharging operation.
- 4) Line-to-line fault during the charging operation.

A. Charging and Discharging Operations of the BSS

This test aimed to investigate the normal operating modes of the test grid-connected BSS. The charging and discharging operations were tested through the load flow analysis. The charging operation was conducted with SOC set as SOC = 80%. It should be noted that SOC = 80% was selected as it represented the lowest acceptable SOC for the used L-A battery units. As a

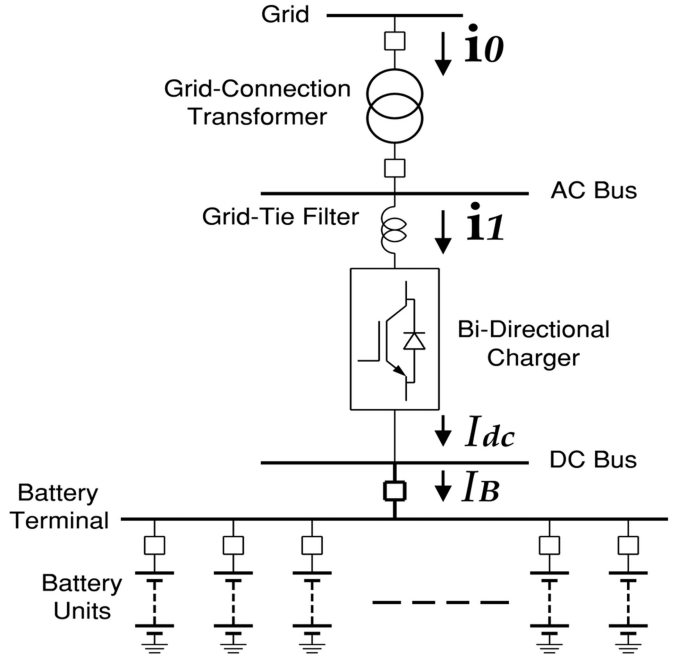


Fig. 7. A single-line diagram for the test 1 MW grid-connected BSS. $i_0 = [i_{a0}, i_{b0}, i_{c0}]$ and $i_1 = [i_{a1}, i_{b1}, i_{c1}]$.

TABLE II
LOAD FLOW RESULTS FOR THE CHARGING OPERATION OF THE GRID-CONNECTED BSS

Quantity	Magnitude	Angle
i_{a0}	46.1 A	-2.86°
i_{b0}	46.1 A	-122.86°
i_{c0}	46.1 A	117.14°
i_{a1}	595.8 A	-3.03°
i_{b1}	595.8 A	-123.03°
i_{c1}	595.8 A	116.97°
I_{dc}	436.4 A	
I_B	436.4 A	
v_a	0.95 kV	-0.03°
v_b	0.95 kV	-120.03°
v_c	0.95 kV	119.97°
V_{dc}	0.96 kV	

result, SOC = 80% provided the maximum charging current for the tested grid-connected BSS. The 3 ϕ currents i_0 , i_1 , dc currents I_{dc} , I_B , ac bus voltage, and dc bus voltage were collected for the charging operation as listed in Table II. The discharging operation was initialized for SOC = 96%, to ensure high discharging current. The grid-connected BSS injected power into the grid as follows:

$$P = 992 \text{ [kW]} \text{ and } Q = 86 \text{ [kVAR].} \quad (17)$$

Table III lists the 3 ϕ currents i_0 , i_1 , dc currents I_{dc} , I_B , ac bus voltage, and dc bus voltage obtained from the load flow analysis for the discharging operation of the grid-connected BSS. It should be noted that the currents in Table III were taken with the convention that currents flowing from the grid had positive sign.

The results in Tables II and III demonstrated stable charging and discharging operations of the tested grid-connected BSS.

TABLE III
LOAD FLOW RESULTS FOR THE DISCHARGING OPERATION OF THE GRID-CONNECTED BSS

Quantity	Magnitude	Angle
i_{a0}	-52.9 A	-5.15°
i_{b0}	-52.9 A	-125.15°
i_{c0}	-52.9 A	114.85°
i_{a1}	-683.7 A	-4.62°
i_{b1}	-683.7 A	-124.62°
i_{c1}	-683.7 A	115.38°
I_{dc}	-500.8 A	
I_B	-500.8 A	
v_a	0.95 kV	-0.02°
v_b	0.95 kV	-120.02°
v_c	0.95 kV	119.98°
V_{dc}	0.96 kV	

TABLE IV
RESULTS FOR THE SHORT-CIRCUIT AT THE DC BUS DURING CHARGING OPERATION WITH THE CONSTANT VOLTAGE CONTROLLER

Quantity	Magnitude	Angle
i_{a0}	16.73 A	-30.1°
i_{b0}	16.73 A	-150.1°
i_{c0}	16.73 A	89.9°
i_{a1}	216.09 A	-32.2°
i_{b1}	216.09 A	-152.3°
i_{c1}	216.09 A	87.8°
I_{dc}	198.27 A	
I_B	-282.94 A	
v_a	0.91 kV	-3.8°
v_b	0.91 kV	-123.8°
v_c	0.91 kV	116.2°
V_{dc}	0.92 kV	

These results also showed that during steady-state conditions, I_{dc} and I_B had identical values. This feature was a result from the absence of any loads connected to the dc bus, and confirmed the power flow from and to the battery units. Finally, the data obtained from this test provided a base case for the steady-state operation of the grid-connected BSS.

B. Short-Circuit on the DC Bus During the Charging Operation

The objective of this test was to examine the contribution of the battery units to a short-circuit at the dc bus during the charging operation. The short-circuit was created through a resistance of $R_F = 2 \Omega$, with SOC = 80%. The short-circuit analysis tool of e-TAP was used to determine the currents through the grid-connected BSS. The 3 ϕ currents i_0 , i_1 , dc currents I_{dc} , I_B , ac bus voltage, and dc bus voltage were collected for the short-circuit at the dc bus, and listed in Table IV. It should be noted that I_B had a negative sign to indicate its direction was out of the battery units. For purposes of demonstrating the effects of the charger controller, the short-circuit at the dc bus was created with constant voltage controller disabled. Table V lists the 3 ϕ currents i_0 , i_1 , dc currents I_{dc} , I_B , ac bus voltage, and dc bus voltage for the short-circuit at the dc bus.

The results of this test demonstrated the effects of the charger controller on battery contributions to the short-circuit current. The data in Tables IV and V showed that actions of the constant voltage controller supported V_{dc} by increasing I_{dc} . These actions

TABLE V
RESULTS FOR THE SHORT-CIRCUIT AT THE DC BUS DURING CHARGING OPERATION WITHOUT THE CONSTANT VOLTAGE CONTROLLER

Quantity	Magnitude	Angle
i_{a0}	4.78 A	-11.9°
i_{b0}	4.78 A	-131.8°
i_{c0}	4.78 A	108.1°
i_{a1}	61.74 A	-13.2°
i_{b1}	61.74 A	-133.1°
i_{c1}	61.74 A	106.8°
I_{dc}	45.22 A	
I_B	-418.79 A	
v_a	0.92 kV	-0.04°
v_b	0.92 kV	-120.04°
v_c	0.92 kV	119.96°
V_{dc}	0.83 kV	

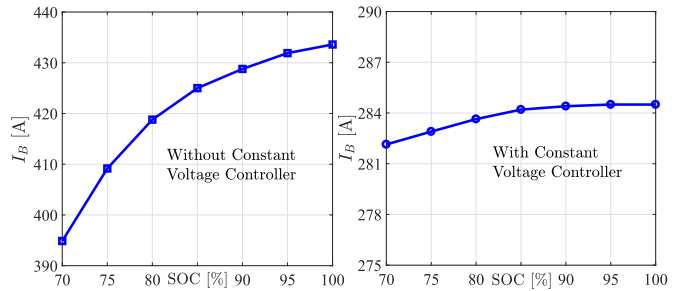


Fig. 8. Contribution of the battery units to the short-circuit current, I_B , at the dc bus for different values of SOC, with and without the actions of the constant voltage controller.

resulted in limiting I_B flowing to the short-circuit branch. The changes in I_{dc} , I_B , and V_{dc} could be seen from the values of these quantities in Tables IV and V.

In order to demonstrate the effects of charger controller and SOC on I_B , the short-circuit at the dc bus was created for several values of SOC with and without the actions of the constant voltage controller. Fig. 8 shows I_B due to the short-circuit at the dc bus, for several values of SOC with and without the charger controller. The results in Fig. 8 showed the effects of the charger controller and SOC on the contribution of battery units to the short-circuit current. Actions of the constant voltage controller regulated V_{dc} (prevented its fast decline) and limited I_B (prevented its transient increase) during the short-circuit at the dc bus.

C. Line-to-Ground Fault During the Discharging Operation

This test aimed to examine the contribution of the battery units to a line-to-ground fault on the ac bus during the discharging operation. The phase B -to-ground fault was created through a resistance of $R_F = 1 \Omega$, with SOC = 100%. The short circuit analysis tool of e-TAP was used to determine the currents through the grid-connected BSS. The 3 ϕ currents i_0 , i_1 , dc currents I_{dc} , I_B , ac bus voltage, and dc bus voltage were collected for the fault at the ac bus, and listed in Table VI.

The data in Table VI shows that the phase B -to-ground fault on the ac bus caused an imbalance in the currents flowing from the BSS to the grid, as well as the currents on the grid side. The ground fault also resulted in a significant increase in i_{b1} .

TABLE VI
RESULTS FOR THE PHASE B-TO-GROUND FAULT AT THE AC BUS DURING THE DISCHARGING OPERATION

Quantity	Magnitude	Angle
i_{a0}	475.78 A	-54.1°
i_{b0}	521.87 A	125.4°
i_{c0}	46.28 A	-60°
i_{a1}	601.38 A	-30°
i_{b1}	2376.78 A	-52.9°
i_{c1}	601.38 A	90°
I_{dc}	466.87 A	
I_B	466.87 A	
v_a	0.90 kV	-1.9°
v_b	0.80 kV	-63.2°
v_c	0.92 kV	122.2°
V_{dc}	0.94 kV	

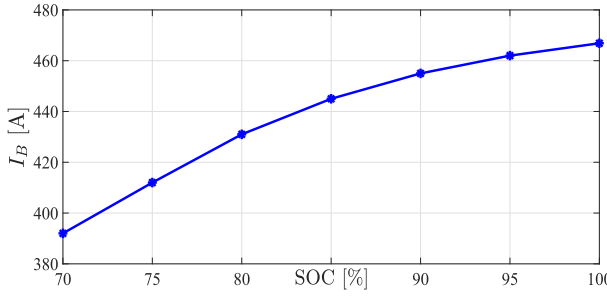


Fig. 9. Effects of SOC on I_B triggered by the phase B -to-ground at the ac bus.

due to the increase in I_B and the reversal of i_{b0} . Moreover, the line-to-ground fault on the ac bus caused changes in the ac voltages and V_{dc} . The phase B -to-ground at the ac bus was tested for several values of SOC to demonstrate the effects of SOC on I_B . Fig. 9 shows I_B , triggered by the fault at the ac bus, for several values of SOC.

The results in Fig. 9 showed that the SOC affected the contribution of battery units to the line-to-ground fault at the ac bus. The effects of SOC on I_B triggered by the phase B -to-ground fault were in agreement with the results in Fig. 8 (the short-circuit at the dc bus).

D. Line-to-Line Fault During the Charging Operation

The objective of this test was to examine the contribution of battery units to a line-to-line fault in the charger PEC during the charging operation. The phase A -to-phase C fault was created through a resistance of $R_F = 3 \Omega$, with $SOC = 88\%$, and with the constant voltage controller. Table VII lists the 3ϕ currents i_0 , i_1 , dc currents I_{dc} , I_B , ac bus voltage, and dc bus voltage for the tested asymmetrical fault in the charger PEC.

The data in Table VII shows that the phase A -to-phase C fault in the charger PEC resulted in unbalanced currents flowing from the grid, and voltages on ac bus. The line-to-line fault caused significant increases in i_{a1} and i_{c1} due to the fault. In addition, I_B and I_{dc} reversed their direction as battery units contributed to the fault current. Finally, the phase A -to-phase C fault in the charger PEC changed the ac voltages and V_{dc} . Similar to the other tested faults, this line-to-line fault was tested for several values of SOC, as shown in Fig. 10.

TABLE VII
RESULTS FOR THE PHASE A -TO-PHASE C FAULT IN THE CHARGER PEC DURING THE CHARGING OPERATION

Quantity	Magnitude	Angle
i_{a0}	49.6 A	-47.6°
i_{b0}	24.1 A	-115.9°
i_{c0}	49.6 A	90.9°
i_{a1}	640.8 A	-52.4°
i_{b1}	310.6 A	-118.9°
i_{c1}	641.1 A	94.8°
I_{dc}	-328.2 A	
I_B	-388.2 A	
v_a	0.92 kV	-1.9°
v_b	0.94 kV	-122.2°
v_c	0.91 kV	174.9°
V_{dc}	0.92 kV	

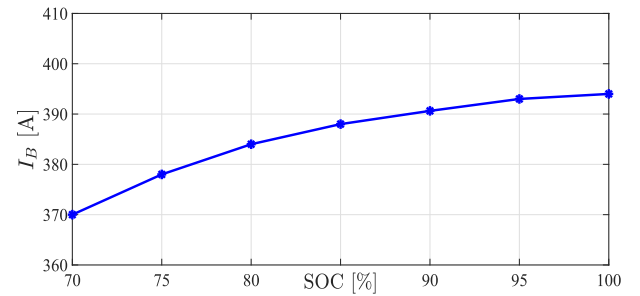


Fig. 10. Effects of SOC on I_B triggered by a line-to-line fault (phase A -to-phase C fault) in the charger PEC.

TABLE VIII
BATTERY CURRENT AND TERMINAL VOLTAGE DURING FAULTS IN DIFFERENT LOCATIONS IN A GRID-CONNECTED BSS

Fault	With Controller	Without Controller	IEEE Standards
Short-Circuit at DC Bus	$I_B = 286.5$ A $V_{dc} = 0.93$ kV	$I_B = 433.6$ A $V_{dc} = 0.78$ kV	$I_B = 4064.9$ A $V_{dc} = 0.96$ kV
3 ϕ Fault at AC Bus	$I_B = 329.7$ A $V_{dc} = 0.94$ kV	$I_B = 731.3$ A $V_{dc} = 0.72$ kV	$I_B = 7700$ A $V_{dc} = 0.96$ kV
Line-to-Ground at AC Bus	$I_B = 466.8$ A $V_{dc} = 0.94$ kV	$I_B = 882.4$ A $V_{dc} = 0.77$ kV	$I_B = 7700$ A $V_{dc} = 0.96$ kV
Line-to-Line at AC Bus	$I_B = 394.6$ A $V_{dc} = 0.93$ kV	$I_B = 782.2$ A $V_{dc} = 0.80$ kV	$I_B = 7700$ A $V_{dc} = 0.96$ kV

Fig. 10 demonstrated the effects of SOC on the contribution of battery units to the line-to-line fault in the charger PEC. The results in Fig. 10 were consistent with results obtained from other faults, where SOC had direct impacts on I_B .

The tested cases have demonstrated the effects of the SOC and actions of the charger controller on the contributions of battery units to faults in grid-connected BSSs. In all tested cases, low SOC values have resulted in lower currents drawn from battery units due to fault events. Furthermore, actions of charger controller have been found able to limit the reductions in dc voltage at battery terminals. These controller actions have resulted in limiting the contributions of battery units to fault currents. These effects of the SOC and charger controller have been observed for faults in different locations of the grid-connected BSS. Finally, the effects of the SOC and charger controller on battery contributions to fault currents have been observed during the charging and discharging operation. Table VIII provides a summary of I_B and V_{dc} for different fault events at different

locations of a grid-connected BSS. These values are determined at SOC = 100%, with and without controller actions (constant voltage), and using IEEE Standard 1375 and IEEE Standard 946.

The data in Table VIII shows the effects of the charger controller on battery currents and terminal voltage due to faults in different locations of a grid-connected BSS. The data in Table VIII together with Figs. 9 and 10 confirm the effects of the SOC and charger controller on I_B and V_{dc} for fault conditions. Observed effects of the SOC and charger controller on I_B and V_{dc} can be used for developing accurate and reliable detection of faults in grid-connected BSSs.

V. CONCLUSION

This article has presented the factors that affect battery contributions to fault currents in grid-connected BSSs. The typical determination of battery contributions to fault currents is based on IEEE Standards 1375 and 946, which use the rated battery terminal voltage and internal resistance. These standards are widely used to select and size protective devices for battery units used in stationary BSSs (see Fig. 2). Grid-connected BSSs do not have loads connected to the dc bus, and thus battery currents only flow through the charger PEC. Battery currents are directly related to the SOC and actions of the charger controller. Effects of the SOC and charger controller on the currents drawn from battery units due to faults have been investigated for the charging and discharging operations. Investigation results have shown that the currents drawn from battery units, due to faults, are directly related to the SOC and actions of charger controller. Observed effects can be critical for developing fault detection methods to improve the protection and operation of grid-connected BSSs.

REFERENCES

- [1] S. A. Saleh *et al.*, "Factors affecting battery unit contributions to fault currents in grid-connected battery storage systems," in *Proc. 56th IEEE IAS Annu. Meeting Conf.*, Vancouver, BC, Canada, 2021, pp. 1–8.
- [2] *IEEE Application Guide for IEEE Standard for Interconnecting Distributed Resources With Electric Power Systems*, IEEE Std. 1547.2-2008, 2008, pp. 1–217.
- [3] *IEEE Recommended Practice for the Design of DC Power Systems for Stationary Applications*, IEEE Std. 946–2020, 2020, pp. 1–74.
- [4] *IEEE Recommended Practice for Sizing Lead-Acid Batteries for Stand Alone Photovoltaic (PV) Systems*, IEEE Std.1013-2007, 2007, pp. 1–50.
- [5] *IEEE Guide for the Protection of Stationary Battery Systems*, IEEE Std. 1375–1998, 1998, pp. 1–59, doi: [10.1109/IEEESTD.1998.87900](https://doi.org/10.1109/IEEESTD.1998.87900).
- [6] *IEEE Recommended Practice for Industrial and Commercial Power Systems Analysis*, IEEE Std. 399–1997, 1997, pp. 1–488.
- [7] S. A. Saleh, E. Ozkop, C. Mardegan, and M. Valdes, "Bus differential protection for buses interconnecting battery storage systems," in *Proc. 57th IEEE IAS Ind. Commercial Power Syst. Tech. Conf.*, Las Vegas, NV, USA, 2021, pp. 1–8.
- [8] G. Wang *et al.*, "A review of power electronics for grid connection of utility-scale battery energy storage systems," *IEEE Trans. Sustain. Energy*, vol. 7, no. 4, pp. 1778–1790, Oct. 2016.
- [9] M. Farhadi and O. Mohammed, "Energy storage technologies for high-power applications," *IEEE Trans. Ind. Appl.*, vol. 52, no. 3, pp. 1953–1961, May/Jun. 2016.
- [10] M. A. Haj-ahmed and M. S. Illindala, "Investigation of protection schemes for flexible distribution of energy and storage resources in an industrial microgrid," *IEEE Trans. Ind. Appl.*, vol. 51, no. 3, pp. 2071–2080, May/Jun. 2015.
- [11] P. Rakhra, P. J. Norman, S. D. A. Fletcher, S. J. Galloway, and G. M. Burt, "Evaluation of the impact of high-bandwidth energy-storage systems on DC protection," *IEEE Trans. Power Del.*, vol. 31, no. 2, pp. 586–595, Apr. 2016.
- [12] S. A. Saleh, C. Richard, X. F. St-Onge, J. Meng, and E. Castillo-Guerra, "Comparing the performance of protection coordination and digital modular protection for grid-connected battery storage systems," *IEEE Trans. Ind. Appl.*, vol. 55, no. 3, pp. 2440–2454, May/Jun. 2019.
- [13] S. A. Saleh, R. McSheffery, and R. Meng, "Testing the performance of the digital modular protection for grid-connected battery storage systems," *IEEE Trans. Ind. Appl.*, vol. 54, no. 3, pp. 2059–2070, May/Jun. 2018.
- [14] A. C. Gaunce *et al.*, "DC arc flash: Testing and modeling incidents in a 125-V substation battery backup system," *IEEE Trans. Ind. Appl.*, vol. 56, no. 3, pp. 2138–2147, May/Jun. 2020.
- [15] R. Hedding and P. Hayes, "Protection of battery energy storage system," in *Proc. 64th IEEE Annu. Conf. Protective Relay Engineers*, College Station, TX, USA, 2011, pp. 155–159.
- [16] L. Tao, G. Chunlin, Y. Jingjing, W. Jianing, Z. Chenliang, and M. Huiyuan, "Analysis on DC side protection strategy for grounded power battery energy storage system," in *Proc. IEEE IAS Ind. Commercial Power Syst. Asia Tech. Conf.*, Weihai, China, 2020, pp. 1006–1011.
- [17] S. A. Saleh, A. S. Aljankawey, B. Alsayid, and M. S. Abu-Khaizaran, "Influences of power electronic converters on voltage-current behaviors during faults in DGUs-Part II: Photovoltaic systems," *IEEE Trans. Ind. Appl.*, vol. 51, no. 4, pp. 2832–2845, Jul./Aug. 2015.
- [18] W. Hartmann, R. Fleck, R. Graba, and M. Hergt, "Characterization of commercial IGBT modules for pulsed power applications," in *Proc. 13th IEEE Pulsed Power Conf.*, San Francisco, CA, USA, 2013, pp. 1–4.
- [19] *IEEE Recommended Practice for Conducting Short-Circuit Studies and Analysis of Industrial and Commercial Power Systems*, IEEE Std. 3002.3–2018, 2018, pp. 1–184.
- [20] M. Coleman, C. K. Lee, C. Zhu, and W. G. Hurley, "State-of-charge determination from EMF voltage estimation: Using impedance, terminal voltage, and current for lead-acid and lithium-ion batteries," *IEEE Trans. Ind. Electron.*, vol. 54, no. 5, pp. 2550–2557, Oct. 2007.
- [21] *Power System Toolbox User Guide*. Natick, MA, USA: Math Works, 2017.
- [22] "e-TAP 19.01: Short circuit analysis toolbox," e-TAP, Irvine, CA, USA, 2019.
- [23] D. Sha, G. Xu, and Y. Xu, "Utility direct interfaced charger/discharger employing unified voltage balance control for cascaded H-bridge units and decentralized control for CF-DAB modules," *IEEE Trans. Ind. Electron.*, vol. 64, no. 10, pp. 7831–7841, Oct. 2017.
- [24] R. Metidji, B. Metidji, and B. Mendil, "Design and implementation of a unity power factor fuzzy battery charger using an ultrasparse matrix rectifier," *IEEE Trans. Power Electron.*, vol. 28, no. 5, pp. 2269–2276, May 2013.
- [25] L. Y. Wang, M. P. Polis, G. G. Yin, W. Chen, Y. Fu, and C. C. Mi, "Battery cell identification and SOC estimation using string terminal voltage measurements," *IEEE Trans. Veh. Technol.*, vol. 61, no. 7, pp. 2925–2935, Sep. 2012.



Saleh A. Saleh (Senior Member, IEEE) received the B.Sc. degree in electrical engineering from Bir Ziet University, West Bank, Palestine, in 1996, and the M.Eng. and Ph.D. degrees in electrical engineering from the Memorial University of Newfoundland, St. John's, NL, Canada, in 2003 and 2007, respectively, with a scholarship from the Natural Sciences and Engineering Research Council of Canada (NSERC).

He was with Palestinian Technical College, West Bank, Palestine, as an Instructor and a Program Coordinator until 2001. From 2007 to 2011, he was a Faculty and a Researcher with Marine Institute, Memorial University of Newfoundland. He is currently a Professor with the Department of Electrical and Computer Engineering, University of New Brunswick, Fredericton, NB, Canada. His research interests include power system operation, control, and protection, digital protection of energy conversion systems, power electronic converter design, analysis, operation, and control, renewable energy systems, motor drives, and digital signal processing applications in power systems, power electronic converters, and motor drives.

Dr. Saleh's research works are supported by the Natural Sciences and Engineering Research Council and New Brunswick Innovation Foundation. He is a registered Professional Engineer in the Provinces of Newfoundland and Labrador and New Brunswick, Canada. He is a recipient of the 2015 Harrison McCain Young Scholars Award and the 2020 University of New Brunswick Merit Award.



Emre Ozkop (Senior Member, IEEE) received the B.Sc.E. degree in electrical and electronics engineering from Gazi University, Ankara, Turkey, in 2003, and the M.Sc.E. and Ph.D. degrees in electrical engineering from Karadeniz Technical University (KTU), Trabzon, Turkey, in 2006 and 2012, respectively.

He is currently an Associate Professor with the Department of Electrical and Electronics Engineering, KTU. He was a Visiting Scholar with the University of New Brunswick, Fredericton, NB, Canada, in 2015 and 2017. His research interests include power electronics, intelligent control systems, power systems protection, control, and grounding, renewable energy systems operation, control, and protection, and smart grid implementation and deployment.



Marcelo E. Valdes (Fellow, IEEE) received the B.S. degree in electrical engineering from Cornell University, Ithaca, NY, USA, in 1977.

He was with GE for 41 years in the field engineering, sales, product management, marketing, and application engineering. He was with the Electrical Products Division, ABB, Cary, NC, USA, in 2018. He is a registered Professional Engineer. He has authored or coauthored more than 35 technical papers for IEEE and other engineering forums. He holds 28 patents in the field electrical distribution and control.

Valdes was the Chair of various IEEE PES and IAS chapters in Northern California, and the Chair of the 2014 IEEE Electrical Safety Workshop (IEEE-ESW). He is the Chair of the IEEE 1683-2014 working group for the IEEE P1683 Guide for Specification and Selection of Low Voltage Motor Control Centers with Enhanced Safety Features. He is active in various IEEE working groups, mostly in electrical safety and power system protection. He has participated in CSA Z462, the Canadian Electrical Safety Standard, NFPA 70, the NEC, and NFPA 70B NFPA's Electrical Maintenance Standard. He has received recognition for his contributions from the Pulp & Paper Industry Committee and IEEE Electrical Safety Committee, and has received the 2015 Pulp & Paper Industry Committee Meritorious Engineering Award, the Excellence in Prevention Through Design Technical Award, and the IEEE IAS Applications Magazine First Prize Article Award in 2014.



Ahmet Yuksel (Student Member, IEEE) received the B.Sc. and M.Sc. degrees in electrical and electronics engineering from Karadeniz Technical University (KTU), Trabzon, Turkey, in 2015 and 2018, respectively. He is currently working toward the Ph.D. degree in electrical engineering with Gazi University, Ankara, Turkey.

He is a Researcher with the Energy Institute of Scientific and Technological Research Council of Turkey (TUBITAK), Marmara Research Center (MRC), Ankara, Turkey. His research interests include power electronic converter design, analysis, operation, control, and renewable energy systems.



Mohammed Haj-Ahmed (Member, IEEE) received the B.Sc. degree from the University of Jordan, Amman, Jordan, in 2006, and the M.Sc. and Ph.D. degrees from Ohio State University, Columbus, OH, USA, in 2011 and 2015, respectively, all in electrical engineering.

Since 2015, he has been with the Department of Electrical and Computer Engineering, University of Jordan, where he is currently an Associate Professor. His research interests include power systems control and protection, power system communication, microgrid protection, renewable energy systems, and control systems.

Dr. Haj-Ahmed is registered with Jordan Engineers Association.



Zaid G. Sanchez (Member, IEEE) received the B.Sc. degree from the Universidad Central de las Villas, Santa Clara, Cuba, in 2002, and the M.Sc. and Ph.D. degrees from the Universidad Central de las Villas, Cuba, in 2004 and 2011, respectively, all in electrical engineering.

Since 2012, he has been an Assistant Professor with the Center for Energy and Environment Studies (CEEMA), University of Cienfuegos, Cienfuegos, Cuba, where he is currently a Professor and the Head. From 2018 to 2019, he was a Visiting Scholar with Emera & NB Power Research Center for Smart Grid Technologies, University of New Brunswick, Fredericton, NB, Canada. His research interests include power system modeling, stability analysis, planning, and protection. His research works also involve integrating and operating renewable energy sources, as well as developing and planning smart grid functions.



Claudio S. Mardegan (Senior Member, IEEE) received the Electrical Engineering degree in Electrical Power System Engineer from the Federal University of Itajuba (UNIFEI), Itajuba, Brazil, in 1980.

He is a Director of EngePower, Osasco, Brazil. He is a Consulting Engineer for Brazilian and multinational companies and an Instructor of several courses in protection engineering. He is the Author of the Proteção e Seletividade em Sistemas Elétricos Industriais (Protection and Coordination in Electrical Power Systems; Attitude Editorial, 2012). He is the Co-Author of the Guide for Low Voltage and Medium Voltage (Brazilian Standards NBR-5410 and NBR-14039). He has authored many papers in the areas of power system analysis and protection systems. He has extensive experience in design, assembling, commissioning, maintenance, consulting, and analysis of power systems and protection systems.

Mardegan has participated in the Generator Grounding, Forensics, DC, and 3004-Series Working Groups in IEEE Industrial Applications Society.

Online Fault Detection and Classification of a Grid-Connected Microgrid System Based on Discrete Wavelet Transformation

Mamata Takhellambam
 Department of Electrical Engineering
 National Institute of Technology, Manipur
 Imphal, India
 mmtatakh@gmail.com

Shuma Adhikari
 Department of Electrical Engineering
 National Institute of Technology, Manipur
 Imphal, India
 shumaadhikari@gmail.com

Laishram Khumanleima Chanu
 Department of Electrical Engineering
 National Institute of Technology, Manipur
 Imphal, India
 khumanleimac@gmail.com

Abstract— The increasing integration of renewable energy sources and distributed energy resources in modern power systems has led to the emergence of microgrids as a viable solution for enhancing energy resilience and sustainability. However, the dynamic and decentralized nature of microgrids poses challenges in ensuring their reliable operation, which calls for developing efficient fault detection and identification methods. In this research, discrete wavelet transformation (DWT) presents a unique online fault detection and identification method for a grid-connected microgrid system. The focus of the research is mainly on the detection and identification of faults by collecting the detailed coefficients of various types of faults, such as line-line fault, line-to-ground fault, double line-to-ground fault, etc., with the help of multi-resolution analysis (MRA) in DWT at different parameters (type of fault, line length, fault resistance, ground resistance) with the ideal selection of the mother-based wavelet. To validate the effectiveness of the proposed methodology, an extensive simulation of the grid-integrated microgrid model consisting of a PV powerplant and Battery storage system has been carried out in the MATLAB/SIMULINK software. The simulation results illustrate the effectiveness and robustness of the suggested technique based on DWT in detecting and classifying various types of faults of a microgrid system with satisfactory results.

Keywords— *Discrete wavelet transformation (DWT), fault classification, fault detection, microgrid (MG), multiresolution analysis (MRA)*.

I. INTRODUCTION

The quest for more sustainable and efficient energy systems has captured the focus of researchers, leading to increased exploration of the concept of distributed microgrids (MG). Potential electrical challenges might arise in an MG due to several distributed energy resources (DERs), communication equipment, and fluctuating loads that constitute the MG. The MG can function both in grid-connected as well as islanded modes. The diverse qualities of microgrid components can impact safety, underscoring the imperative to prioritize safety measures before introducing technologies [1].

Various types of fault detection methods have been proposed by researchers for the protection of different power

system networks. The detection, classification, and localization of faults in an MG system utilizing a long short-term memory (LSTM) network based on deep learning, demonstrates its superiority over many other techniques as discussed in [2], [3]. However, it can only be implemented in a time-based sequential network and it is more complicated than traditional recurrent neural networks (RNN). Md. Daisy *et. al* [4], identify faulty branches through a comparison between the actual fault voltage magnitude difference and the simulated faults; however, its precision decreases in the presence of faults with high resistances, leading to a reduction in the fault voltage difference. The phase difference between the positive-sequence fault element of the bus voltage and the positive-sequence fault elements of the currents in the feeders presented in [5], can only be used in grid-connected mode. DC line short circuit fault detection scheme was proposed based on RSFC as given in [6], which needs communication requirements for backup protection. A low-cost micro phasor presented by G. S. Dua *et. al* [7] is used as differential protection for a microgrid system based on the positive sequence current angle of the line. Phase angle, the magnitude of voltage and the voltage-based classifier's phase angle are used for the classification of fault in a PV microgrid system or any three-phase system [8]. The fault detection for the LVDC distribution system is based on mathematical morphology as suggested in [9], and [10]. A. Q.Khan *et. al* [11], present a unique hybrid approach that uses readings from phase measurement units (PMUs) for fault detection and the location of transmission lines in an interconnected network. The majority of these fault detection schemes either have communicational requirements, complexity in training, problems regarding noise, only based on time domain or inability to function efficiently during high impedance conditions.

Discrete wavelet transformation (DWT) is specialized in extracting features both in time and frequency [13], [14]. Wavelet transformation is most suited for the feature extraction and fault analysis of nonlinear transient signals of a network [15], [16]. DWT has become a prominent method for the

detection and classification of faults in a power system network because of their high accuracy and simplicity of operation.

Considering the survey above, the contribution of this study can be summed up as:

- 1) A novel yet simple fault detection and identification technique of a grid-connected microgrid based on multiresolution analysis of DWT is proposed.
- 2) Employed a five-level decomposition using Daubechies (Db5) as the mother wavelet for feature extraction for the analysis of all types of three-phase faults (symmetrical & unsymmetrical) in a grid-connected microgrid system.
- 3) The effectiveness of the proposed algorithm is studied by varying certain parameters such as types of faults, line length, fault resistance and ground resistance.
- 4) The main characteristic of the proposed algorithm is its simplicity of operation, accuracy, sensitivity and reliability.

In accordance with the contribution mentioned above, the organization of this paper can be given as: Section II briefly describes the modelling of the microgrid and application of the proposed methodology. Section III gives the result and discussion of the fault analysis of the grid-connected microgrid systems. Finally, Section IV addresses the conclusion of the proposed work.

II. MODELLING OF MICROGRID AND METHODOLOGY

A. Modelling of the microgrid system

The power system consisting of a utility grid, PV plant, and the battery is simulated in the MATLAB Simulink software, and various fault conditions are introduced in the system to carry out the detection and identification of faults. The block diagram of the grid-integrated microgrid is given in Fig 1.

The system consists of 154MW, 35.5kV, 50Hz Main grid and PV power plant as sources, a Battery energy storage system is incorporated to maintain a constant power supply, a 3.4/0.4kv step-down transformer, a transmission time parameter network to set the desired length of transmission line, VI measurement to measure the current and voltages, Constant AC as well as DC load, a three-phase fault parameter to introduced different types of faults.

B. Methodology: Wavelet transformation

The wavelet transform is an efficient signal analysis tool that represents signals in the time-frequency domain, offering a unique capability to localize features in both time and frequency. This is particularly advantageous in applications of fault detection, where precise time and frequency information is crucial, wavelet transform excels by extracting transient details from nonstationary signals like fault currents. Its ability to provide a detailed time-frequency representation makes it a valuable tool for identifying faults in dynamic systems.[12][13][14].

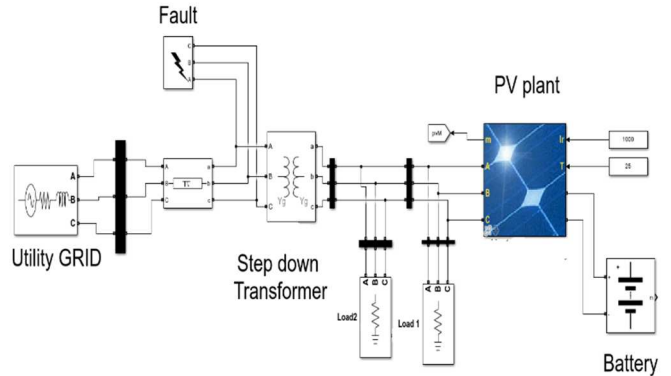


Fig.1 Block diagram of the grid-connected microgrid system.

1) Continuous Wavelet Transform: The Continuous Wavelet Transform (CWT) is a mathematical technique utilized for the analysis of signals across time and frequency domains. In contrast to the Discrete Wavelet Transform (DWT), it utilizes a continuous spectrum of wavelet scales, allowing for the investigation of signals at various frequencies and time scales.

2) Discrete wavelet Transformation: Discrete wavelet transformation is mostly preferred for the practical application of wavelet transformation because of its ability to decompose any time series signal into approximation and detailed coefficient using scaling function and mother wavelet respectively [13]. Discrete wavelet transformation can be represented as

$$DWT(f, n) = \frac{1}{\sqrt{a_0}} \sum_{k=0}^{N-1} f(k) \varphi\left(\frac{n-k a_0}{a_0}\right) \quad (1)$$

where, n and k are integers, f , a_0 , ka_0 are frequency, scaling and translational constant and $\varphi(n)$ is the mother wavelet.

The signals undergo decomposition as they pass through a high-pass filter and a low-pass filter producing the detail and approximate coefficient [15]. The process of decomposition is carried out in multi-resolution analysis until the desired detailed

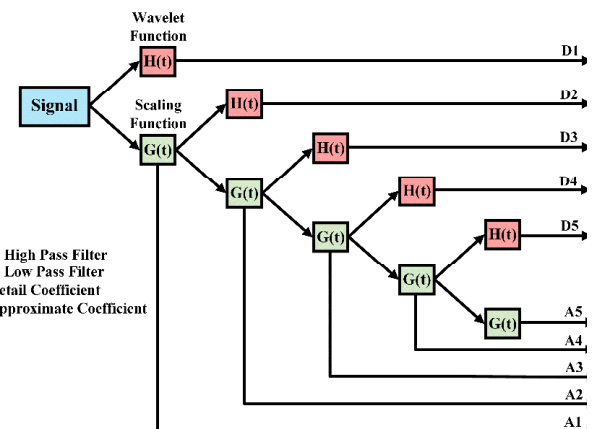


Fig 2: Five-level decomposition of multi-resolution analysis of DWT

TABLE I: FAULTS PARAMETERS WITH CONSIDERING CONSTRAINTS.

Types of Faults	Fault location	Fault resistance, R_f	Ground resistance, R_g	Frequency
LL, LLL, LLLG,	10km, 15km	0.001 Ω , 4 Ω	0.01 Ω , 1 Ω	50Hz
LG, LLG, no fault				

coefficient is obtained. Fig 2 shows the 5-level decomposition of multi-resolution analysis (MRA) of DWT.

3) *Data collection:* The fault analysis of the system is carried out by running the system with various parameters given in Table I. To implement wavelet transformation, data for the three-phase currents (I_a, I_b, I_c) and ground current (I_g) are initially collected.

A detailed flowchart of the fault detection and classification using discrete wavelet transformation is shown in Fig 3.

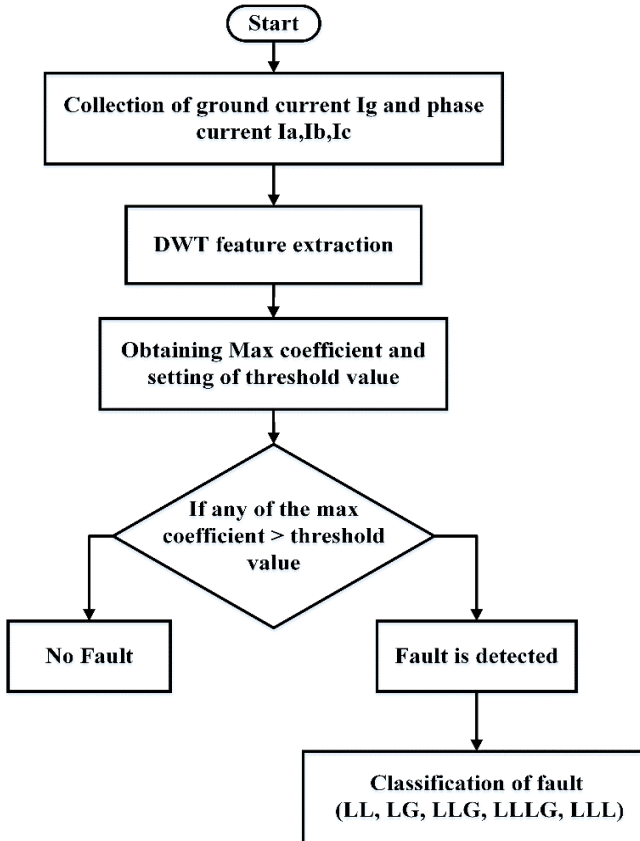


Fig 3: Flowchart of the proposed fault detection and classification technique

4) *Feature Extraction:* A five-level decomposition using Multi-Resolution Analysis for the Discrete Wavelet Transform (DWT) is performed, with db5 chosen as the mother wavelet. Detailed and approximate coefficients are collected from the multi-level decomposition, allowing the calculation of the maximum coefficient for each phase.

5) *Detection and Classification of Faults:* Comparing the maximum coefficient values of each phase under various fault conditions, a threshold value is determined. If the maximum

coefficient value exceeds this threshold, the fault is detected. Conversely, if the maximum coefficient value is below the threshold, the system is considered to be operating under normal conditions.

In summary, the implementation involves collecting current data, performing a five-level DWT decomposition, calculating maximum coefficients for each phase, and comparing these values against a predetermined threshold to detect and identify faults or confirm normal system operation.

III. RESULT AND DISCUSSION:

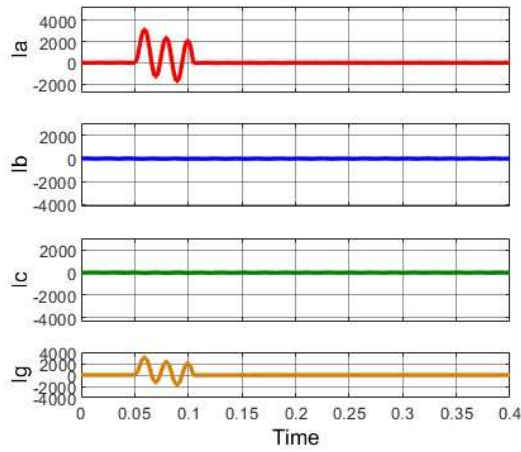
For the fault analysis of the Microgrid system through wavelet transformation, twelve different types of fault case conditions are considered at two different locations and by varying the fault resistance and ground resistance. The max coefficient of each phase and ground current during each fault condition at two different locations obtained from the 5-level wavelet decomposition are given in Table II and Table III.

TABLE II: MAX COEFFICIENT OF ALL PHASES AND GROUND CURRENT AT FAULT LOCATION=10 KM, $R_f=0.001\Omega$, $R_g=0.01\Omega$

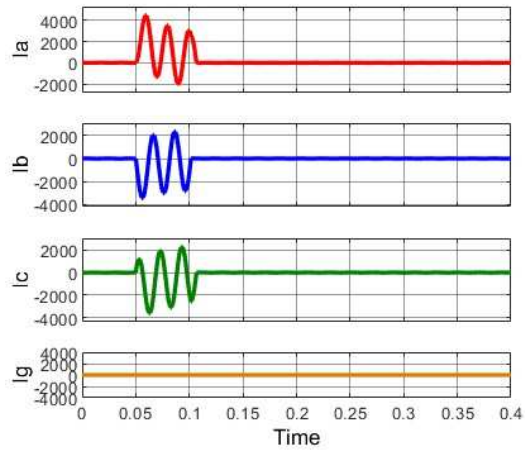
Type of fault	Max coefficient of I_A	Max coefficient of I_B	Max coefficient of I_C	Max coefficient of I_G
LLL fault (ABC)	331.0906	293.2174	456.1936	228.3255
LLL fault (ABC)	257.0019	257.0019	456.1936	0.0078
LL fault (AB)	258.0296	294.4383	0.7683	0.0118
LL fault (BC)	1.3998	312.2131	466.7824	0.0016
LL fault (AC)	156.6219	1.8915	217.1023	0.0011
LG fault (AG)	414.4931	1.8915	1.8915	407.6142
LG fault (BG)	2.0781	228.6775	1.9875	226.9005
LG fault (CG)	3.7479	4.0071	346.6666	344.5329
LLG fault (ABG)	220.4998	253.5786	1.9917	348.6715
LLG fault (BCG)	2.9639	311.5292	459.7038	238.0438
LLG fault (ACG)	244.6850	3.7223	364.0455	292.5052
No fault condition	1.3998	1.8915	0.7683	1.7667e-11

The maximum coefficient of all the phase currents and ground currents, at the fault location is 10km, $R_f=0.001 \Omega$ and $R_g=0.01 \Omega$ is given in Table II. It can be seen from all the fault case conditions considered in the table above that the maximum coefficient of the current during no fault condition is remarkably smaller (with the highest maximum coefficient of the healthy line recorded as 4.0071) than that of the maximum coefficient value of the phase with fault.

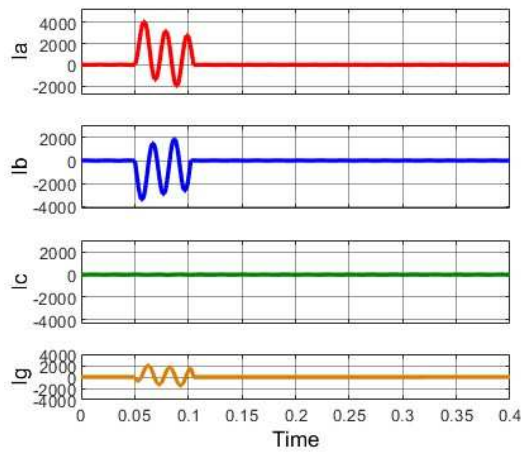
From Table III, it can be observed that during fault conditions the value of the max coefficient of the faulty phase is considerably larger than that of the phase with no fault. The highest value of the max coefficient of phase current under no fault is found to be 4.0071. It can be concluded from both



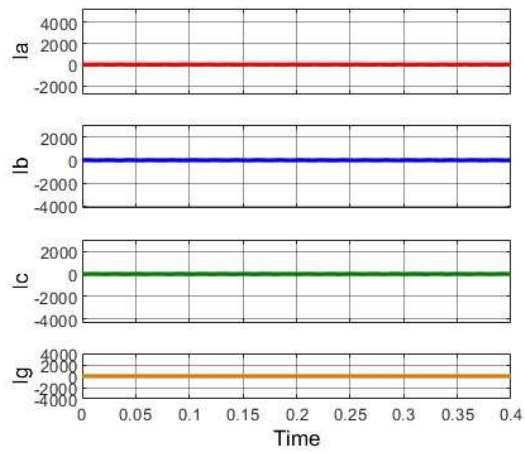
(a)



(b)



(c)



(d)

Fig. 5 Current waveform when a fault is applied from 0.05 to 0.1 sec during (a)AG fault (b)ABC fault (c)ABG fault (d) no fault condition.

TABLE III: MAX COEFFICIENT OF ALL PHASES AND GROUND CURRENT AT FAULT LOCATION=15 KM, $R_f=4\Omega$, $R_g=1\Omega$.

Type of fault	Max coefficient of I_A	Max coefficient of I_B	Max coefficient of I_C	Max coefficient of I_G
LLLG fault (ABCG)	412.9636	232.2204	392.9984	256.1650
LLL fault (ABC)	59.6944	232.2204	392.9984	0.0119
LL fault (AB)	218.8406	105.7227	0.6970	0.0120
LL fault (BC)	1.4017	242.3942	404.3273	0.0068
LL fault (AC)	136.8620	1.7772	184.7678	0.0069
LG fault (AG)	34.5555	2.0688	2.0617	32.9325
LG fault (BG)	3.5333	165.1459	3.5892	164.1666
LG fault (CG)	2.9413	1.8156	277.5770	276.2598
LLG fault (ABG)	128.9696	227.2795	2.3721	159.2801
LLG fault (BCG)	2.1810	237.1425	397.8139	97.0552
LLG fault (ACG)	396.2905	2.4061	298.6797	271.4048
No fault condition	1.4017	1.7772	0.6970	3.1167e-12

observations that fault can be distinguished by comparing the maximum coefficient value of all the phase currents to a common standard reference value. If the max coefficient value of any phase current exceeds 10, it indicates the presence of a fault in that phase. This simple threshold comparison allows for the straightforward identification of faults based on the magnitude of the maximum coefficient value.

From the current waveform given in Fig 5 (a), it can be seen that the magnitude of phase current I_a and ground current I_g drastically increases from 0.05 to 0.1 sec when the fault is introduced, which indicates the presence of a fault in I_a and I_g resulting in AG fault. Likewise in the case of Fig. 5(b) magnitude of I_a , I_b and I_c , increases drastically giving rise to ABC fault. In Fig. 5(c) huge rise in the magnitude of I_a , I_b and I_c can be seen, indicating the presence of ABG fault, while in Fig. 5(d), no sudden changes in the magnitude of current are observed, which indicates that there is no fault in any line. From Fig. 6 it can be observed that the phase current in I_a , and I_b , abruptly increases from 0.05 sec to 0.1 sec which informs the presence of a fault in lines A and B (i.e. AB fault). It can be concluded from the observation that the phase current of the

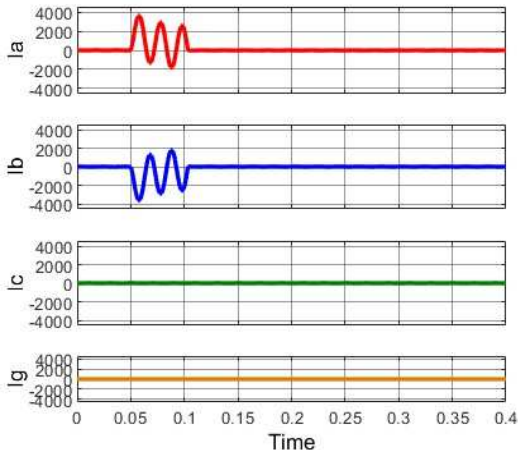


Fig. 6 Current waveform when a fault is applied from 0.05 to 0.1 sec during (e) AB fault

faulty line abruptly increases during fault conditions and under no-fault conditions there is not a sudden rise in current.

It can be observed from the comparative analysis of the proposed technique, that DWT is superior to the conventional ANN in classifying symmetrical and unsymmetrical fault, unlike the ANN which classifies only the symmetrical fault[17]. Also, DWT is not limited to the detection and classification of faults in a power system network with a short transmission line and low impedance network like that of the fuzzy logic [18] and voltage magnitude difference technique[4].

IV. CONCLUSION

This study emphasizes the utilization of Discrete wavelet transformation for real-time fault detection and classification in a grid-connected microgrid system. The multi-resource analysis decomposition of discrete wavelet transformation proves effective in differentiating the faulty and healthy lines under different fault conditions. Notably, the results demonstrate that the fault of the microgrid system can be analyzed effectively by distinguishing standard fault index values.

REFERENCE

- [1] Seyed Amir Hosseini, Behrooz Taheri, Seyed Hossein Hesamedin Sadeghi & Adel Nasiri “An Overview of DC Microgrid Protection Schemes and the Factors Involved” Electric Power Components and Systems, 0(0): 1–31, 2023
- [2] Bappa Roy, Aribam Deleena Devi, Faisal Alsaif, Shuma Adhikari, Subir Datta, K.Jilenkumari Devi, sager Alsulamy, and Taha Selim Ustun , “Deep Learning Based Relay for Online Fault Detection, Classification, and Fault Location in a Grid-Connected Microgrid”, IEEE Access, Vol. 11, June 2023.
- [3] Taha Selim Ustun, Shuichi Sugahara, Masaichi Suzuki, Jun Hashimoto and Kenji Otani “Power Hardware in-the-Loop Testing to Analyze Fault Behavior of Smart Inverters in Distribution Networks” Sustainability 2020, 12, 9365.
- [4] Mohammad Daisy, Rahman Dashti Mahmood Hosseini Aliabadi, Hamid Reza Shaker, “Fault location in power grids using substation voltage magnitude differences: A comprehensive technique for transmission lines, distribution networks, and AC/DC microgrids”, Measurement, Vol 220, Oct 2023.
- [5] Fan Zhang and Longhua Mu “A Fault Detection Method of Microgrids with Grid-Connected Inverter Interfaced Distributed Generators Based on the PQ Control Strategy”, IEEE Access, Vol.10, Sept. 2018.
- [6] Guangyang Zhou, Minxiao Han, Shaahin Filizadeh , Zhi Geng, and Xiaohui Zhang, “A Fault Detection Scheme in MTDC Systems Using a Superconducting Fault Current Limiter”, IEEE Systems Journal, Vol 16, No.3 September 2022.
- [7] Gagandeep Singh Dua, Barjeet Tyagi and Vishal Kumar, “Microgrid Differential Protection Based on Superimposed Current Angle Employing Synchrophasors” IEEE Transactions on Industrial Informatics, Vol. 19, No. 8, August 2023.
- [8] A. Hooshyar, E. F. El-Saadany and M. Sanaye-Pasand, "Fault Type Classification in Microgrids Including Photovoltaic DGs," in IEEE Transactions on Smart Grid, vol. 7, no. 5, pp. 2218-2229, Sept. 2016.
- [9] Yun-Sik Oh *et. al*, “Fault detection scheme based on mathematical morphology in last mile radial low voltage DC distribution networks”, International Journal of Electrical Power & Energy Systems, Volume 106, 2019, Pages 520-527.
- [10] Marija Culjak , Hrvoje Pandžić and Juraj Havelka , “Mathematical Morphology-Based Fault Detection in Radial DC Microgrids Considering Fault Current From VSC” IEEE TRANSACTIONS ON SMART GRID, VOL. 14, NO. 4, JULY 2023
- [11] Abdul Qayyum Khan, Qudrat Ullah, Muhammad Sarwar, Sufi Tabassum Gul, Naeem Iqbal “Transmission Line Fault Detection and Identification in an Interconnected Power Network using Phasor Measurement Units” IFAC Papers Online 51-24 (2018) 1356–1363.
- [12] Debi Prasad Mishra, Subhransu Ranjan Samantaray “A Combined Wavelet and Data-Mining Based Intelligent Protection Scheme for Microgrid” IEEE Transactions on Smart Grid, 2015
- [13] Stephane G. Mallat “A Theory for Multiresolution Signal Decomposition: The Wavelet Representation”, IEEE Transactions on Pattern Analysis and Machine Intelligence, Vol 11, No. 7, July 1989
- [14] Azriyenni Azhari Zakri, *et. Al*, “Extract Fault Signal via DWT and Penetration of SVM for Fault Classification at Power System Transmission” 2nd International Conference on Electrical Engineering and Informatics (ICon EEI 2018), Batam - Indonesia, 16th-17th October, 2018.
- [15] Julie Matarweh, Reziq Mustaklem, Anas Saleem, Omar Mohamed “The Application of Discrete Wavelet Transform to Classification of Power Transmission System Faults” 2019 IEEE Jordan International Joint Conference on Electrical Engineering and Information Technology (JEEIT).
- [16] D.K.J.S Jayamaha and A.D Rajapakse. “Wavelet-Based Artificial Neural Networks for Detection and Classification of DC Microgrid Faults” 2019 IEEE Power & Energy Society General Meeting (PESGM).
- [17] S. Kumar K, S. Shivakumara R and V. Venkatesh, “Artificial neural network based method for location and classification of faults on a transmission lines,” International Journal of Scientific and Research Publications, vol. 4, no. 6, pp. 1-6, June 2014.
- [18] Biswarup Das , J. Vittal Reddy “Fuzzy-Logic-Based Fault Classification Scheme for Digital Distance Protection” IEEE TRANSACTIONS ON POWER DELIVERY, VOL. 20, NO. 2, APRIL 2005.

Research on Grid-Connected/Islanded Control Strategy of PV and Battery Storage Systems as Emergency Power Supply of Pumping Storage Power Station

Zhaohui Kan, Zilong Li, Shuaixuan Li, Tong Zhang
 Hubei Bailianhe Pumped Storage Co., Ltd.
 Huanggang, China

Dang Zhu, Ming Yi, Yunhui Huang
 Wuhan University of Technology
 Wuhan, China
 e-mail: 1312869978@qq.com

Abstract—In order to solve the problem of the insufficient reliability of diesel engine as the emergency power supply of pumped storage power station, a grid-connected/islanded control strategy of PV and battery storage systems as the emergency power supply of pumped storage power station is proposed. To begin with, the control strategies of different operation modes of the optical storage system are introduced. In the grid-connected operation mode, PQ control strategy is used to coordinate the output of PV and battery storage to meet the station power load demand. When faults occur in the grid, the PV and battery storage systems switch to islanded operation mode. At this time, the battery storage system adopts V / F control to maintain the stability of system voltage and frequency. The PV system still uses PQ control, and the two coordinate to supply power for the load. The time domain simulation model of PV and battery storage systems is established and the control strategy of the converter is simulated. The simulation results verify the effectiveness of the proposed grid-connected/islanded control strategy.

Keywords—pumped storage power station; emergency power suppl; PV and battery storage systems; grid-connected/islanded control

I. INTRODUCTION

At present, the domestic pumped storage power stations which have been put into operation basically use diesel engine sets as emergency power supply for station power load. However, as the diesel engine is used as emergency power supply has the risks of off-line power supply, unsuccessful start-up, environmental pollution and later maintenance costs are higher. Therefore, in order to ensure the reliability and stability of the station power load for pumped storage power station, it is necessary to supplement safe, reliable, and low maintenance cost emergency power supply to ensure the stable operation of station power system [1]-[4].

With flexible control and mature technology, PV and battery storage systems is an important application direction of new energy generation technology. Literature [5] studies and discusses the emergency power supply of storage power stations, and statistically analyzes the current emergency power supply configuration of pumping power stations and the main influencing factors. Literature [6] studied the configuration scheme and operation mode of the standby diesel generator set for the safe and reliable operation of the

isolated network of the offshore wind farm. Literature [7]-[8] designed a coordinated operation control strategy for isolated micro-grid of Wind Power, PV System, Diesel Generator, and Battery Storage to ensure long-term stable operation of the isolated system.

This paper introduces a kind of PV and battery storage systems structure, and analyzes two control strategies of battery storage converter and their switching: constant power control, namely PQ control strategy; Constant voltage constant frequency control, that is V/f control strategy. In grid-connected mode, PV system and battery storage system adopt PQ control strategy to coordinate output and meet the station power load demand. In the islanded mode, the output power of the PV system is greatly affected by the environment and not controllable when generating power. PQ control is always adopted during the operation. In this case, the battery storage converter is controlled by V/f to provide stable voltage and frequency for the system, and can be switched according to the voltage and frequency of the grid.

II. SYSTEM STRUCTURE PRINCIPLE AND COORDINATED CONTROL STRATEGY

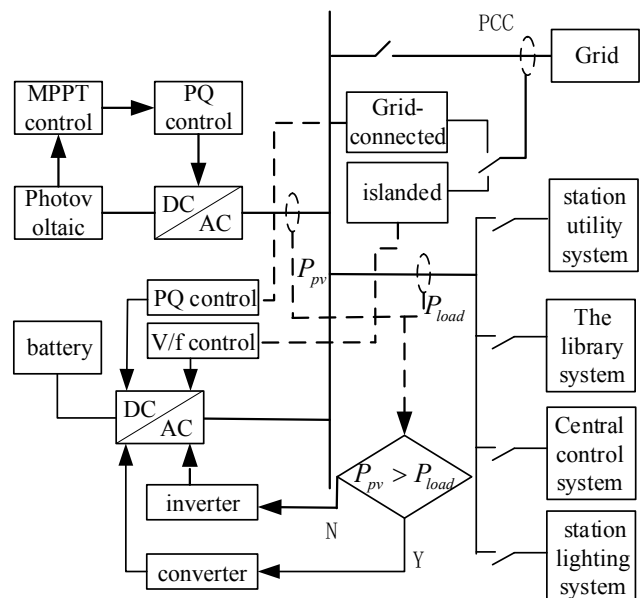


Figure 1. Overall structure of PV and battery storage systems.

The object of this paper is PV and battery storage systems, whose structure is shown in Fig. 1. The system consists of PV array, battery storage system, station power load, converter and grid. Among them, station power load includes station utility system, the library system, central control system, station lighting system, etc.

As can be seen from Fig. 1, in order to realize the coordinated operation of the PV and battery storage systems, the output power P_{pv} of the PV system and station power load P_{load} are detected. When $P_{\text{pv}} > P_{\text{load}}$ occurs, the station power load is all provided by the PV system, and the excess active power of the PV system is transferred to the battery storage system for charging. When $P_{\text{pv}} < P_{\text{load}}$, all the power of the PV system is transferred to the station power load, and the insufficient power demand is provided by the battery storage.

III. GRID-CONNECTED/ISLANDED CONTROL STRATEGY OF SYSTEM

A. Grid-Connected Control Strategy

The control structure of power outer loop and grid-connected current inner ring is adopted.

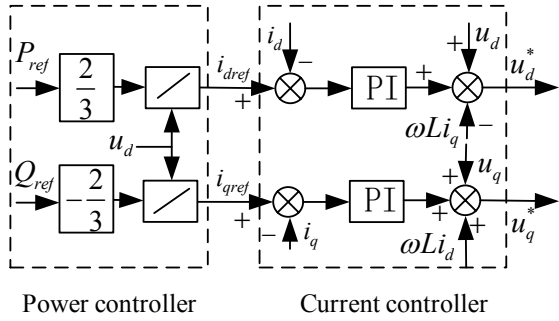


Figure 2. Grid-connected control strategy structure.

The power outer ring needs to collect the grid voltage U and grid current I in real time, and then get the instantaneous measured value of power through calculation. The difference between them and the given value P_{ref} and Q_{ref} is divided by u_{sd} to get the given value i_{dref} and i_{qref} of the current inner ring. Grid-connected power is obtained through dq coordinate transformation to obtain current i_d and i_q , which are different from i_{dref} and i_{qref} . Through PI link and feedforward decoupling link, the inverter is controlled. The voltage reference values u_d^* and u_q^* are obtained. After the inverse transformation of coordinates and the SPWM modulation module, the driving signal of IGBT can be obtained, so as to ensure that the inverter delivers power to the grid at a given power value.

B. Islanded Control Strategy

When PV and battery storage systems is islanded, the voltage and frequency in the PV and battery storage systems must be stable. Therefore, the battery storage converter is

controlled by V/f. The battery storage system is equivalent to a voltage source and outputs the given voltage and frequency through closed-loop control. V/f control adopts double closed loop structure of outer voltage loop and inner current loop.

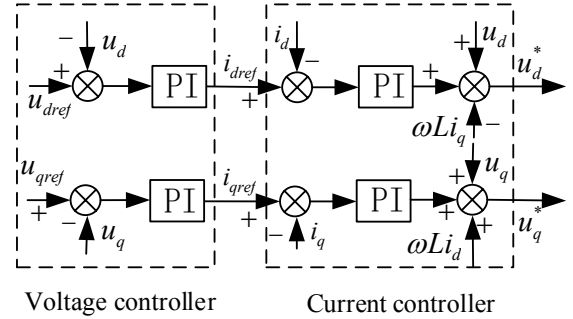


Figure 3. Control strategy structure.

Similar to PQ control, the reference voltage d-axis component u_{dref} is set as the base amplitude, and the q-axis component u_{qref} is set as 0. The differences between the u_d and u_q values obtained from the actual measured load side voltage through coordinate changes are adjusted by the PI controller to obtain the reference values i_{dref} and i_{qref} of the capacitance current axis d and q, respectively. Finally, the reference voltage components u_d^* and u_q^* in the internal axis coordinate system of the inverter are obtained through the PI controller and the feedforward decoupling link to realize the control of the inverter.

C. Grid-Connected/Islanded Switch Control Strategy

Since PV system always adopts PQ control in grid-connected operation and islanded, only the switch of battery storage system grid-connected/islanded control is considered.

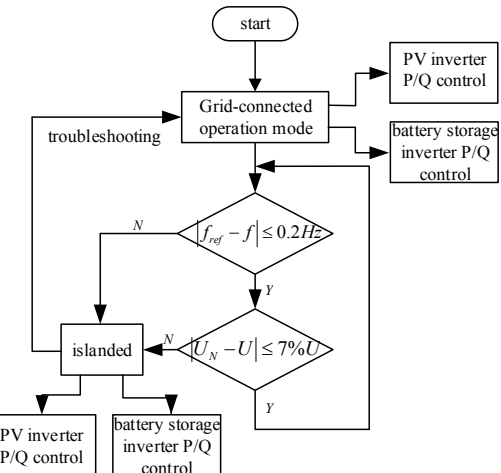


Figure 4. Grid-connected/islanded switching control flow.

According to the documents of GB/T12325-2008 "allows the power quality of power supply voltage deviation"

regulation, which is 10 kV and below power grid to allow the three-phase voltage deviation value is 7% of the rated voltage, frequency deviation should be allowed to meet GB/T15945-2008 "power quality of power system frequency deviation" regulation, allowing frequency deviation is 0.2 Hz, as the frequency of the detected lines or voltage exceeds the allowed range, system switch to islanded; When the fault is eliminated and the voltage frequency returns to the normal range, the PV and battery storage systems are reconnected to the grid.

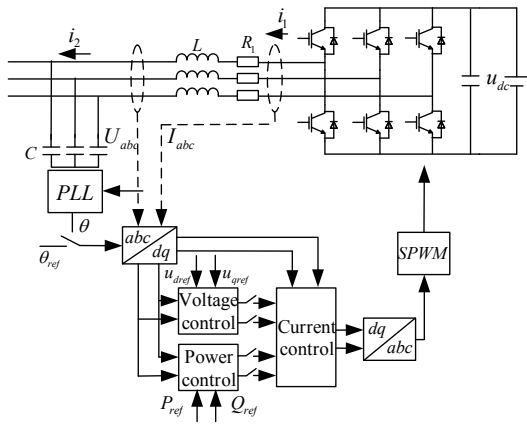


Figure 5. Grid-connected/islanded switching control strategy of the battery storage system.

As shown in the Fig. 5 above, during grid-connected operation, phase information required for coordinate transformation is provided by the PLL. Meanwhile, PQ control strategy of power control of the outer loop and current control of the inner loop is adopted. When a fault is detected in the grid, the frequency is switched to the given 50Hz to ensure the stable frequency of the system, and the corresponding power control of the outer loop is switched to the V/f control strategy of voltage control. The inner current loop does not need to be changed during the switching of the shunt.

IV. THE SIMULATION ANALYSIS

On the basis of theoretical analysis, the PV and battery storage systems are modeled, and Simulink simulation software is used to simulate the PV and battery storage systems as shown in Fig. 1.

A. Grid-Connected Control Strategy Simulation

The irradiance change of the PV array is set as shown in Fig. 6, the station power load is set to 50kW, and the output power of the PV system and battery storage system is changed as shown in the figure below.

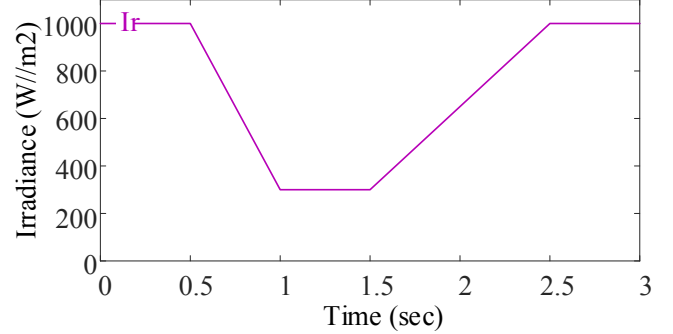


Figure 6. Irradiance changes of PV array.

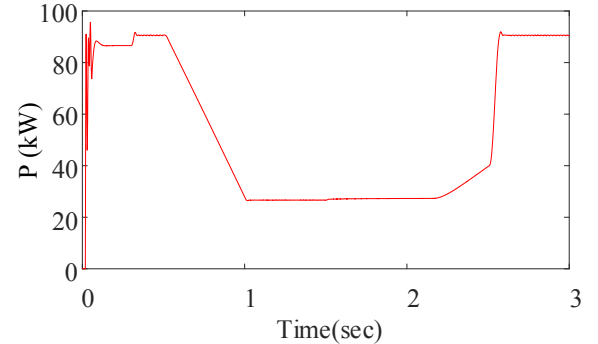


Figure 7. Active power change of PV system output.

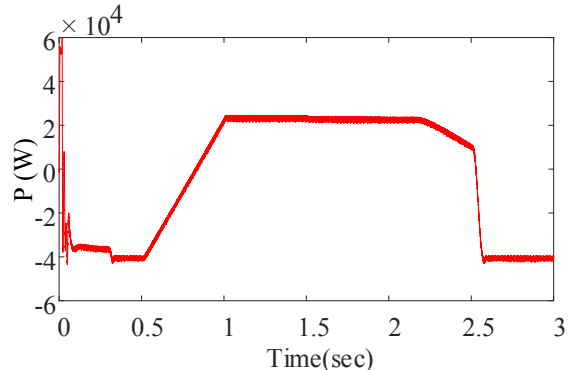


Figure 8. Active power change of battery storage system output.

The grid-connected current of PV inverter and battery storage converter is shown below.

It can be seen from Fig. 9-11 that the output current of PV inverter and battery storage converter changes with the change of irradiance, and both of them jointly maintain the stability of current at the grid point. Before 0.8s, the PV output power is greater than the station power load, the battery storage is charged. At 0.8s, the PV output power is less than the station power load, and the phase of the output current of the battery storage inverter is changed. The battery storage changing from charging state to discharge state to supply power to the load. It changed again around 2.5s.

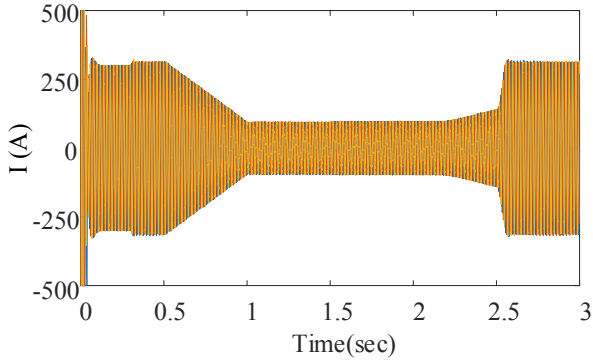


Figure 9. Output current of PV inverter.

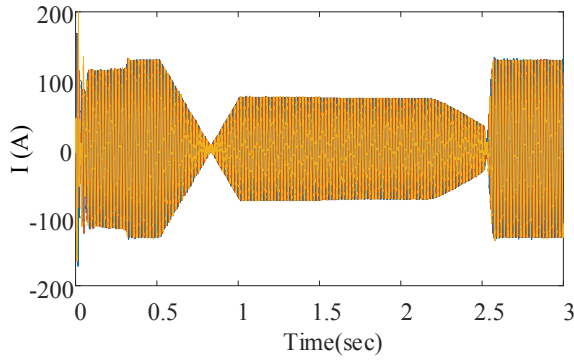


Figure 10. Output current of battery storage inverter.

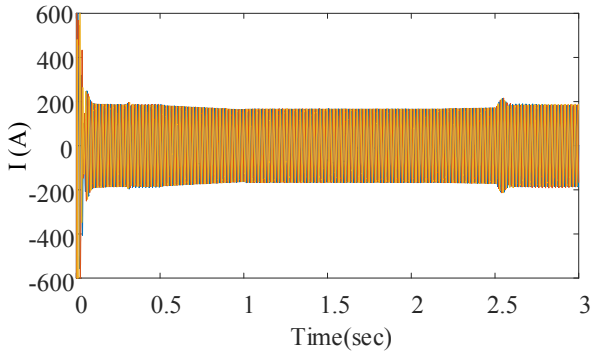


Figure 11. Junction current.

B. Islanded Control Strategy Simulation

Under the operation condition of the islanded, let the initial station power load be 120kw, cut out 60kW at 0.5s, cut-in 50kW at 1.5s, and the PV output is 100kW. At this point, the battery storage converter is controlled by V/f.

As can be seen from the Figs. 12-13, before 0.5s, the PV output was always lower than the station power load, so it was necessary to combine battery storage to supply power to the station power load. When the 60kW load is removed at 0.5s, the excess power will charge the battery storage when the PV output is greater than the station power load, corresponding to the part of the battery storage output curve in the Fig. below zero. At 1.5s, the load is cut-in 50kW, at which point the station power load is greater than the PV

output, and the battery storage changes from charging to discharging, which together with the PV power supplies the station power load.

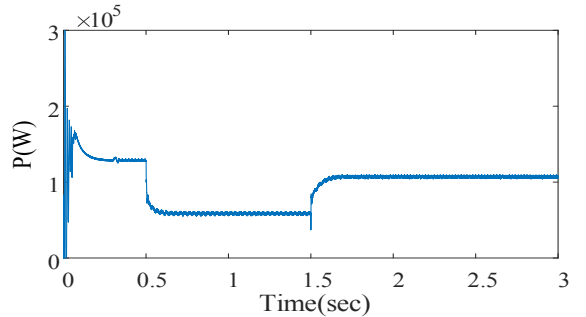


Figure 12. Active power change of the station power load.

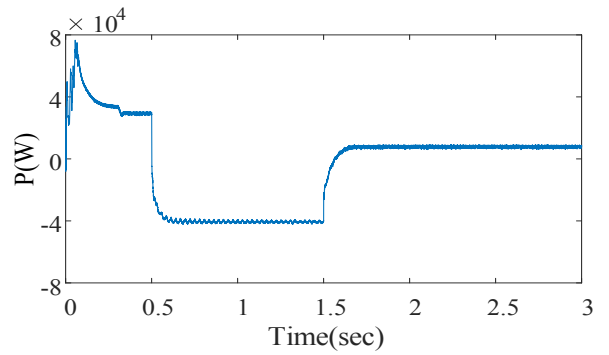


Figure 13. Active power change of battery storage system output.

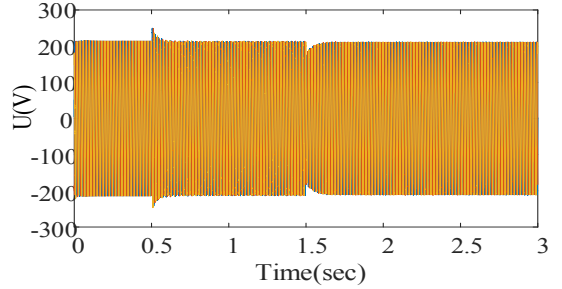


Figure 14. Three-phase voltage variation.

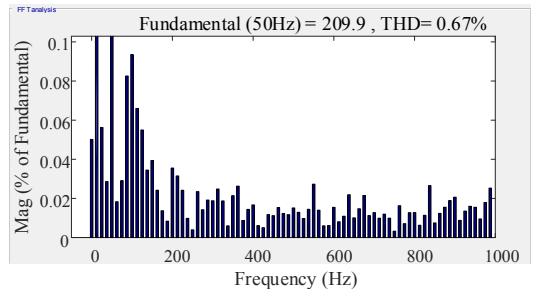


Figure 15. Voltage spectrum diagram.

Figs. 14-17 show the load voltage, current and spectrum diagram. It can be seen that the load voltage fluctuates when the load is cut-in and cut out, and then

quickly returns to stability. The load current decreases when the load is cut out, and increases when the load is cut in. The total harmonic distortion rate of voltage and current is 0.67%.

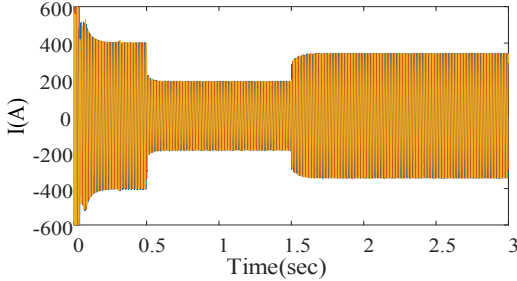


Figure 16. Change of three-phase current.

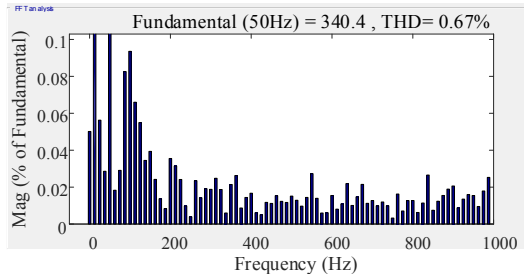


Figure 17. Current spectrum diagram.

C. Grid-Connected/Islanded Control Strategy Simulation

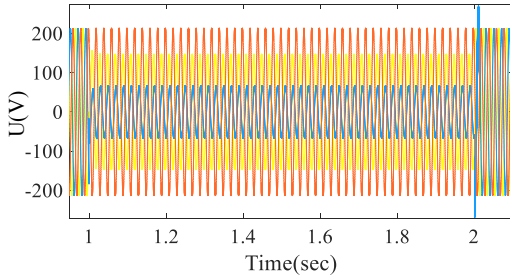


Figure 18. Voltage changes on the grid side.

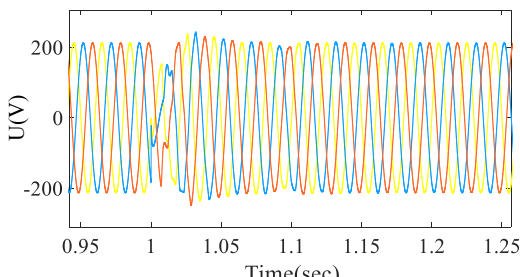


Figure 19. Load voltage variation.

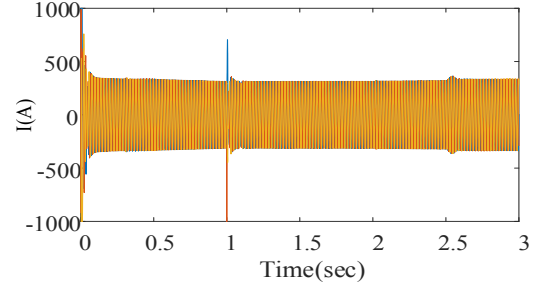


Figure 20. Load current variation.

Let the two-phase grounding short-circuit fault occur at the grid side at 1s, and the fault disappears at 2s, as shown in Fig. 18. The output power of the PV system is shown in Fig. 6, and the station power load is set to 100kW.

As can be seen from the Figs. 19-20, when the power grid fails, the optical storage system quickly switches to islanded. After 0.1s, the system runs stably in islanded. After the fault disappeared, the system switched to the grid-connected operation mode without obvious fluctuation.

V. CONCLUSION

In this paper, PV and battery storage systems is proposed as the emergency power supply of the pumping storage power station and grid-connected/islanded control strategy. Through simulation and analysis of the system voltage and power waveform under different operating modes, the following conclusions are drawn:

Under the grid-connected condition, the battery storage system can coordinate with the PV system to supply power to the station power load. Under the condition of islanded, the V/f control of the battery storage converter can provide stable voltage and frequency for the station power load.

When faults occur in the grid, the control strategy should be switched quickly to ensure the stable voltage of the pumping storage power station and the reliable operation of the station power load.

ACKNOWLEDGMENT

This work was supported by the Science and Technology Project of State Grid Xinyuan Company LTD. under Grant SGXY-2019F02-2-131.

REFERENCES

- [1] Q. Lu, W. Zhao, X. Huang. Preliminary discussion on comprehensive utilization of pumped storage power station [J]. *Hydropower and pumped storage*, 2017, 3(06): 58-62.
- [2] Z. Huang. Function research of pumped storage power station [J]. *Modern industrial economy and informatization*, 2018, 8(13): 96-98.
- [3] K. Wang, Z. Li, C. Bai, H. Zhou, et al. Study on price mechanism and market bidding model of pumped storage power station [J]. *Smart power*, 2019, 47(06): 47-55.
- [4] Y. Huang, X. Yuan, J. Hu, P. Zhou. Modeling of VSC connected to weak grid for stability analysis of DC-link voltage control[J]. *IEEE Journal of Emerging and Selected Topics in Power Electronics*, 2015, 3 (4) : 1193-1204.
- [5] J. Li. The Design and Analysis on the Emergency Power Supply Configuration of Pumped Storage Power Plant [J]. *Hydropower and pumped storage*, 2016,2(01):97-102.

- [6] M. Zheng, Y. Yang, Y. Shen, X. Xu, Y. Tao. Research on the Standby Diesel Generator Set Scheme of Offshore Wind Farm in the State of Island Operation Mode [J]. *Southern energy construction*, 2019, 6(01):24-30.
- [7] M. Liu, L. Guo, C. Wang, et al. A Coordinated Operating Control Strategy for Hybrid Isolated Microgrid Including Wind Power, Photovoltaic System, Diesel Generator, and Battery Storage [J]. *Power system automation*, 2012, 36(15): 19-24
- [8] Q. Wang, J. Sun, Y. Tang. Research on intelligent control strategy of wind-wind-firewood storage combined power generation system [J]. *Journal of electrical applications*, 2012, 31(24): 96-100.

Short Circuit Fault Localization Method Based on Improved OLS-RBF Neural Network Algorithm for AC Microgrids

Yibiao Huang
State Grid Fuzhou Electric Power Supply Company
 Fuzhou, China
 huangyibiao@126.com

Longyang Zhu
State Grid Fuzhou Electric Power Supply Company
 Fuzhou, China
 2239042194@qq.com

Yifan Wang
State Grid Fuzhou Electric Power Supply Company
 Fuzhou, China
 wyf688642@163.com

Hang Cheng
Fujian Rongneng Electric Power Group
 Fuzhou, China
 ch_7508@163.com

Yunting Shao
State Grid Fuzhou Electric Power Supply Company
 Fuzhou, China
 790034965@qq.com

Xin Zheng
College of Electrical Engineering and Automation
 Fuzhou University
 Fuzhou, China
 27480389@qq.com

Abstract—In order to improve the accuracy of short-circuit fault location in microgrids, this paper proposed a short-circuit fault location method for AC microgrids based on the improved OLS-RBF neural network algorithm. On the basis of amplifying microgrid short-circuit fault current signal using wavelet energy spectrum algorithm, the relationship between short-circuit current wavelet energy spectrum value and fault distance is investigated, and based on the European standard 400V low-voltage microgrid model, a coupling formula for fault location is constructed. Thus, a common fault area location model is established for both grid-connected and islanded modes. In the simulation experiments, the effect of transition resistance is taken into account to verify the accuracy of the method under different topological models.

Keywords— *microgrid, short circuit fault, neural network, fault location.*

I. INTRODUCTION

As nonrenewable energy sources deplete and traditional energy generation burdens the environment, China urgently needs to adopt a new technological and industrial revolution to replace its previous development model with a more scientific and sustainable one. This has led to the emergence of the smart grid concept [1]. Wind and photovoltaic power, as representatives of distributed energy, are promoted for their environmental benefits, integrating into traditional power distribution systems as microgrids and transforming their structure. However, microgrids experience rapid inrush current during faults, complicating data protection and affecting AC protection accuracy. Thus, accurately diagnosing and locating faults during short circuits is a key research area in microgrids.

Recent studies on microgrid fault diagnosis have highlighted the integration of digital signal processing and neural networks. Literature [2] combines wavelet singular entropy with a self-organizing feature mapping neural network for accurate classification of changes in microgrid systems

within one sampling period. However, its adaptability is limited and the model training process is complex. Literature [3] uses a great overlap discrete wavelet transform and back propagation neural network to quickly and accurately identify fault types, considering initial phase angle and transition resistances, but does not detail fault location. Literature [4] proposed a microgrid fault location method based on ARM model, which has a high quality of single-target fault location and little geographic coordinate error. However, it needs the signal support of the communication network, and visualization elements in the nonnetworked state are relatively few in number with a large deviation value. Literature [5] utilizes high-scale wavelet energy spectrum decomposition with the OLS-RBF neural network for early detection and regional location of short-circuit faults in microgrids. However, insufficient sampling capacity may lead to overfitting. Moreover, OLS-RBF neural networks are not universal and require frequent parameter adjustments due to changes in the training set, which leads to a complicated training process.

The proposed method in this paper is based on the literature [5], and then improves the OLS-RBF neural network algorithm by introducing the gradient descent operator, so that each centroid has an independent centroid width. This improves the generalization performance of the algorithm. The model tuning process is simplified to adapt the neural network model to microgrid models with different topologies on the basis of ensuring the rapidity and accuracy of fault localization.

II. MICROGRID SHORT CIRCUIT FAULT ANALYSIS

A. Modeling of 400V Low Voltage Microgrids

Referring to the European 400V standard low-voltage microgrid structure [6], a simulation model is established by MATLAB/SIMULINK, as shown in Fig. 1. The distributed power in the model consists of energy storage battery, photovoltaic battery, and wind turbine, in which the energy storage battery is VF controlled and the rest of the distributed

power is PQ controlled. The power factors of the loads are all 0.85, the operating frequency of the microgrid model is 50 Hz, and the total length of the line is 600m.

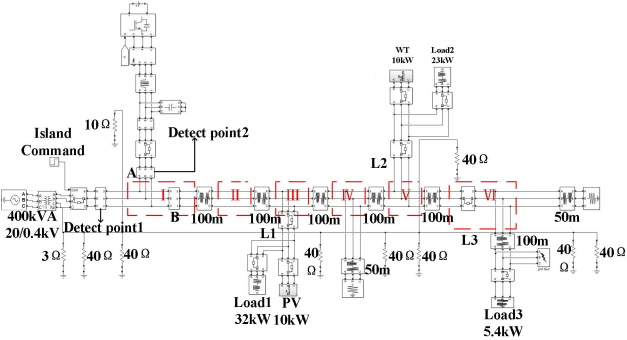


Fig. 1. Topology of 400V standard LV microgrid in Europe

B. Failure Analysis

The wavelet energy spectrum transform is a mathematical tool based on the Fourier transform, capable of effectively identifying and extracting subtle features within signals. At the same time, the multi-scale wavelet decomposition algorithm itself functions as a digital filter, efficiently suppressing noise interference in low-voltage systems [7]. In this paper, the derivative of the cubic B-spline function is chosen as the wavelet function, according to Mallat's algorithm [8], the wavelet energy spectrum transform equation for the discrete signal $f(x)$ in the time domain is shown in (1).

In Equation(1), i represents the scale of wavelet decomposition, $S_{2^i}f(x)$ and $W_{2^i}f(x)$ are the smooth component and detail component at the i -th scale of wavelet decomposition, respectively, and $E_{2^i}f(x)$ is the energy of the details at the i -th scale. As i increases, the singularity of the fault signal is enhanced. However, as i increases, the computation speed decreases. Taking all factors into account, this paper selects the wavelet decomposition transform at the fourth scale. The impulse response coefficients of the low-pass filter h_k and the band-pass filter g_k are provided in Table I.

Based on Table I and Equation (1), the equations can be derived, where Equations (2) and (3) represent the smooth component at the third scale and the detail component at the fourth scale, respectively, and Equation (4) is the mathematical model of the wavelet energy spectrum used in this paper.

The wavelet energy spectrum algorithm is modeled in Simulink using existing components, as shown in Figure 2.

Wavelet transform can effectively extract local signal features, and the wavelet energy spectrum is based on the binary wavelet transform, which squares and amplifies the detailed components of the signal to improve the recognition of abrupt features of weak signals. In this paper, the first peak value of the wavelet energy spectrum, $E4_{max1}$, is obtained after a short-circuit fault occurs in AC microgrid by using wavelet energy spectrum algorithm, which amplifies the fault current signal during the short-circuit fault. Then, the relationship between $E4_{max1}$ and the fault distance d is analyzed.

$$\begin{cases} S_{2^i}f(x) = \sum_k h_k S_{2^{i-1}}f(x - 2^{i-1}k) \\ W_{2^i}f(x) = \sum_k g_k S_{2^{i-1}}f(x - 2^{i-1}k) \\ E_{2^i}f(x) = |W_{2^i}f(x)|^2 \end{cases} \quad (1)$$

TABLE I. THE COEFFICIENTS h_k AND g_k

k	-1	0	1	2
h_k	0.125	0.375	0.375	0.125
g_k	0	-2	2	0

$$\begin{aligned} S_{2^1}f(n) &= \frac{1}{8}S_{2^0}f(n+1) + \frac{3}{8}S_{2^0}f(n) + \frac{3}{8}S_{2^0}f(n-1) + \frac{1}{8}S_{2^0}f(n-2) \\ S_{2^2}f(n) &= \frac{1}{8}S_{2^1}f(n+2) + \frac{3}{8}S_{2^1}f(n) + \frac{3}{8}S_{2^1}f(n-2) + \frac{1}{8}S_{2^1}f(n-4) \\ S_{2^3}f(n) &= \frac{1}{8}S_{2^2}f(n+4) + \frac{3}{8}S_{2^2}f(n) + \frac{3}{8}S_{2^2}f(n-4) + \frac{1}{8}S_{2^2}f(n-8) \end{aligned} \quad (2)$$

$$W_{2^4}f(n) = 2(S_{2^3}f(n-8) - S_{2^3}f(n)) \quad (3)$$

$$E_{2^4}f(x) = |W_{2^4}f(x)|^2 \quad (4)$$

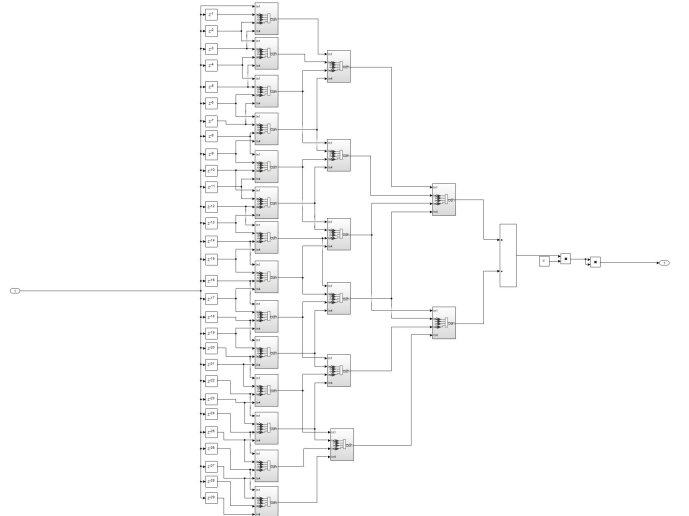


Fig. 2. The model of the wavelet energy spectrum algorithm

Previous research has shown that [9] when the distance d from the short-circuit fault point to the detection point increases, $E4_{max1}$ will decrease. Considering the actual value of $E4_{max1}$ is relatively large, we define the parameter $E4_{max1} = K_e/E4_{max1}$ where K_e takes the value of 10^6 . Fig. 3 shows the relationship between d and $E4_{max1}$ for single-phase grounded short circuits under different values of θ_c .

As we can see from Fig. 3, $E4'_{max1}$ increases with the increase of d for different θ_c . After the simulation study, it is found that the conclusion is always consistent with the above for different capacity cases, different transition resistor resistance values and different short-circuit fault types [10]. Therefore, considering different factors, the value of the fault current measured at the detection point can approximately reflect the distance d from the short-circuit fault point to the detection point, thus realizing the regional localization of the short-circuit fault.

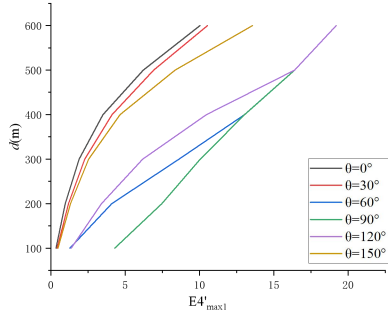


Fig. 3. Relationship between d and $E4'max1$ for different θ_c

III. FAULT LOCATION ANALYSIS BASED ON NEURAL NETWORK

A. Principle of OLS-RBF Neural Network Algorithm

As shown in Fig. 4, the radial basis function neural network consists of three layers of neurons: the input layer, the hidden layer and the output layer, which theoretically has the ability to approximate any nonlinear function. Among them, the input layer receives training data, the sample capacity is n ; the implicit layer transforms the low-dimensional linearly indivisible problem of the input layer into a high-dimensional space with the help of a radial basis function so as to realize a linearly differentiable. The radial basis function is usually selected Gaussian function, the mapping relationship as shown in (5). As the sample point is closer to the center point, the implicit layer output is higher. The output layer is connected to the implicit layer by linear weights, as shown in (6). In Equation (6), y represents the actual value, and \hat{y} represents the predicted value. From (5) and (6), the radial basis function center point c_i , width σ_i and output weights λ_i affect the accuracy of the neural network model together.

The OLS-RBF neural network selects the center points of the radial basis function by orthogonal least squares, and determines the contribution of each sampling point to the reduction of the output error, so as to minimize the overall error until it meets the set requirements. Compared with the K-means clustering method, the OLS-RBF neural network does not need to preset the center points, and the order of contribution is fixed when the sampling points are determined, i.e., the accuracy of the model is only related to the number of center points in the hidden layer. The flow of the algorithm is shown in Fig. 5 [11].

After the above process, a radial basis function neural network model based on orthogonal least squares can finally be obtained. It can be found that when the sampling points and their corresponding truth values are unchanged, the center point selection is unchanged, and there are no random events in the model construction process. However, if the capacity of the sampling points is small, it may lead to all the sampling points being selected as the center point, overfitting occurs, and the expected fitting accuracy cannot be achieved. In addition, the OLS-RBF neural network is not universal, and whenever the training set is changed, the width of the center point in the program needs to be constantly modified, and the training process is more complicated.

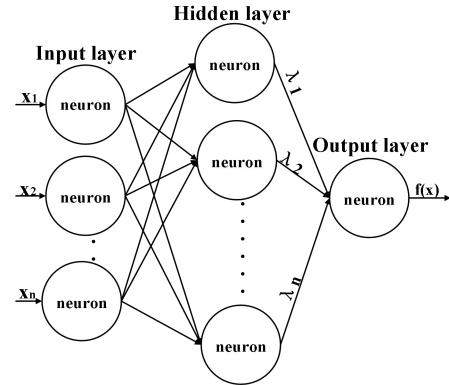


Fig. 4. Schematic diagram of RBF neural network

$$\phi(\|x - c_i\|) = \exp\left(-\frac{\|x - c_i\|}{2\sigma_i^2}\right) \quad (5)$$

$$y = \hat{y} + \varepsilon = \sum_{i=1}^n \lambda_i \phi_i(\|x - c_i\|) + \varepsilon \quad (6)$$

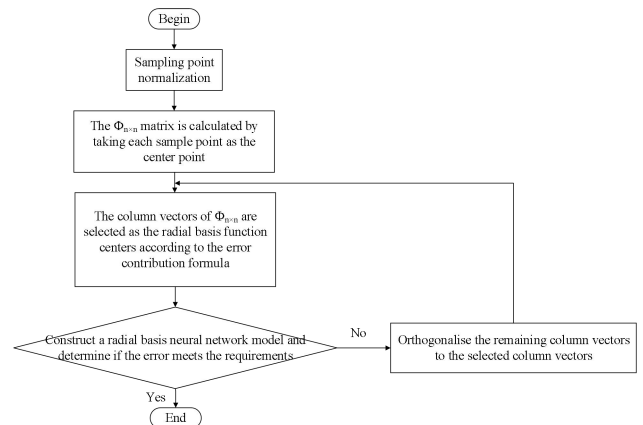


Fig. 5. Flowchart of OLS-RBF neural network model

B. Improved OLS-RBF Neural Network Algorithm

In order to reduce the number of neurons in the hidden layer of the OLS-RBF neural network and to improve the generalization ability of the algorithm, a gradient descent operator is introduced into the original OLS-RBF neural network so that each centroid has an independent centroid width σ_i . The structure of the improved OLS-RBF neural network algorithm is shown in Fig. 6.

The principle of the gradient descent operator is as follows: each radial basis function center point initially has a width value σ . To optimize the model, the width of each center point needs to be adjusted to minimize the output error. First, the root mean square error (rmse) under the current conditions is calculated using Equation (7), representing the error between the model output and the true value. The goal of the gradient descent method is to gradually adjust the center point width σ to reduce this error.

The gradient descent method uses the gradient of the error to adjust the width. The update equation for the center point width is shown in Equation (8). In Equation (8), σ^* is the updated width, and ω is the learning rate. This value can be

set relatively large in the initial phase of the program to widen the search range for σ . When the difference between σ^* and σ becomes small, the learning rate should be reduced to a very small value. $\Delta\sigma$ is the change in the center point width, and its calculation equation is shown in Equation (9).

If $\Delta\sigma > 0$, it indicates that the current adjustment direction of the width σ helps reduce the error, and the adjustment should continue in the current direction to approach the optimal value. If the gradient change is small, it indicates that the width adjustment is stabilizing, and the learning rate ω should be reduced to more precisely find the minimum error.

When the difference in the error becomes sufficiently small or the maximum number of iterations is reached, the gradient descent process ends, and the optimal width value for each basis function is obtained.[11]

For a single-phase grounded short-circuit fault, set the range of DG capacity of the built simulation model as 10-60kW, with sample points at $S_{DG} \in \{10, 20, 30, 40, 50, 60\}$. Due to the symmetry of the fault occurrence, only half a cycle need to be analyzed, with initial phase angles $\theta_c \in \{0, 30, 60, 90, 120, 150\}$. The short-circuit point transition resistance is $R_g \in \{0.01, 0.05, 0.1, 0.5, 1\}$, and the fault distance is set as $d \in \{100, 200, 300, 400, 500, 600\}$. This results in a total of 1,080 data sets, with 80% used for training and 20% for testing. Figure 7 illustrates the modeling process of various neural networks for the objective function d , showing that the improved OLS-RBF neural network requires fewer implicit layers to converge and takes less time during debugging.

The trained radial basis function centroid c_i , output weights λ_i and centroid width σ_i are substituted into (6) to obtain the functional relationship between the fault distance d and $S_{DG}, \theta_c, R_g, E'_{max1}$ as in (10). Fig. 8 shows the prediction accuracy of the two neural network models for the test set in the grid-connected, where the pre-improved R^2 is 97.56% and the improved R^2 can reach 98.99%.

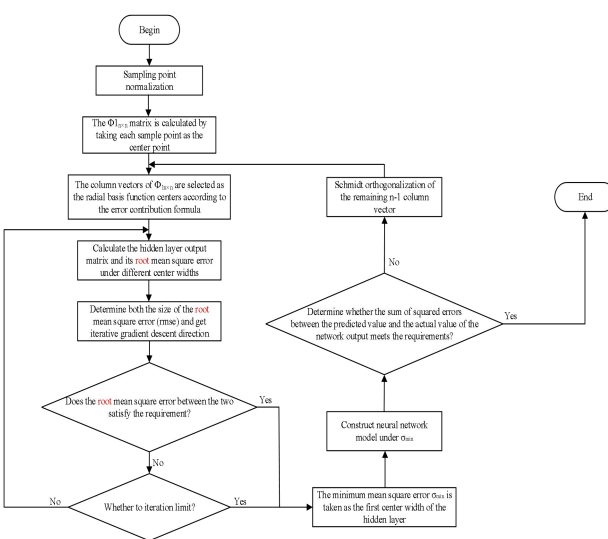


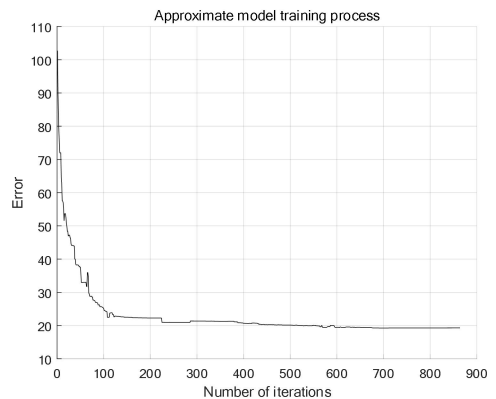
Fig. 6. Flowchart of OLS-RBF neural network model

$$\delta_{RMSE} = \sqrt{\|y - \phi_n \lambda\|^2 / n} \quad (7)$$

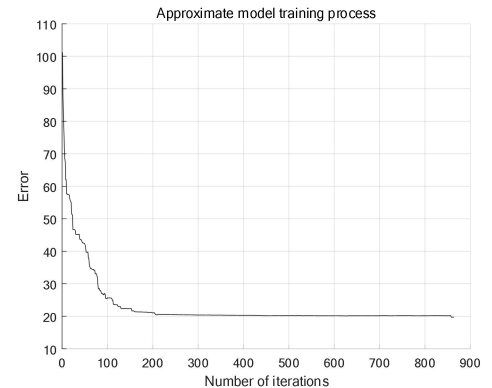
$$\sigma^* = \sigma - \omega \Delta \sigma \quad (8)$$

$$\Delta \sigma = (\delta_{RMSE1} - \delta_{RMSE2}) / (\sigma^* - \sigma) \quad (9)$$

$$d = \sum_{i=1}^{864} \lambda_i \exp \left(-\frac{\sqrt{(S_{DG} - c_i)^2 + (\theta_c - c_i)^2 + (E'_{max1} - c_i)^2 + (R_g - c_i)^2}}{2\sigma^2} \right) \quad (10)$$

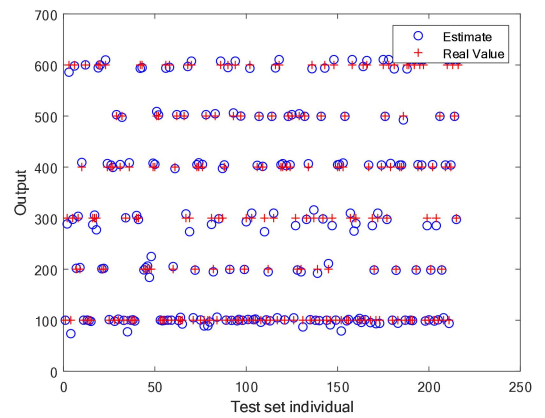


(a) OLS-RBF neural network

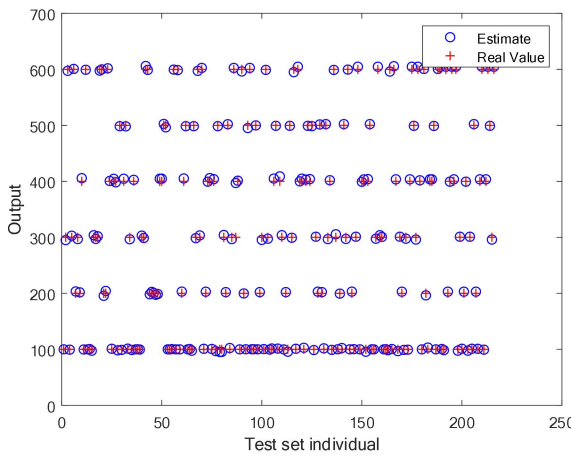


(b) Improved OLS-RBF neural network

Fig. 7. Approximate modeling process of different neural networks for the objective function d



(a) OLS-RBF neural network



(b) Improved OLS-RBF neural network

Fig. 8. Fault location prediction accuracy map in grid-connected operation mode

IV. SIMULATION VERIFICATION

A. Initial Phase Angle of Fault θ_c Determination and Short Circuit Fault Type Identification

From Fig. 3 and (10), it can be seen that it is necessary to determine the initial phase angle θ_c of the fault and determine the fault type before fault region localization by $E4'_{max1}$. When $E4$ reaches the detection threshold X_d , the system gets the preliminary fault initial phase angle detection value θ and the calculation formula is shown in (11).

$$\theta = K_j \times S_t \times 10^{-4} \times 180^\circ \quad (11)$$

where S_t denotes the simulation step size in Simulink, which is set to 50us in this paper according to the accuracy requirement; K_j is the number of times the fault initial phase angle detection module runs. Since the wavelet energy spectrum characteristics are the same when the fault occurs in the positive and negative half-waves, this parameter is reset when the current is at the point of crossing the zero point. As there is an interval Δt between the detection of the fault occurrence and the actual occurrence of the fault, the detection value θ needs to be processed as shown in Equation (12) to obtain a more accurate initial phase angle of the fault θ_c . Figure 9 shows the detection model of the initial phase angle of the fault θ_c .

$$\theta_c = \theta - \Delta\theta \quad (12)$$

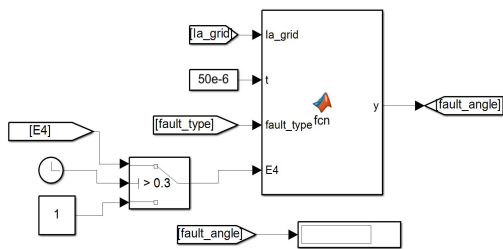


Fig. 9. Initial phase angle of fault θ_c Detection model

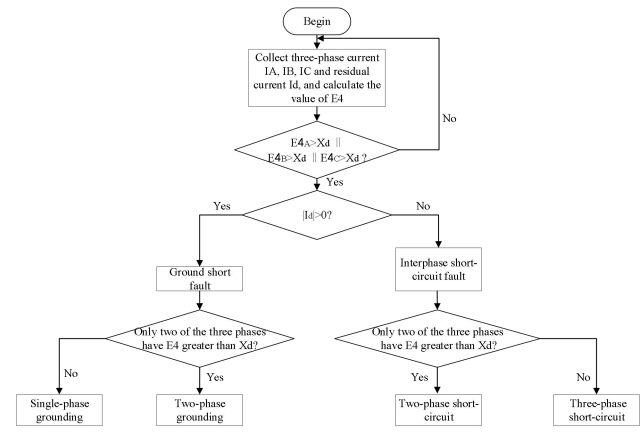


Fig. 10. Block diagram of short-circuit fault type judgment program

Figure 10 shows the short circuit fault type judgment process. Since the microgrid model established in this paper is a three-phase four wire system, the residual current can be used to determine whether the short circuit fault is grounded, and then the faulted phases and the fault type can be determined based on whether the $E4$ values of the currents in each of the phases of \dot{I}_a , \dot{I}_b , and \dot{I}_c exceed the threshold values.

B. Simulation Modeling

According to the above analysis of the principle of fault area localization, design the area localization simulation model, as shown in Fig. 11. The realization steps are as follows:

1) Based on the early detection thresholds X_d set earlier, when the measured $E4$ value is greater than X_d , the fault is judged to have occurred;

2) Determine whether current is passing through the grid-connected point;

3) Detect the initial phase angle of the fault θ_c ;

4) Identify the type of fault;

5) Detect the maximum $E4$ value within 1ms as $E4_{max1}$ and calculate $E4'_{max1}$;

6) Calculate the fault distance d by substituting the initial fault phase angle θ_c , $E4'_{max1}$, and the S_{DG} and R_g set by the system into the fault area location equation for the fault type, then determine the fault area.

C. Simulation results and analysis

The simulation verification data for different short-circuit fault types are shown in Table II, where t_1 denotes the early detection time, and t_2 denotes the total time from early detection to fault location for short-circuit faults. From the data in the table, it can be seen that the protection system is able to realize the early detection of the fault within 1ms, and accurately identify the fault type and complete the fault location within 2ms. The fault settings are distributed across six regions in Figure 1, and the measurement results are consistent with the area where the fault point is located.

The proposed method has been compared with the traveling wave distance measurement method from literature [12] at different fault distances and the results are listed in Table III. It can be seen from the table that the method proposed in this

paper has a significant advantage in terms of positioning accuracy.

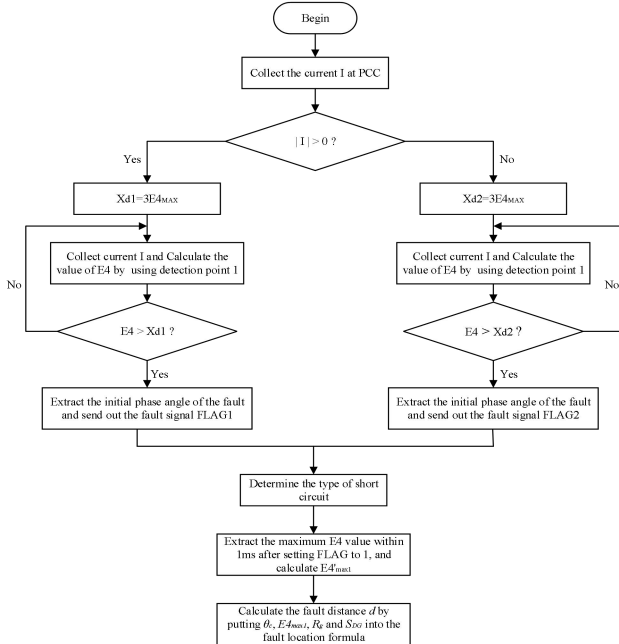


Fig. 11. Protection system operation flow

V. CONCLUSION

In summary, this paper proposes a fault location method which is based on improved OLS-RBF neural network algorithm on the ground of using wavelet energy spectrum algorithm to amplify the fault current, while satisfying the requirements of quickness and accuracy of fault area location, it reduces the complexity of the network model, simplifies the model training process, and enhances the generalizability of the proposed method. In addition, a generalized fault area localization model is established for both grid-connected and islanded modes.

TABLE II. SHORT-CIRCUIT FAULT PROTECTION SIMULATION VERIFICATION RESULTS

Type & Distance of fault (d/m)	running mode	$S_{dc}(kW)$	$\theta_c(^{\circ})$	t_1	t_2	Localization results of fault area
AG (268)	isolated island	43	136	0.363	1.384	Region III
AG (427)	grid connection	41	177	0.490	1.523	Region V
AG (508)	grid connection	38	131	0.362	1.387	Region VI
AG (63)	isolated island	42	173	0.453	1.574	Region I
ABG (589)	grid connection	26	105	0.268	1.620	Region VI
ABG (212)	isolated island	39	50	0.336	1.650	Region III
ABG (109)	isolated island	10	4	0.465	1.718	Region II
ABG (336)	grid connection	28	121	0.441	1.469	Region IV
AB (498)	isolated island	37	81	0.269	1.792	Region V
AB (560)	grid connection	59	76	0.563	1.887	Region VI
AB (446)	isolated island	12	151	0.245	1.597	Region V
ABC (600)	isolated island	55	139	0.562	1.704	Region VI
ABC (358)	grid connection	17	66	0.446	1.767	Region IV

TABLE III. FAULT LOCATION PERFORMANCE COMPARISON OF DIFFERENT PROTECTION METHODS

fault localization method	fault distance (m)	localization result (m)	relative error (%)
the method described in this paper	820	826	0.7
Traveling wave distance measurement method	880	889	1.0
Traveling wave distance measurement method	820	1040	26.8
Traveling wave distance measurement method	880	1040	18.2

ACKNOWLEDGMENT

This work is financially supported by “Technology Project of State Grid Fujian Electric Power Co., Ltd.” (No. 521310240008).

REFERENCES

- [1] Zeng Ming, Yang Yongqi and Liu Dunnan ,et al, " Generation-Grid-Load-Storage" Coordinative Optimal Operation Mode of Energy Internet and Key Technologies " , *Power System Technology*,vol.40,no.1,pp.114-124, January 2016.
- [2] Qiu Lu, Ye Yinzong and Jiang Chundi, "Fault diagnostic method for micro-grid based on wavelet singularity entropy and SOM neural network", *Journal of Shandong University(Engineering Science)*, vol. 47, no. 5, pp. 118-122+129, October 2017.
- [3] Chen Jiahui , Gao Yanjie , Jin Yiwei, " A New Microgrid Fault Diagnosis Method Based on MODWT and BP Neural Network ", *Journal of Shanghai University of Electric Power*,Vol.37,no.1,pp.57-60+77, February 2021.
- [4] Zeng Yihui , Shu Yingjun , Mai Junjia , Li Bin , Wu Xinqiao, "A Beidou Fault Location Method for AC Microgrids Based on Arm Model " , *Power System and Clean Energy*,Vol.39,no.4,pp.99-104,April,2023.
- [5] Zheng Xin and Gan Honghao, "Early Detection and Regional Location of Short Circuit Fault for Grid-connected AC Microgrid with Different Capacity ", *Proceedings of the CSEE*,vol. 44, no. 11, pp. 4353-4367, 2024.Available: <http://kns.cnki.net/kcms/detail/11.2107.tm.20230308.0921.012.html>.
- [6] PAPATHANASSIOU S, HATZIARGYRIOU N, STRUNZ K, " A benchmark low voltage microgrid network ", Proceedings of CIGRE Symposium: *Power Systems with Dispersed Generation*, Athens, Greece, pp. 1-8, April 2005.
- [7] Chen Li'an and Zhang Peiming, "Early Detection of Short Circuit Faults in Low Voltage Systems Based on Morphological Wavelets," *China Electric Power Research Institute*, vol. 10, no. 1, pp. 24-28+88, May 2005.
- [8] S. Mallat and S. Zhong, "Characterization of signals from multiscale edges," *IEEE Transactions on Pattern Analysis and Machine Intelligence*, vol. 14, no. 7, pp. 710-732, July 1992.
- [9] Zeng Yue,"Design and Implementation of Short-Circuit Fault Protection System in Grid-Connected AC Microgrid ",Fuzhou University,April 2022.
- [10] Zhou Yanfang, Wang Ying, Huang Tao, Mao Weijun and Hu Zhesheng, " Research on influence of transition resistance on microgrid fault detection", *Modern Electronics Technique*, vol. 45, no. 17, pp. 157-162, September 2022.
- [11] Zhao Fumin, " Research on multi-objective optimization method of electromagnetic actuator with permanent magnet " , Fuzhou University,April 2022.
- [12] Dai Feng, Wang Zheng, Cheng Menghan, et al, "Study on fault location considering refraction and reflection of short lines in a distribution network," *Power System Protection and Control*, vol. 48, no. 16, pp. 122-130, 2020.

Simulation Analysis of Fault Crossing of Three-phase Energy Storage System

Xuebin Wang

Guobin Fu

Guoqiang Lu

Electric Power Research Institute

Electric Power Research Institute

Electric Power Research Institute

State Grid Qinghai Electric Power Company

State Grid Qinghai Electric Power Company

State Grid Qinghai Electric Power Company

Qinghai, China

Qinghai, China

Qinghai, China

519957075@qq.com

fgbin0814@163.com

lgqiang2015@163.com

Haibin Sun

Kaixuan Yang

Electric Power Research Institute

Electric Power Research Institute

State Grid Qinghai Electric Power Company

State Grid Qinghai Electric Power Company

Qinghai, China

Qinghai, China

1601427954@qq.com

806867060@qq.com

Abstract—The proposed goal of "double carbon" in China has attracted much attention from new energy generation. However, the new energy generation has intermittency, volatility and other characteristics to the stability of the grid has brought a certain challenge. Therefore, many new energy distribution and storage schemes have been introduced, so the stable operation of the energy storage system after grid connection is particularly critical. Based on the time domain simulation of PSCAD/EMTDC three-phase energy storage system, this paper studies whether the system has the ability of stable fault crossing during the fault period.

Keywords—Three-phase energy storage, Grid-connected converters, PQ double closed loop control, Fault traverse control

I. MODELING REQUIREMENTS FOR THREE-PHASE ENERGY STORAGE SYSTEM

The three-phase energy storage system is generally first connected to the DC bus through Buck-Boost circuit [1], and then connected to the AC power grid through the power converter system and filter circuit. Its structure is shown in Figure 1. The DC-DC circuit is used to maintain the voltage stability of the DC bus. The converter adopts the vector control strategy based on the rotating dq coordinate system to ensure that the system has the ability of power frequency active power and reactive power regulation. The filter circuit is used to filter the harmonics generated by power electronic devices to ensure that the output voltage and current meet the requirements of grid-connected harmonics.

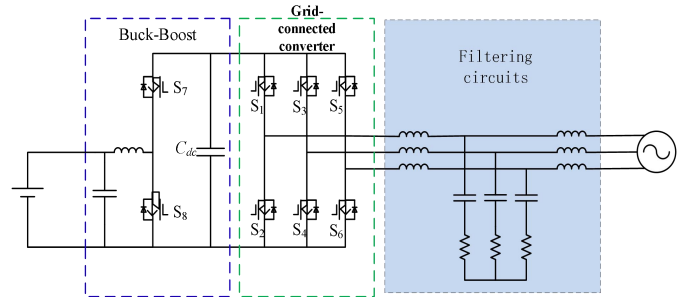


Fig. 1. Three-phase energy storage system

The Technical Regulations for Electrochemical Energy Storage System Access to the Power Grid [2] put forward specific requirements for the fault crossing capability of the lithium-ion energy storage system, that is, the system should run continuously without off-grid at a specific voltage drop/rise depth, and inject capacitive/inductive reactive current into the power grid to support voltage recovery when necessary. When the system fails, the control is put into the fault crossing control link, and the working mode is switched to reactive power priority mode [3].

A. Grid-connected converter control mode

There are many kinds of control methods of grid-connected converters in engineering, and there are great differences in working principles. In order to analyze the operation condition of the three-phase energy storage system after grid-connection, this paper adopts the most commonly used PQ double closed-loop control strategy, calculates the reference value of the D-axis current and the Q-axis current according to the active

power and reactive power instructions, and then realizes the power control by PI control of the current. We build the PQ control model according to the above ideas. As shown in Figure 2, in this control strategy, the function of the PLL is to detect the direction of the voltage vector at the junction point, so as to provide a phase reference for the decomposition of the electrical quantity dq in the entire control system. Figure 2 is a logical diagram of the PQ control relationship.

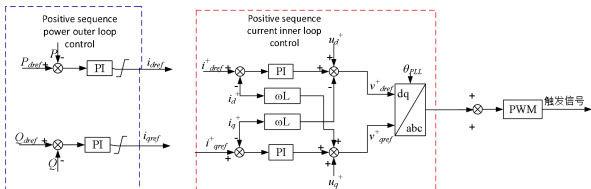


Fig. 2. PQ double closed loop control logic diagram

Where, P (Q) and P_{ref} (Q_{ref}) are the measured value and reference value of active (reactive) power respectively; u_d (i_d), u_q (i_q) and D-axis and Q-axis components of positive sequence voltage (current) respectively; i_dref , i_qref positive sequence power outer loop, fault crossing control output current reference value; θ_{PLL} is the output phase Angle of the phase locked loop (PLL). PI is the proportional-integral link; ω_L is the reactance of the converter. The calculation formula of the current reference value is shown in formula (1). Finally, the SPWM pulse modulation is used to generate the pulse signal to control the switch device on/off.

$$\begin{cases} i_dref = \frac{2P_{ref}}{3U_g} \\ i_qref = -\frac{2Q_{ref}}{3U_g} \end{cases} \quad (1)$$

Where U_g is the D-axis component of the grid voltage.

When the system fails, the grid-connected converter control is put into fault pass control mode and the working mode is switched to reactive power priority mode. Reactive power is generated during voltage drop, and reactive power is absorbed during voltage rise to support voltage recovery of the grid. The fault crossing control link is used to maintain the system's on-grid operation and support the voltage recovery of the grid during the fault period, so as to ensure that the energy storage system has the fault crossing capability, as shown in Figure 3. VT is the effective value of the voltage at the junction point.

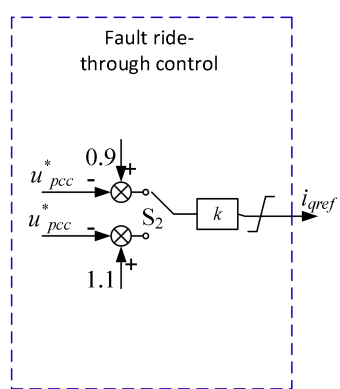


Fig. 3. Fault control link

According to the requirement of reactive power support capability during fault crossing, $iqref1$ and $iqref2$

of Q-axis current during low voltage crossing and high voltage crossing are shown in formula (2) respectively.

$$\begin{cases} iqref1 = k(0.9 - VT) & 0.2 \leq VT \leq 0.9 \\ iqref2 = k(VT - 1.1) & 1.1 \leq VT \leq 1.3 \end{cases} \quad (2)$$

In the formula, VT is the effective value of the grid voltage; k is a constant coefficient greater than 1.5.

During normal grid-connected operation, the inner ring is connected with the positive sequence power outer ring; Once the voltage drop/rise is detected, the outer ring switches to the fault crossing control link, which includes low voltage crossing and high voltage crossing, which is controlled by switch $S1$; After the voltage returns to normal, the inner ring is connected to the positive sequence power outer ring.

B. DC-DC control policy

The electrochemical energy storage system needs to achieve bidirectional energy transmission [4], so the DC-DC converter should have the ability of bidirectional conversion. A DC-DC converter is a device that converts a DC voltage or current into a different DC voltage or current [5]. It achieves smooth output by controlling the Boost and Buck working modes of the power tube on/off. It can be used to boost or reduce voltage, and can also be used to control the charge and discharge of the battery [6].

The specific working principle is shown in Figure 4. The IGBT of the upper bridge arm is $s7$, and the IGBT of the lower bridge arm is $s8$. When the battery is charged, $s7$ is turned on, $s8$ is turned off, U_{dc} side inductance $L1$ is charged and the battery is charged. When the battery is discharged, $s7$ is turned off, $s8$ is turned on, and the battery is charged to the inductor $L1$.

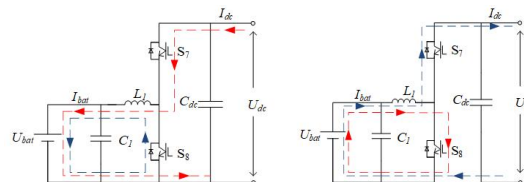


Fig. 4. DC-DC control principle

We take PSCAD to build a simulation model as an example. According to the above principles, the main circuit diagram of DC-DC is shown in Figure 5 below.

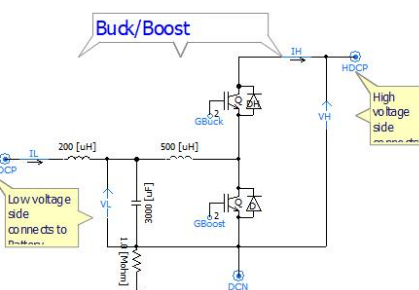


Fig. 5. DC-DC main circuit diagram

Taking battery charging as an example, the DC-DC control circuit is shown in Figure 6. When the battery is charged, the output signal of the control circuit to EnBuck is high level, and the output signal of EnBoost is low level [6]. At this time, EnBuck triggers the IGBT of the upper bridge arm in Figure 5 to work, outputs the pwm signal of GBuck, and controls the upper bridge arm to turn on and

off periodically. Lower bridge arm IGBT is not put into operation due to low EnBoost output. The signal diagram of the simulation results is shown in Figure 7.

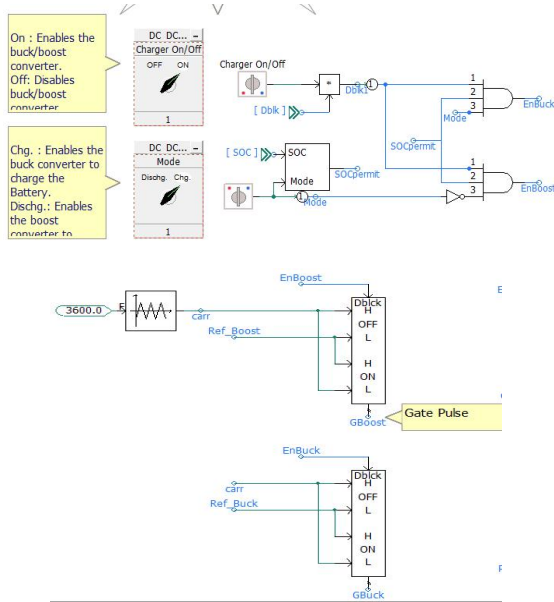


Fig. 6. DC-DC control circuit diagram

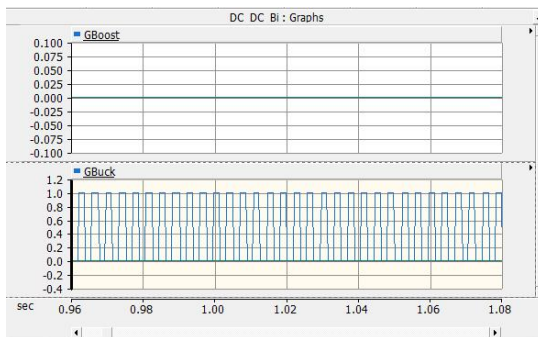


Fig. 7. Signal diagram

II. SIMULATION VERIFICATION

According to the three-phase energy storage system structure diagram shown in Figure 8 above, the three-phase energy storage system model is simulated and built in pscad. As shown in Figure 8 below, the Buck/Boost converter is connected to a battery with a rated DC voltage of 500v on the left side and a DC line with a rated DC voltage of 1kv on the right side. The grid-connected converter is connected to the AC power grid with a rated voltage of 1kv. In this system, we take the most serious failure of the system, that is, three-phase simultaneous ground fault, as an example to study whether the energy storage system has the ability of low-voltage crossing.

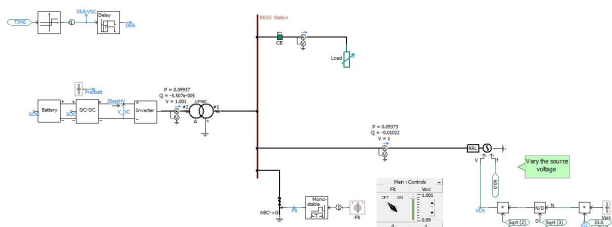


Fig. 8. Three-phase energy storage system

In order to better observe the fault crossing ability of the system, we need to observe the fault crossing ability of the energy storage system in the process of charging and discharging, and after charging when the voltage drop is caused by the three-relative fault of the system. Only when the energy storage system can achieve stable operation without off-grid in any case, the system can be put into actual use.

A. Battery charging fault crossing

According to the principles of Chapter 1, the battery is controlled to charge through the DC-DC control link. Under normal operation, it takes about 14s to charge the battery capacity from 90% to 100% in the initial state, as shown in Figure 9.

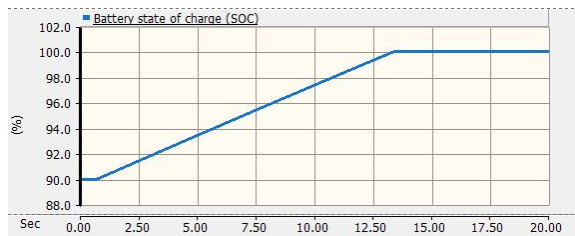


Fig. 9. Battery charging time during normal operation

In order to study the fault crossing ability of the energy storage system during and after charging, we set the fault before 14s and once after 14s respectively, and observe the power changes on the line to determine whether it has stable fault crossing ability.

In order to realize the above process, we use the fault control module as shown in Figure 10 to simulate the three-phase simultaneous ground fault. When the system runs normally, the Flt module is in the off state. When a fault needs to occur, the Flt module is turned on, in order to more intuitively observe the fault crossing ability, the fault duration is set to two seconds, after two seconds, the fault is removed, and then the power grid is normal operation. According to the above principle process, we will simulate the fault during the charging process and after the charging process to observe the change of line power.

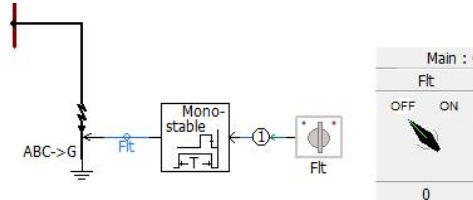


Fig. 10. Fault control module.

As shown in the signal diagram in Figure 11, when the fault occurs before or after charging, the energy storage system can run stably without going offline. In other words, the fault traversal control strategy can ensure that the energy storage system has stable fault traversal capability when the fault occurs before and after the battery charging process.

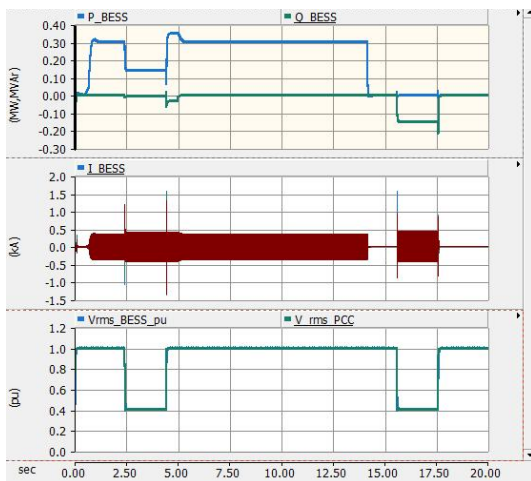


Fig. 11. Charging signal diagram

B. Battery discharge fault crossing

Under the above fault traversal control process, the energy storage system can realize the stable fault traversal ability of the battery during the charging process. According to the above analysis process, the signal diagram of power and other variables on the line is observed to analyze whether the system has stable fault crossing ability during the discharge process.

The DC-DC control ring realizes the discharge of the battery by controlling the on-off of the IGBT on the upper and lower bridge arms of buck-boost circuit. As shown in Figure 12, during the normal operation of the system, the capacity of the battery changes from 90% to 65% within 20 seconds of discharge. During this process, the fault control module in Figure 10 above is still used in this paper when a three-relative short circuit fault occurs within 20 seconds of discharge, and the power change on the line is analyzed to determine the fault traversal ability of the system during discharge. As shown in the discharge signal diagram in Figure 13, the energy storage system can also ensure stable operation without off-grid during the discharge process, and the fault control link also ensures the ability of the energy storage system to pass through the fault during the discharge process.

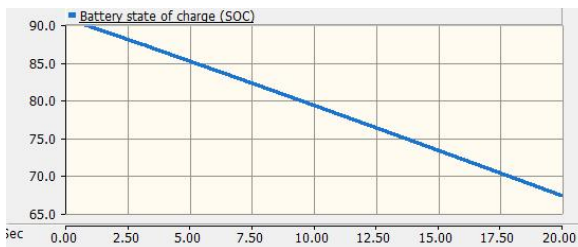


Fig. 12. Battery discharge time in normal operation

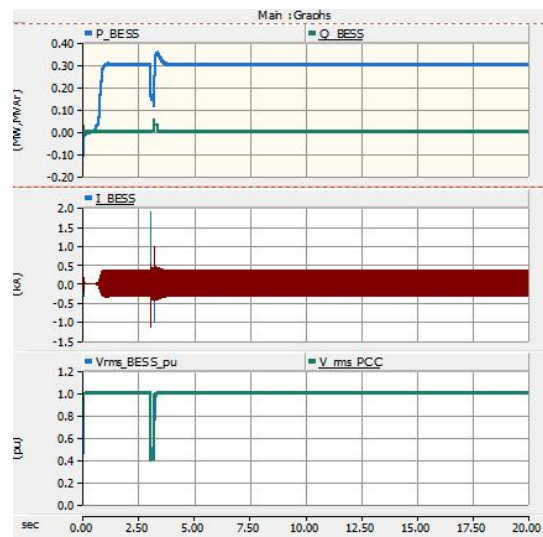


Fig. 13. Signal diagram

III. CONCLUSION

The three-phase grid-connected converters based on this paper play an important role in energy conversion and grid management, and have good flexibility to adapt to different grid environments and energy needs. It can be integrated with renewable energy sources to achieve smooth access and coordinated control, while also supporting distributed power supply access and energy scheduling.

Of course, the system has improved the fault protection function, during the system failure, the fault crossing control support system fault crossing, avoid the energy storage system off the grid, and realize the stable operation of the energy storage system.

In summary, the three-phase energy storage grid-connected converter has significant advantages and application value in energy conversion and power grid management. It can improve the efficiency of energy utilization, enhance the reliability and flexibility of the power grid, optimize the control of energy management, and reduce operating costs. With the continuous development and improvement of technology, the application prospect of three-phase energy storage grid-connected converters will be broader.

REFERENCES

- [1] Pang Xiaoyu. Research on Energy storage photovoltaic grid-connected inverter System based on MMC [D]. Jilin University, 2022.
- [2] Zhou Wu. Frequency Domain Modeling Analysis and active suppression technology of conducted electromagnetic interference for three-phase two-level inverters [D]. Huazhong University of Science and Technology, 2021.
- [3] FANG Yu. Fault Characteristics Analysis and calculation of new energy power system with inverter [D]. North China Electric Power University (Beijing), 2020.
- [4] Qi Yue. Research on Control strategy of microgrid grid-connected inverter based on Virtual synchro [D]. Harbin Institute of Technology, 2016.
- [5] Bai Zihong. Research on Some Relevant Theories and Application Technologies of current-mode multilevel converters [D]. Zhejiang University, 2008.
- [6] Tong Weiming. Research on Specific harmonic suppression technique of PWM Inverter [D]. Harbin Institute of Technology, 1999.